Characterization of Structured Optical Materials and Devices in the Visible, Near Infrared, and Terahertz Regimes

by

Thomas Edwin Lanier

(Under the direction of William M. Dennis)

Abstract

In this dissertation, a range of structured materials and devices with unique optical properties are characterized. Frequency-Resolved Optical Gating measurements of pulses reflected from layered dielectrics designed to stretch femtosecond optical pulses by a factor of ~ 10 are described and results are presented and analyzed. Finite-Difference Time-Domain (FDTD) code written in Fortran 90 is used in an investigation of two-beam coupling gain characteristics of hybrid organic-inorganic devices fashioned from a liquid crystal layer sandwiched between two photorefractive windows. Commercial FDTD software is used to investigate electromagnetic properties of various metallic nanostructures including the polarization properties imparted to light scattered by chiral Ag nanostructures, the dependence on morphology of the local field enhancement near the surface of Ag nanorods used for surface enhanced Raman spectroscopy, and the terahertz transmission behavior of Ag nanorods deposited on silicon.

Index words: Frequency Resolved Optical Gating, Computational Optics, Photorefractives, Metamaterials, Terahertz Optics, Finite Difference Time Domain, Liquid Crystals

Characterization of Structured Optical Materials and Devices in the Visible, Near Infrared, and Terahertz Regimes

by

Thomas Edwin Lanier

B.S., University of Georgia, 2003

A Dissertation Submitted to the Graduate Faculty
of The University of Georgia in Partial Fulfillment
of the
Requirements for the Degree

Doctor of Philosophy

Athens, Georgia

2012

Characterization of Structured Optical Materials and Devices in the Visible, Near Infrared, and Terahertz Regimes

by

Thomas Edwin Lanier

Approved:

Major Professor: William M. Dennis

Committee: Uwe Happek
Steven P. Lewis

Electronic Version Approved:

Maureen Grasso
Dean of the Graduate School
The University of Georgia
August 2012

Characterization of Structured Optical Materials and Devices in the Visible, Near Infrared, and Terahertz Regimes

Thomas E. Lanier

July 23, 2012

Dedication

To my parents Christine Gleaton Lanier and Robert Jesse Lanier, Jr.

Acknowledgments

I would like to thank the U.S. Air Force Research Laboratory for funding the bulk of my research, and for providing the impetus for various projects.

Many fellow and former graduate students have impacted my experience as a PhD candidate. I am grateful to Carl Liebig for introducing me to the laser laboratory, and for overseeing my early experiments. I thank Sebastian Winkler for authoring the FROG code, commenting it mostly in English, and for teaching me that science is more than a set of details integrated over all knowledge space. I thank Sarah Dunning for conducting the computational design studies that led to the fabrication of the pulse-stretching mirrors. I am grateful to Jeremy Gulley for being a great combination of friend and scientific peer, and for understanding that my criticism is always constructive and an application of the golden rule. I also thank Mohua Bhattacharya for her kindness, for being a trustworthy analyst, and for so gracefully making me feel as smart as she.

Former group member Erik Zeek is acknowledged for offering his sincere and helpful comments on my fledgling presentations in group meetings. I owe more than a sentence to systems administrators Mike Caplinger and Jeff Deroshia for always managing the logistics of my computational work with the utmost professionalism and expertise. I thank Dr. Susanne Ullrich for nudging me toward ultrafast laser conferences, and for granting me the use of her laser system. Many thanks to Dr. Yiping Zhao for the additional motivation and guidance provided during my studies of metallic nanostructures.

Lastly, I would like to acknowledge the members of my PhD advisory committee, not only for serving on it, but also for their influence on my development as a scientist. I thank Dr. Uwe Happek for offering the use of laboratory equipment as well as hands-on assistance in the intensity calibration of my spectrograph, and for years of sincere, down-to-earth guidance. I acknowledge Dr. Steven P. Lewis as being, as I have stated on a number of occasions, "my favorite physics teacher" (you're a close second, UGA Physics & Astronomy faculty!). Finally, I'd like to express profound gratitude to my advisor, mentor, and friend, Dr. William M. Dennis. It stands to reason that there must be some upper limit on one's mentoring capacity in terms of professionalism, empathy, and willingness and ability to engage in friendly scientific discourse. I can assure you that you will not find his. In retrospect, this has subconsciously been a sort of goal during my PhD candidacy, but I don't believe I've ever come close. He is a model of scientific integrity, pedagogical expertise, and personal character. I can only hope that my future holds a similar brand of success.

Contents

List of Tables

Chapter 1

Introduction

1.1 Background

Since the first appearance of the laser in 1960 [1], coherent, high-intensity light sources have played an important role in many areas of science and technology. The consequent advancement of optical device technology has necessarily occurred simultaneously. Advances in studies of thin film optics, the dynamics of organic dye molecules, semiconductors, and nonlinear crystals both owe their existence to and share credit for advances in laser technology. During the same time period, computational power has dramatically increased and the field of computational optics has developed and matured. There is currently significant interest in the optical properties of materials engineered at the nanoscale and their use in metamaterial applications. Modern electromagnetic systems constituted by structured optical materials and devices demand accurate numerical approximation schemes that have only become practical in recent years. The topic of this dissertation is the interaction with such structured materials of electromagnetic radiation (visible, near infrared, and terahertz) with a view to a variety of optical applications.

The behavior of classical electromagnetic phenomena is described by the macroscopic Maxwell equations:

$$\boldsymbol{\nabla} \times \mathbf{H} = \frac{\partial \mathbf{D}}{\partial t} + \mathbf{J} \qquad \boldsymbol{\nabla} \times \mathbf{E} = -\frac{\partial \mathbf{B}}{\partial t} \tag{1.1}$$

$$\boldsymbol{\nabla} \cdot \mathbf{B} = 0 \qquad \boldsymbol{\nabla} \cdot \mathbf{D} = \rho \tag{1.2}$$

These equations are closed by constitutive relations

$$\mathbf{D} = \mathbf{D}(\mathbf{E}, \mathbf{B}) \qquad \text{and} \qquad \mathbf{H} = \mathbf{H}(\mathbf{E}, \mathbf{B}) \tag{1.3}$$

and $\mathbf{J} = \mathbf{J}(\mathbf{E}, \mathbf{B})$. These relations, to whatever extent they offer a mathematically viable solution, or even exist in closed form, contain the effects that materials have on the time evolution of the fields occurring in Eqs. 1.1 while maintaining Eqs. 1.2. Optics typically avoids explicit reference to the free charge and current densities ρ and $\mathbf{J}$, either because they are zero or because they are otherwise modeled using Eqs. 1.3.

If a material may be described by

$$D = \varepsilon_0 E + P \qquad \text{and} \qquad H = \frac{1}{\mu_0} B \tag{1.4}$$

where $P = \varepsilon_0 \chi^{(1)} E$, with $\chi^{(1)}$ a constant, then the optical properties of the non-magnetic material are captured by a refractive index $n \equiv \sqrt{\varepsilon_\mathrm{r}\, \mu_\mathrm{r}} = \sqrt{\varepsilon_\mathrm{r}} = \sqrt{1 + \chi^{(1)}}$. This treats the material as responding instantaneously through a polarization that has a linear, isotropic dependence on $\mathbf{E}$. High-intensity lasers have brought about the need for inclusion of higher

order terms in the polarization

$$P = \epsilon_0 \left[\chi^{(1)} E + \chi^{(2)} E^2 + \chi^{(3)} E^3 + \cdots \right] \tag{1.5}$$

so that, for example, the material response may depend on the intensity $I \propto E^2$. Another possibility is that the material has a frequency-dependent response to $\mathbf{E}$. Actually, the requirement that a material response be causal implies, through the Kramers-Kronig relations that all materials are dispersive. In other words, $\mathbf{D}(\omega) = \varepsilon(\omega)\,\mathbf{E}(\omega)$, where the electric permittivity $\varepsilon(\omega)$ may, for example, be derived from considering a collection of damped, driven oscillators that constitute radiating dipoles. The dependence on the vectorial nature of the fields is captured by retaining the tensor nature of the permittivity so that $D_i = \sum_j \varepsilon_{ij} E_j$, and the coupling between orthogonal components of $\mathbf{D}$ and $\mathbf{E}$ occurs through non-zero off-diagonal elements of $\hat{\varepsilon}$. Additionally, effects non-local in space may be exhibited, rendering the spatial Fourier transform of the permittivity a function of wave vector [2]. Consideration of such spatial dispersion is particularly relevant in the context of materials containing nanoscale units whose influence on the optical properties of a structure arise as a result of its morphology [3]. Its combination with frequency dispersion and anisotropy is expressed explicitly by the notation $\hat{\varepsilon}(\omega, \mathbf{k})$. Much of this dissertation consists of investigations of optical devices and materials whose response may be conceptualized in this manner. In particular, the following three types of optical system are investigated:

i) Deposited dielectric layer structures for femtosecond pulse shaping applications

ii) A liquid crystal layer positioned between two photorefractive windows for two-beam coupling applications

iii) Metallic nanostructures for surface enhanced Raman spectroscopy and visible and terahertz metamaterial applications

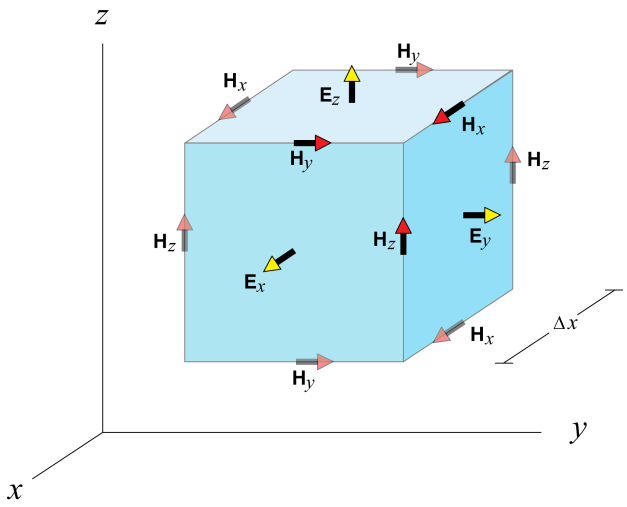

Figure 1.1: The Yee space lattice.

1.2 The Finite-Difference Time-Domain Method

Much of the work in this dissertation uses the Finite-Difference Time-Domain (FDTD) method, which numerically time-integrates the Maxwell curl equations. Three-dimensional space is discretized in units of Δx, Δy, and Δz, and the components of the electric and magnetic fields are interleaved on this grid resulting in discretized expressions for the spatial derivatives in the Maxwell curl equations that are second-order accurate despite being first order in Δx. This arrangement, shown in Fig. 1.1, may also be shown to satisfy Eqs. 1.2 for the case $\rho = 0$. Similarly, a leap-frog field updating scheme is employed to achieve the same second order accuracy in discretized expressions for the time derivatives that are first order in Δt. The field components as a function of space are stored in memory during the simulation, with $\mathbf{H}$ being time-shifted relative to $\mathbf{E}$ by $\Delta t/2$. The result is a simple algorithm for time-marching the components of $\mathbf{E}$ and $\mathbf{H}$ with accuracy that improves as $\Delta x \to 0$. For the case of a uniform Cartesian grid, numerical stability requires that the *Courant number*

be $S = c\Delta t/\Delta x \leq 1/\sqrt{d}$, where d is the dimensionality of the Yee space lattice. This is how the size of the time step is chosen for a given grid cell size Δx.

The purpose of an FDTD calculation is to determine the electromagnetic response of some material structure. The method has developed as a useful tool in, for example, designing microelectromechanical systems, determining radar scatter from low-visibility aircraft, and modeling very low-frequency pulse propagation around the Earth's atmosphere. These examples speak to the fact that the feasibility of this technique is determined by the relationship between the spatial scale of the problem and the wavelengths of interest. The spatial resolution of the grid must be chosen to be fine enough to resolve all wavelengths of interest, and to adequately represent the particular material morphology. Materials are imposed at particular points in space by implementing the corresponding constitutive relations for those grid locations. In this way, the FDTD method accounts for spatial dispersion automatically as long as the morphology of the material structure is adequately represented on the discrete spatial grid.

Linear dispersion may be treated by multiple approaches [4]. The frequency-domain relationship $\mathbf{D}(\omega) = \varepsilon(\omega)\,\mathbf{E}(\omega)$ becomes a convolution in the time domain. The piecewise-linear recursive-convolution method entails expressing this convolution in discrete form, inserting it into the usual FDTD field-updating expression, and using a recursion relation to avoid storing and evaluating the entire history of $\mathbf{E}(t)$ at each time step for the cases of Debye and Lorentz media. The auxiliary differential equation method solves the time-domain relationship between $\mathbf{D}$, $\mathbf{E}$, and $\mathbf{P}$ synchronously with the usual time-marching of $\mathbf{E}(t)$ and $\mathbf{H}(t)$, yielding a self-consistent composite system. In Chapter 4 of this dissertation, material dispersion is handled by the commercial software package XFdtd (Remcom). The numerical formalism for implementation of a Debye material with relative permittivity at infinite frequency ε_∞, static relative permittivity ε_s, and relaxation time τ may be augmented to realize a Drude material with plasma frequency ω_p and scattering frequency γ by reassignment of

the model parameters as follows:

$$\begin{aligned} \varepsilon_{\text{Debye}}(\omega) &\rightarrow \varepsilon_{\text{Drude}}(\omega) \\ \varepsilon_{\infty} &\rightarrow 1 \\ \varepsilon_s &\rightarrow 1 - \left(\frac{\omega_{\text{p}}}{\gamma}\right)^2 \\ \tau &\rightarrow \frac{1}{\gamma} \\ \sigma &\rightarrow \varepsilon_0 \frac{\omega_{\text{p}}^2}{\gamma} \end{aligned} \tag{1.6}$$

where σ is the conductivity that appears in FDTD updating equations that retain an Ohm's Law current density.

Anisotropy may be handled in the case of non-dispersive materials by assigning all nine elements of a permittivity tensor $\hat{\varepsilon}$ and inserting into the normal FDTD updating scheme a step in which $\mathbf{E}$ is calculated as $\mathbf{E} = \hat{\varepsilon}^{-1}\mathbf{D}$. The permittivity tensor may be assigned an arbitrary spatial dependence. Such an approach is useful when considering monochromatic optical effects in liquid crystals, which may be treated as birefringent crystals with a spatially-dependent symmetry axis.

A three-dimensional FDTD code was constructed in the Fortran 90 programming language. The computational domain must be limited in order to contain the spatially finite simulation. Waves perfectly reflect from the outer boundary because field variables are implicitly zero outside it. This is called a "perfect electrical conductor" condition because $\mathbf{E} = 0$ in the interior of a conductor in the context of electrostatics. The outgoing waves must not be allowed to reflect and interfere with the fields of interest. The outgoing waves are removed from the simulation by implementing non-physical constitutive relations in a thin layer surrounding the computational domain. This is called the "perfectly matched" absorbing boundary because, within the absorber, the Maxwell curl equations + an Ohm's

Law conductivity are symmetrized by introducing a magnetic conductivity σ^* at the interface between the computational domain (CD) and the perfectly matched layer (PML):

$$\varepsilon_0\,\varepsilon_{\mathrm{r}}\frac{\partial \mathbf{E}}{\partial t}+\sigma\mathbf{E}=\boldsymbol{\nabla}\times\mathbf{H} \qquad\qquad \mu_0\frac{\partial \mathbf{H}}{\partial t}+\sigma^*\mathbf{H}=-\boldsymbol{\nabla}\times\mathbf{E} \tag{1.7}$$

Electrical and magnetic wave impedances are matched by imposing the matching condition

$$\frac{\sigma}{\varepsilon_0}=\frac{\sigma^*}{\mu_0} \tag{1.8}$$

These conductivities increase as a function of depth in the PML, so that fields propagating into them rapidly decay irrespective of wavelength, polarization, and propagation direction. This reduces reflections from the CD-PML interface to a negligible level while allowing electromagnetic waves to be attenuated as they propagate into the PML. The result is that the fields stored in the CD correspond to those of the unbounded optical system.

Various types of PML exist [5]. A form must be chosen that suits the particular situation. For example, the constitutive relations and numerical formalism must be modified for the case of a PML that is in spatial contact with a dispersive medium. The uniaxial PML (UPML) was chosen for simplicity, and to match the PML to a non-magnetic medium with refractive index $n \geq 1$.

The construction of the UPML may be summarized by writing the impedance-matching condition in Eq. 1.8 as

$$\frac{\hat{\sigma}(\xi)}{\varepsilon_0\,\varepsilon_{\mathrm{r}}}=\frac{\hat{\sigma}^*(\xi)}{\mu_0} \tag{1.9}$$

where $n \equiv \sqrt{\varepsilon_{\mathrm{r}}\,\mu_{\mathrm{r}}}=\sqrt{\varepsilon_{\mathrm{r}}}$ is the refractive index of the non-magnetic medium adjacent to the PML, ξ is a generalized coordinate representing depth into the PML, and the elements of the diagonal tensors $\hat{\sigma}(\xi)$ and $\hat{\sigma}^*(\xi)$ are constructed as follows: If ξ represents variation of the i^{th} Cartesian coordinate x_i, then σ_{ii} and σ^*_{ii} increase from zero as a function of ξ according

to an m^{th}-order monomial in x_i, where the details of the monomial depend on the desired reflectance $R \ll 1$ and the total PML thickness. Otherwise, $\sigma_{ii} = 0$. The parameter m is typically chosen to be 3 or 5. Implementing this absorbing boundary condition involves using field-updating expressions distinct from those applied within the CD, so that the `do` loops corresponding to 3D space are somewhat increased in complexity, and distinct subroutines are called to update fields in the PML.

1.3 Layout of this dissertation

This dissertation is organized as follows: Chapter 2 describes measurements of ultrashort pulses reflected from layered dielectrics that were designed with the help of FDTD calculations. In addition to traditional optical measurements, the full complex pulse fields $E(t)$ corresponding to incident and reflected pulses were measured using the Frequency-Resolved Optical Gating technique. Chapter 3 presents the use of a two-dimensional version of the Fortran FDTD code in an investigation of two-beam coupling in an organic liquid crystal layer sandwiched between two inorganic photorefractive windows. The origin of gain coefficients measured for these devices is not well understood. The effects that the anisotropy and spatial dependence of the liquid crystal permittivity have on beam coupling were simulated by the FDTD method. Finally, Chapter 4 will present the use of XFdtd to investigate electromagnetic properties of various metallic nanostructures including the polarization properties imparted to light scattered by helical Ag nanorods. In Section 4.2, the dependence on morphology of the local field enhancement near the surface of Ag nanorods for surface enhanced Raman spectroscopy is investigated. Experimental transmission spectra at THz frequencies for similar nanostructures were calculated (described in Section 4.3), taking advantage of the ability of FDTD calculations to produce broadband spectra from a single simulation. Finally, Chapter 5 will provide a summary, state conclusions, and describe future work.

Chapter 2

Experimental Characterization of Femtosecond Pulse-stretching Devices

2.1 Introduction

Fabrication of optical devices consisting of deposited layers of dielectric materials is commonplace among optics manufacturers. Devices for many applications are realizable using deposited materials that are effectively nondispersive, isotropic, and linear, in which case the reflectivity and transmissivity of each layer interface is characterized by two refractive indices alone. The optical properties of a device composed of a sequence of non-absorbing material layers with refractive indices alternating between n_1 and n_2 are determined by the set of interference conditions at the 1-2 and 2-1 interfaces. For a given incident wavelength, these conditions are determined by the sequence of optical path lengths constituted by the sequence of layer thicknesses. The reflectance spectrum $R(\omega) = \left|\frac{E_{\mathrm{r}}(\omega)}{E_0(\omega)}\right|^2$ of such a layered structure is determined by the set of boundary conditions imposed on Maxwell's curl equations at each interface. The reflectance spectrum $R(\omega)$ may be calculated by, for example, the Characteristic Matrix method [6]. This quantity describes the kinematics of a multilay-

ered device in that no reference is made to any temporal structure exhibited by an incident wave (apart from oscillation at frequency ω). The question of how a multilayered device *shapes* an optical pulse is a dynamical one to which an answer may be given in terms of the reflected intensity envelope $I(t) \propto |E(t)|^2$, where the complex electric field amplitude is

$$E(t) = \sqrt{I(t)}\ \exp(-i\ \phi(t)). \tag{2.1}$$

These quantities are defined relative to the convention that states the time dependence of the real-valued electric field as

$$\mathcal{E}(t) = \frac{1}{2}\sqrt{I(t)}\ \exp(i\,[\,\omega_0 t - \phi(t)\,])\ +\ \text{c.c.} \tag{2.2}$$

where ω_0 is the carrier frequency and *c.c.* denotes the preceding term's complex conjugate. The phase $\phi(t)$ of an optical pulse contains information about which frequencies occur at what time. The phase of a pulse incident upon a particular multilayered structure has significant impact on the reflected pulse shape. This is demonstrated most clearly by considering the action of a pulse-chirping mirror on two oppositely chirped incident pulses with the same spectrum. Roughly speaking, one pulse will be stretched in time and the other compressed by virtue of the fact that reflections from the layers closer to the front face of the structure will occur at the front of the reflected pulse. The more precise details of each of the reflected intensity envelopes $I_{\mathrm{r}}^{(1)}(t)$ and $I_{\mathrm{r}}^{(2)}(t)$ will have a strong dependence upon the particular sequence of layer thicknesses. It is natural to compute these reflected pulses directly in the time domain by the FDTD method, with all phase information implicitly contained by real-valued data. Performing these calculations in a single spatial dimension has the benefit of vastly reducing the computational resources necessary for simulation of a given optical experiment, at the cost of being able to model only high-symmetry systems at normal incidence. Such calculations have been used [7] as feedback to a genetic algorithm that

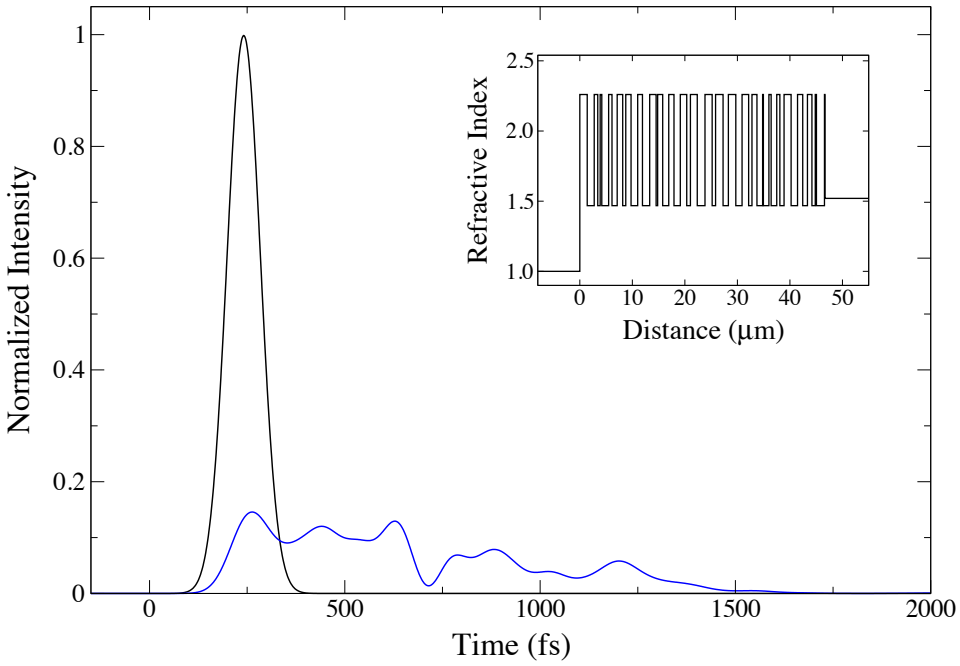

Figure 2.1: The temporal intensity envelopes of the incident pulse (black) and reflected pulse calculated by the FDTD method (blue) for the device whose performance is experimentally evaluated in this chapter. The refractive index profile of the device is shown in the inset

searches for a sequence of layer thicknesses that best produces some desired intensity envelope upon reflection. This chapter describes the experimental characterization of the performance of a prototype device designed in this way to stretch Gaussian pulses with FWHM[1] of 100 fs and 800 nm center wavelength at normal incidence. The refractive index profile of the as-designed device and its performance as predicted by FDTD calculations are shown in Fig. 2.1. These refractive indices correspond to deposited niobium pentoxide (Nb_2O_5) and silicon dioxide (SiO_2). A possible application of such a reduction of peak intensity is the amplification of laser pulses. Laser systems that use grating-based modules to stretch, amplify, and subsequently recompress ultrashort pulses while avoiding damage to the gain

[1]Full width at half maximum of the intensity

medium are commonplace. As these modules contain many expensive optical elements that require nontrivial alignment, their replacement by a single mirror would simultaneously provide the benefits of cost-effectiveness and increased compactness. Traditional optical measurements will be described in addition to measurements of the complex pulse field corresponding to Eq. 2.1 using the Frequency-Resolved Optical Gating (FROG) technique, which is described in Section 2.4.

2.2 Laser System

The ultrashort pulses used in this work were nominally 100 fs *s*-polarized pulses centered at 800 nm produced by a *Tsunami* (Spectra-Physics) titanium sapphire (Ti:Al_2O_3) oscillator operating at 82 MHz with a nominal average power of 350 mW. These specifications correspond to a peak power of 40 kW, which corresponds to a peak intensity of ~ 1 MW/cm^2 if a $1/e^2$ beam radius $w = 1$ mm is assumed.

The energy source for this laser is a *Millennia* (Spectra-Physics) diode-pumped laser providing a 5 W continuous-wave output at 532 nm. The gain medium of this laser is neodymium yttrium vanadate (Nd:YVO_4). The 1064 nm emission from this crystal is intracavity-frequency-doubled by a lithium triborate (LBO) crystal, providing a 5 W pump to the Ti:Al_2O_3 at 532 nm. In the sapphire host, electronic states associated with ground state absorption of pump photons by Ti^{3+} ions couple to vibrational states associated with the ion-host system, resulting in the appreciable radiative transition linewidth that provides the frequency content necessary for the construction of ultrashort optical pulses [8].

Pulsed operation in this laser cavity is induced by an acousto-optic modulator, which uses the acoustic standing wave in an intracavity crystal driven transversely by a piezoelectric transducer at frequency ν_a to produce a refractive index modulation that switches on and off with frequency $2\nu_a$. This dynamic transmission grating diffracts light out of the cavity,

providing a time-dependent loss that may be used to constrain the oscillator to longitudinal modes with frequency spacing equal to the round trip transit time of the cavity. This is achieved when the condition $2\nu_{\mathrm{a}} = \frac{c}{2L}$ is satisfied, where L is the cavity length and c is the speed of light in vacuum. Stable operation requires that this condition be precisely maintained despite inherent variations in L. The driving frequency ν_{a} is therefore dynamically corrected by a feedback circuit that monitors modulation of the laser output arising from mode beating associated with the phase mismatch caused by waver of L. Thus, regenerative mode-locking derives the appropriate ν_{a} from the laser cavity itself.

The preceding discussion considers all mode-locked frequency components in the cavity to have the same round trip transit time. Dispersion in the intracavity materials (including air) was neglected. The inherent wavelength dependence of the refractive indices of these materials produces positive group velocity dispersion (GVD), delaying higher frequency components relative to lower ones. In addition, an intensity-dependent refractive index experienced in the Ti:Al_2O_3 rod perturbs the phase velocity near the peak of the instantaneous intensity envelope. This causes self-phase modulation, which adds to the positive GVD. The nominally 100 fs bandwidth-limited output of the oscillator is accomplished by compensating for these effects through the introduction of negative GVD to the cavity. Inserting a set of prisms into the cavity results in a wavelength-dependent cavity length $L(\lambda)$, facilitating round trip transit times that are approximately uniform across the cavity pass band.

2.3 Preliminary Measurements

Before discussing measurements of the complex field amplitude of pulses incident upon and reflected from the pulse-stretching mirrors, several supplementary optical measurements made using more traditional methods will be presented. In what follows, the prototypes will be referred to by the serial numbers F120309-2 and F120309-3 assigned by those responsible for the fabrication at Teledyne Scientific & Imaging, LLC.

Firstly, the nominal reflectivity was measured using a Spectra-Physics 407A power meter at a 0.36° angle of incidence, which is the incidence angle that was used for subsequent ultrashort pulse measurements[2]. Since the incident and reflected beams were nearly collinear, the power meter head could not be directly used to measure the power of the reflected beam without blocking the incident beam. The reflectivity was therefore measured by monitoring the ratio of the power reflected from the next mirror in the beam path ($> 99\%$ reflectivity) to the incident power. The resulting reflectivities were found to be $R = 0.77$ for F120309-2 and $R = 0.71$ for F120309-3; somewhat lower than the reflectivity of $R = 0.82$ predicted for the as-designed mirror.

During preliminary measurements, it was noted that both F120309-2 and F120309-3 were convex rather than planar. The radius of curvature of each mirror was measured by reflecting a HeNe laser from the mirror and measuring the reflected beam spot sizes at fixed distances from the mirror. The divergence of the HeNe laser beam was accounted for by first characterizing it by using a New Focus 5103 planar metal mirror in place of the pulse-stretching mirrors. The results for the radii of curvature are $R_{\mathrm{C}} = +1.62$ m for F120309-2 and $R_{\mathrm{C}} = +2.68$ m for F120309-3. These properties are summarized in Table 2.1.

The reflectance spectra for the pulse-stretching mirrors were calculated from pulse spectra measured using an IST-Rees spectrometer model E201LSA03A. The measured reflectance

[2]This choice of incidence angle is explained in Section 2.4

Table 2.1: Reflectivity and radius of curvature of pulse-stretching mirrors

Mirror	Nominal reflectivity – R	Radius of curvature – R_C (m)
As designed	0.82	∞
F120309-2	0.77	+1.62
F120309-3	0.71	+2.68

spectrum of each prototype is shown in Fig. 2.2 along with the reflectance spectra calculated from Fourier-transformed FDTD results for the as-designed mirror as well as a design with 0.5% random error introduced to the layer thicknesses. The pulse spectra shown in the inset of Fig. 2.2 have been intensity calibrated using the reflectivity data in Table 2.1. Specifically, the measured incident pulse spectrum was first normalized so that its peak is unity, and each reflected pulse spectrum is subsequently scaled by the product formed by the corresponding nominal reflectivity listed in Table 2.1 and the ratio of the integrated incident spectrum to the integrated reflected spectrum.

The experimental reflectances were calculated by taking the point-by-point ratio of the reflected laser pulse spectra to incident laser pulse spectrum. Reflectance values > 1 arise from the combined effects of error in the wavelength calibration $\ll 1$ nm and the low precision of the measurement of the reflectivity used to calibrate the vertical scale of each pulse spectrum.

It is evident that there are features in the measured and calculated reflectance spectra that do not overlap, and that the mismatch is quite similar to that between the spectra of the as-designed mirror and the mirror with error introduced. In order to ensure that the non-normal incidence measurement of the reflectance was not responsible for the deviation of the measured spectra from that of the original design, the spectrum of one of the devices

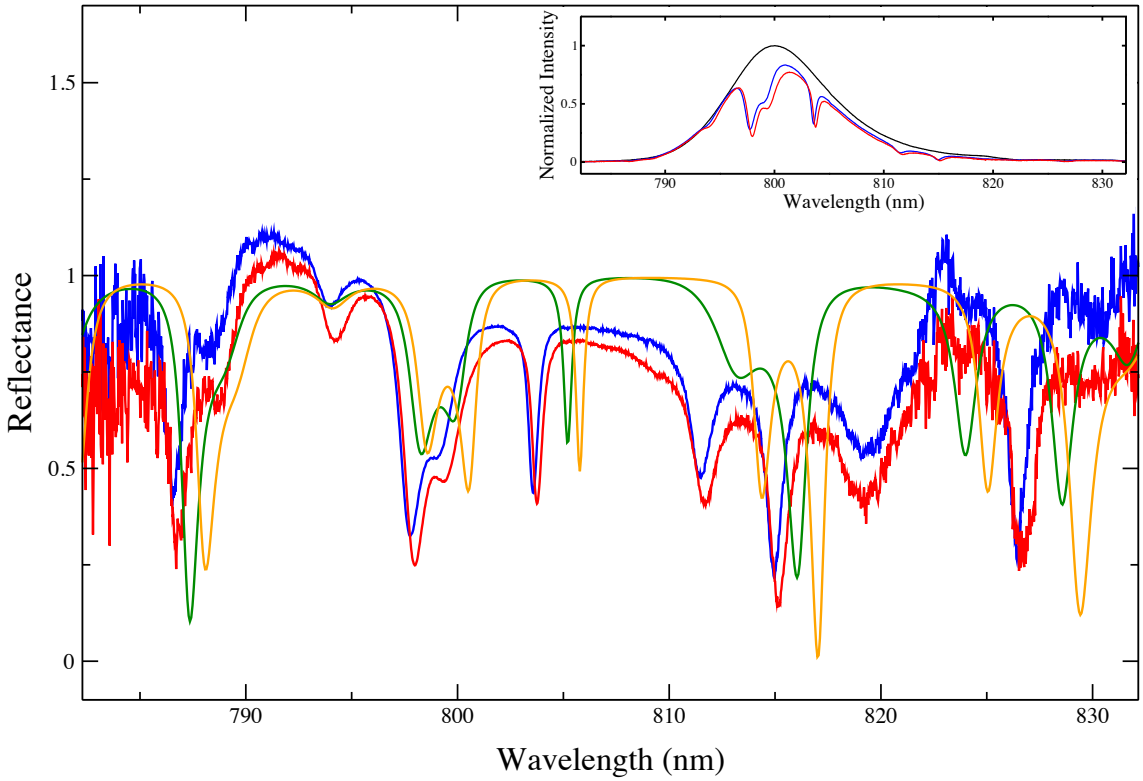

Figure 2.2: Reflectance spectra of F120309-2 (blue) and F120309-3 (red), the mirror design calculated by the FDTD method (green), and the mirror design incorporating a 0.5% error calculated by the FDTD method (orange). Inset: The measured pulse spectra used to compute reflectances. See text for details.

was measured as a function of the angle of incidence between 0.21° and 0.52°. The spectrum was found to be independent of incidence angle over this range.

The time-dependence of an ultrashort optical pulse has been traditionally expressed in terms of its second-order intensity autocorrelation, which uses a copy of the pulse to gate itself in time. By crossing two copies of the pulse in an appropriate[3] nonlinear medium, a third pulse with spectrum containing the summed frequencies is produced and propagates in a direction determined by conservation of momentum. This is depicted schematically in

[3]This will be elaborated in Section 2.4

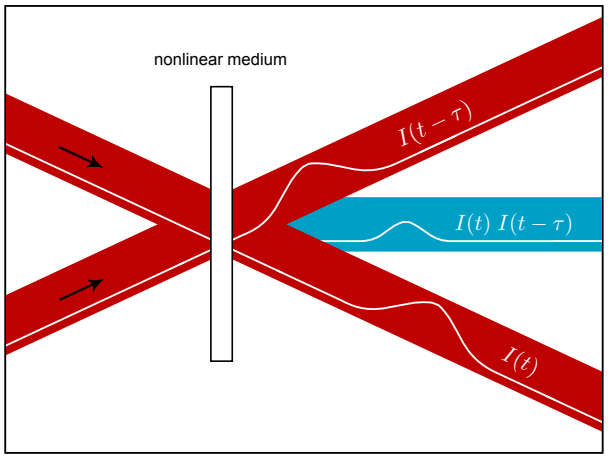

Figure 2.3: Schematic of an autocorrelation measurement with noncollinear beam geometry.

Fig. 2.3. The time-integrated intensity of the nonlinear signal pulse is measured as a function of delay τ, thus providing a crude measurement of ultrashort laser pulse duration. While the functional form of the pulse shape must be presumed to extract a pulse duration $\Delta\tau_{\text{pulse}}$ from such a measurement, an autocorrelation trace provides some qualitative indication of the duration of a pulse with unknown shape. Furthermore, the autocorrelation data can be compared to the delay marginal of a Frequency-Resolved Optical Gating (FROG) measurement (see Section 2.4) as an aid to ascertaining the reliability of that measurement. Autocorrelations of the incident pulse and pulses reflected from both F120309-2 and F120309-3 were measured using a Spectra-Physics Model 409 rotating-block autocorrelator. This device measures the quantity

$$A(\tau) = \int_{-\infty}^{\infty} I(t)\ I(t-\tau)\ dt \tag{2.3}$$

Table 2.2: Standard deviations of autocorrelation measurements of both incident and reflected pulses.

Laser pulse	σ_A (fs)
Incident pulse	53.8
Reflected pulse: F120309-2	409.0
Reflected pulse: F120309-3	402.9

whose FWHM $\Delta\tau_A$ is related to the FWHM of a Gaussian pulse intensity by

$$\Delta\tau_{\text{pulse}} = \frac{1}{\sqrt{2}}\,\Delta\tau_A = 2\sqrt{\ln 2}\,\sigma_A \tag{2.4}$$

where σ_A is the standard deviation of the autocorrelation. This instrument is calibrated by inserting a fused silica etalon into one of the beam paths, which shifts the autocorrelation trace by a known optical time delay. Fig. 2.4 shows the normalized autocorrelations of pulses reflected from each of the mirrors as well as that of the incident pulse. The standard deviations of these distributions are given in Table 2.2. The assumption of Gaussian intensity is reasonable for the incident pulse, which yields a FWHM of 89.6 fs.

2.4 FROG Measurements

2.4.1 The FROG technique

The autocorrelation measurements presented in Section 2.3 clearly indicate that the incident Gaussian pulse has been stretched significantly in time upon reflection from the prototype devices. In addition, the ripples in the reflected pulse autocorrelation data indicate significant structure in the reflected intensity envelope. In order to fully characterize the electric field of

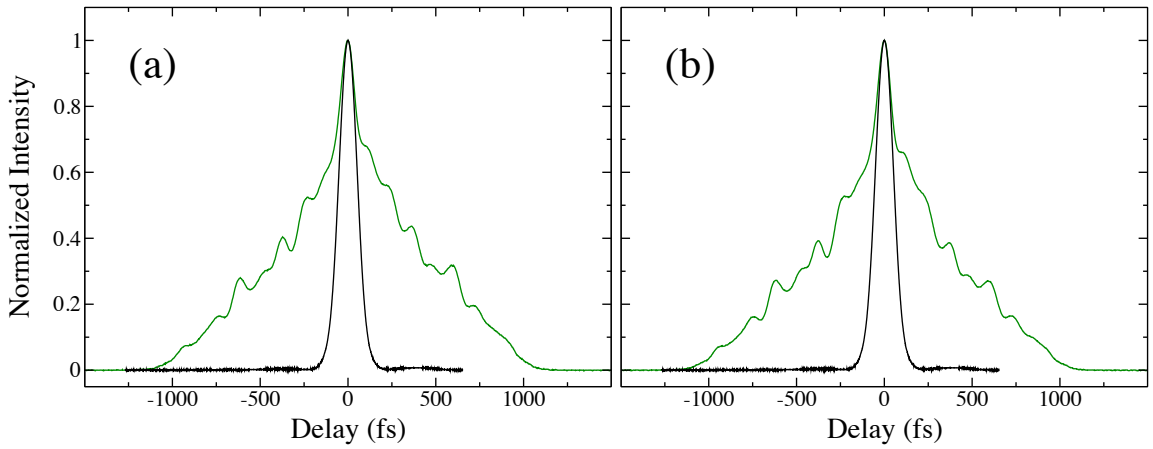

Figure 2.4: Measured intensity autocorrelations of incident and reflected pulses. (a) Pulse reflected from F120309-2 (green) and the incident pulse (black). (b) Pulse reflected from F120309-3 (green) and the incident pulse (black).

the pulse, it is necessary to obtain information about the amplitude and phase of the pulse electric field. This information is contained in the functions $I(t)$ and $\phi(t)$ in Eq. 2.1. One way of obtaining this information is by spectrally analyzing the pulses whose intensity vs. delay produced the autocorrelation. Spectra of the delay-dependent nonlinear signal pulses may be measured, resulting in a two-dimensional data set referred to as the FROG trace:

$$I_{\mathrm{FROG}}(\omega,\tau) = |E_{\mathrm{sig}}(\omega,\tau)|^2 = \left| \int_{-\infty}^{\infty} E_{\mathrm{sig}}(t,\tau)\ \exp(-i\omega t)\ dt \right|^2 \tag{2.5}$$

where in this work,

$$E_{\mathrm{sig}}(t,\tau) = E(t)\,E(t-\tau) \tag{2.6}$$

is the nonlinear signal pulse produced for a particular delay τ in the autocorrelation geometry. The combination of spectral and time information contained in this data set overdetermines the $I(t)$ and $\phi(t)$ sought for the complex amplitude $E(t)$ which can be extracted by means of a phase retrieval process. Although Eq. 2.5 cannot be solved directly for the pulse field

$E(t)$, this relationship provides the retrieval algorithm with the constraint that the squared magnitude of the Fourier transform of $E_{\text{sig}}(t,\tau)$ must be in agreement with the FROG trace data. That $E_{\text{sig}}(t,\tau)$ must be generated by the functional form $E(t)\,E(t-\tau)$ provides an additional constraint on the $E(t)$ being sought[4]. This technique was first applied to the measurement of ultrafast pulses by Trebino, *et al.* [9] and is called Frequency-Resolved Optical Gating (FROG). The FROG technique was used to time-resolve the complex amplitude of the pulse both before and after the reflection from pulse-stretching mirrors F120309-2 and F120309-3.

The form of $E_{\text{sig}}(t,\tau)$ in Eq. 2.6 corresponds to SHG-FROG, or FROG "in an SHG geometry", where SHG refers to the nonlinear optical process of second harmonic generation. This is because the signal pulse field is generated by the polarization term that is second order in the instantaneous electric field: $P^{(2)} = \varepsilon_0 \chi^{(2)} \mathcal{E}^2$. For the case of two non-collinear beams ("1" and "2") overlapping in the nonlinear medium, $\mathcal{E}^2$ has many terms, one being the sum-frequency generation term

$$\frac{1}{2}\,E_1\,E_2\,\exp(\,i\,[\,(\omega_1+\omega_2)\,t-(\mathbf{k}_1+\mathbf{k}_2)\cdot\mathbf{r}\,]\,)\;+\;\text{c.c.} \tag{2.7}$$

This term is responsible for the signal pulse measured in the autocorrelation geometry with propagation vector $\mathbf{k}_1+\mathbf{k}_2$ (see [10], pgs. 40, 279 and [11], pg. 249).

The SHG-FROG data trace is symmetric about $\tau = 0$, which is the delay setting at which the pulse copies are perfectly overlapped in time. As a consequence, the pulse resulting from the retrieval algorithm is ambiguous with respect to the direction of time. In other words, any given pulse and a time-reversed version of it would produce the same FROG trace, so an SHG-FROG trace cannot not determine which pulse was actually measured. Additional measurements or assumptions may be made to argue for a particular choice of the direction of

[4]See Appendix A for description of the retrieval algorithm.

time. Here, this ambiguity is considered to be removed in the stretched pulse measurements by knowledge of the pulse reflected by the mirror design in FDTD simulations.

The integral of the FROG trace over either of its dimensions results in a marginal that can be measured independently. Specifically, the delay marginal is the one-dimensional curve resulting from integration of the FROG trace data over all frequencies and equals the autocorrelation $A(\tau)$. The frequency marginal is the one-dimensional curve resulting from integration over the delay coordinate, and equals the autoconvolution of the spectrum of the pulse being measured. These marginals provide consistency checks of the pulse measurement, and comparisons between them and independent measurements accompany all of the pulse measurement results presented in Section 2.4.3. It should be noted that the autoconvolutions depicted in Section 2.4.3 have not been manually shifted onto frequency marginals. Instead, the pulse spectra used to calculate them are first zero-padded down to zero frequency, lending meaning to the relative shift between these two curves. This can be accounted for by the day-to-day center wavelength of operation of the laser, which in a few instances was allowed to drift by < 0.5 nm. The absolute offset of the autoconvolution is sensitive to such shifts.

2.4.2 Experimental details and considerations

The pulses reflected from the mirrors were measured using the FROG technique in an SHG geometry. The experimental setup for these measurements is shown in Fig. 2.5. In order to compensate for the convex surfaces of F120309-2 and F120309-3, the incident pulse was first passed through a beam-expanding telescope (BET), which was used to collimate the reflection from the stretcher mirrors and ensure that the beam diameter was kept within the clear aperture of subsequent optics. Light reflected at normal incidence from a sample is traditionally measured using a beam splitter placed in collinear incident and reflected beam paths. Associated with that approach is a loss of 75% of the pulse intensity. The small-angle geometry was chosen for this experiment with a mind to the intensity dependence

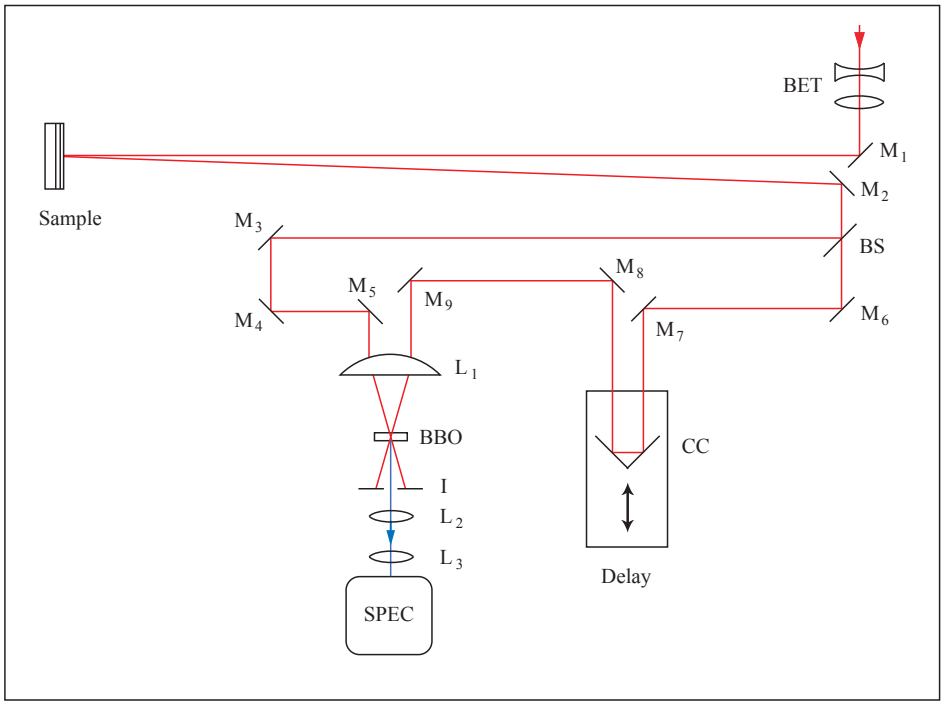

Figure 2.5: Schematic of the SHG-FROG experiment. BET=Beam Expanding Telescope; BS=Beam Splitter; SPEC=Spectrometer; L_1=80 mm focal length lens; CC=Corner Cube reflector

of the nonlinear process required to measure the unamplified, stretched pulses with low peak intensity. Since the pulse-stretching mirrors were designed for normal incidence, it was necessary to estimate the effect of using a 0.36° angle of incidence. The use of a non-zero incidence angle in the experimental design is validated by considering the fractional change in the optical path length Λ_m in a layer caused by a non-zero angle of incidence,

$$\frac{\Delta\Lambda_m}{\Lambda_m} = \sec\theta_m - 1 \tag{2.8}$$

where θ_m is the angle of refraction in the medium. The fractional changes in the optical path length for Nb_2O_5 and SiO_2 are 4×10^{-6} and 9×10^{-6} respectively, which amounts to

an absolute change in optical path length of less than $\lambda/4200$ for the thickest layers. The robustness of this mirror design with respect to detuning of the center wavelength from 790 nm to 815 nm was investigated elsewhere [7]. Since this wavelength detuning introduces a much larger fractional error than that introduced by the non-normal incidence geometry used in the experiment, any effects associated with the nonzero 0.36° incidence angle may be regarded as negligible. After reflection from a pulse-stretching mirror, the pulse was amplitude-split using a beam splitter (BS). One of these pulses was propagated through a fixed optical delay, while the second pulse was propagated through a variable delay line. This resulted in a gate pulse $E(t-\tau)$, which is delayed relative to the probe pulse $E(t)$. An $f = 80$ mm lens (L_1) was used to focus the beams into a thin Beta-Barium Borate (BBO) crystal. The resulting nonlinear signal pulse was collimated and imaged onto the slit of the spectrometer (SPEC), which recorded its wavelength spectrum for each value of the time delay between pulses.

The thickness L of the nonlinear medium is the most important parameter of a FROG experiment. A FROG measurement is only valid insofar as the nonlinear process is uniformly phase-matched over the entire bandwidth of the pulse. The crystal phase-matching bandwidth scales as $1/L$, whereas the intensity of the phase-matched signal pulse, and therefore the signal-to-noise ratio of the FROG trace, is proportional to L^2. There is therefore a narrow range of crystal thicknesses appropriate for this measurement [10]. In order to select an appropriate crystal, the phase-matching bandwidth

$$\delta\lambda_{\mathrm{FWHM}} \approx \frac{0.44\ \lambda_0/L}{\left|\left[\frac{dn}{d\lambda}\right]_{\lambda=\lambda_0} - \frac{1}{2}\left[\frac{dn}{d\lambda}\right]_{\lambda=\lambda_0/2}\right|} \tag{2.9}$$

was calculated from Sellmeier equations for the refractive index of BBO [12] and compared with the spectral bandwidth of a 100 fs bandwidth-limited Gaussian pulse centered at 800 nm. A thickness of $L = 200$ μm was selected to best accommodate the bandwidth and peak

intensity of the unamplified laser output, while also taking into consideration the fact that the pulses reflected from the stretcher mirrors have a significantly lower peak intensity and thus will generate a weaker signal pulse. The two additional spatial dimensions of the BBO crystal were each 5 mm.

Spectra were measured by an Oriel MS125$^{\text{TM}}$ 1/8 m spectrograph (Model 77400) with 10 μm slit (Model 77222), 1200 grooves/mm grating, and LineSpec$^{\text{TM}}$ 1024 pixel CMOS linear array (Model 78866) installed[5]. This instrument was wavelength-calibrated using the known spectral lines [13] of an Oriel Hg "pencil" calibration lamp (Model 6035) inserted into the BBO crystal position. The instrument function (intensity calibration) was calculated from spectra gathered using the spectrograph and a calibrated photodiode (one for which the wavelength-dependent quantum efficiency is known) for a common tunable source. However, the associated correction to the spectra comprising the FROG traces measured in this work was found to be negligible.

A 100 fs pulse has longitudinal spatial extent of ~ 30 μm. The generation of the nonlinear signal pulse depends on positional and orientational degrees of freedom of the both the beams and the BBO crystal, as well as the arrival time of the gate pulse $E(t-\tau)$. When $\tau = 0$, the optical distances from BS to BBO of the probe $E(t)$ and gate $E(t-\tau)$ are equal, overlapping them in time. It is therefore beneficial to have a method, independent of any signal pulse, of determining what position of the corner cube reflector (CC) achieves the time overlap and defines $\tau = 0$. This was done by inserting in front of L_1 a single gold mirror large enough to reflect the parallel beams toward a screen ~ 12 meters away. After propagating through this distance, the diverging beams, crossed at a small angle and overlapping somewhat in space, create a visible interference pattern when $\tau \sim 0$. By optimizing the visibility of this interference pattern through fine adjustment of the delay, the optical path difference between two 100 fs pulse copies traveling from BS to L_1 may be reduced to ~ 1 μm.

[5]This configuration gives $\frac{\Delta\lambda}{\Delta\text{pixel}} = 0.048590$ nm/pixel.

One might expect that the optical system for collection of the signal pulses is designed according to those considerations common to all spectroscopic measurements. However, in a FROG measurement two subtle issues are alleviated by careful choice and placement of all components following the BBO crystal (see [10], pg. 278). The finite spatial extent of the beam crossing in the focal plane of L_1 results in a range of delay values for any given CC position because the wavefronts of the two pulse copies are not parallel. This is called transverse geometrical time-smearing and results in distortions in the FROG trace if not minimized. The second effect involves the direction of propagation of the signal pulse. A pulse whose phase $\phi(t)$ is asymmetric (in time) about the pulse peak has frequency content which varies in time as it passes through the crystal[6]. The signal pulse, whose propagation vector $\mathbf{k}_{\mathrm{sp}} = \mathbf{k}_1 + \mathbf{k}_2$ is given by momentum conservation, spreads into a solid angle that depends on which frequency components are overlapped in time for a particular CC position. A valid and complete FROG trace is produced only when all signal pulse rays corresponding to a particular value of delay reach the CMOS detector without being clipped. This is accomplished by careful imaging of the signal pulse onto the spectrometer slit such that rays corresponding to unwanted delay values associated with the first effect are blocked, but all spatial components associated with the second effect are collected. The relationship between the actual image size and the slit width determines the effective image size, which may be reduced to limit the effective object size to correspond to a narrowed range of delay values. See Fig. 2.6 and [10], chapter 7. All rays originating from this effective object are collected at the plane of the effective image. The use of two lenses as shown in Fig. 2.5 is a matter of convenience.

A FROG trace data set is considered properly sampled when its smallest values are 10^{-4} $\times$ the peak of the trace or less [10]. Many detectors, including the CMOS array of the spectrometer used in this work, do not have sufficient dynamic range for this criterion to be

[6]Simple example: a chirped pulse.

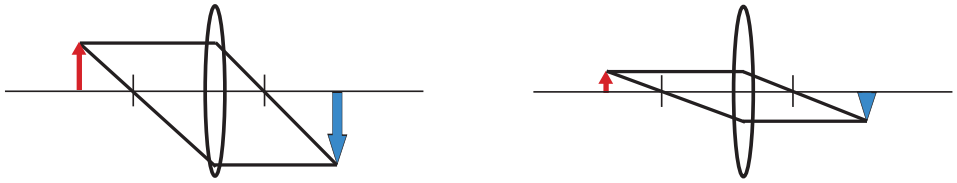

Figure 2.6: Left: The red arrow represents the spatial overlap of beams 1 and 2 in the nonlinear crystal. The blue arrow represents the signal pulse spot size at the plane of the spectrometer entrance slit. Right: The red arrow represents the effective image after being clipped by the slit. The blue arrow represents the effective object size corresponding to a narrower range of delay values and less time-smearing.

satisfied by a single FROG trace. For a given exposure time setting, a signal pulse spectrum may have regions that are (i) below the detection threshold, (ii) linear (and therefore contain useful data), or (iii) in saturation. In this work, the portions of individual FROG trace data sets corresponding to the linear response regime are identified, extracted, scaled accordingly, and then merged to form a high dynamic range FROG trace [14]. An example of this construction is given in Appendix B.

A computer algorithm incorporating the method of generalized projections was used to retrieve $E(t)$ from the high dynamic range FROG trace[7]. Comparison of the measured FROG trace with the FROG trace generated by the retrieved electric field aids the interpretation of the pulse measurement results. The FROG trace derived from the field retrieved by the algorithm will be referred to as the "retrieved FROG trace" in the discussion below.

[7]See Appendix A for description of the retrieval algorithm.

Convergence of the retrieval algorithm, which operates on a $N_\omega \times N_\tau$ grid, is quantified by the FROG error:

$$G^k = \sqrt{\frac{1}{N_\omega N_\tau} \sum_{i=1}^{N_\omega} \sum_{j=1}^{N_\tau} \left| I^{\mathrm{m}}_{\mathrm{FROG}}(\omega_i, \tau_j) - \mu\, I^k_{\mathrm{FROG}}(\omega_i, \tau_j) \right|^2} \tag{2.10}$$

where m indicates the measured FROG trace, k indicates the retrieved FROG trace at the k^{th} iteration of the algorithm, and μ is a real normalization constant that minimizes the error G^k.

2.4.3 Results and Discussion

The incident laser pulse source is described in Section 2.2. The incident pulse was first characterized in terms of FROG measurements for comparison with those taken for the case of stretched pulses. It should be noted that the ambiguity in the direction of time of the electric fields retrieved from SHG-FROG traces results in a time axis whose meaning is limited to the size of its increment. Each FROG measurement result presented below retains this feature, whereas Fig. 2.10 will summarize results more intuitively in that later times have more positive values.

Shown in Fig. 2.7 is the result of a reference measurement of the incident pulse made by inserting a general purpose silver mirror (New Focus Model 5103) in the sample position. The FROG trace derived from $E(t)$ as retrieved by the algorithm is presented for comparison with the measured FROG trace. The deviation of the incident laser pulse from an ideal Gaussian pulse is manifested in the red-shifted, low-level features in the FROG trace (particularly visible in the raw data shown in Appendix B) and is an indication of excessively large negative group-delay dispersion occurring in the laser cavity [10, 15]. It is possible that the occurrence of these lower-level pulse features affects the interference conditions at the layer

interfaces and correspondingly degrades the performance of the pulse-shaping devices, as they were optimized for a purely Gaussian incident pulse.

The experimentally measured FROG trace and the resulting retrieved fields from the pulse after reflection from F120309-2 are shown in Fig. 2.8. Data for the pulse after reflection from F120309-3 are shown in Fig. 2.9. Shown in Fig. 2.10 is a comparison between the predicted mirror performance and the measured intensities already presented in Figs. 2.7, 2.8, and 2.9 but with the measured reflectivities taken into account. Specifically, the measured incident pulse data are first normalized so that its peak is unity, and the measured reflected pulse data are subsequently scaled by the product formed by the corresponding nominal reflectivity listed in Table 2.1 and the ratio of the time-integrated incident intensity to the time-integrated reflected intensity. Also, time axes have been shifted and inverted for convenient comparison with the simulated result depicted in Fig. 2.1 and reproduced in Fig. 2.10 (a). In Figs. 2.10 (a), (b), and (c), the ratios of peak reflected intensity to peak incident intensity are 0.146, 0.210, and 0.192 respectively.

As can be seen in Figs. 2.10 (b) and 2.10 (c), both F120309-2 and F120309-3 stretch the incident pulse from $\sim$100 fs to $\sim$1 ps in a manner similar to the predicted behavior shown in Fig. 2.10 (a). However, the reflected pulses from both F120309-2 and F120309-3 exhibit a temporal profile that is more structured than the predicted reflected pulse. This is a comparison of an FDTD calculation of the reflection from an ideal device design of an assumed Gaussian incident pulse with FROG measurements of the laboratory incident and reflected pulses using actual prototypes. Possible causes of this discrepancy include imperfect layer thicknesses associated with statistical fabrication errors (see Fig. 2.2), the non-planar mirror surfaces (see Table 2.1) and the associated compensatory beam manipulation (see Section 2.4.2, first paragraph), and deviation of the incident pulse from the assumed Gaussian, as well as deviation of the refractive indices of the actual deposited materials from the assumed non-dispersive values. There are many potential sources of error in the FROG

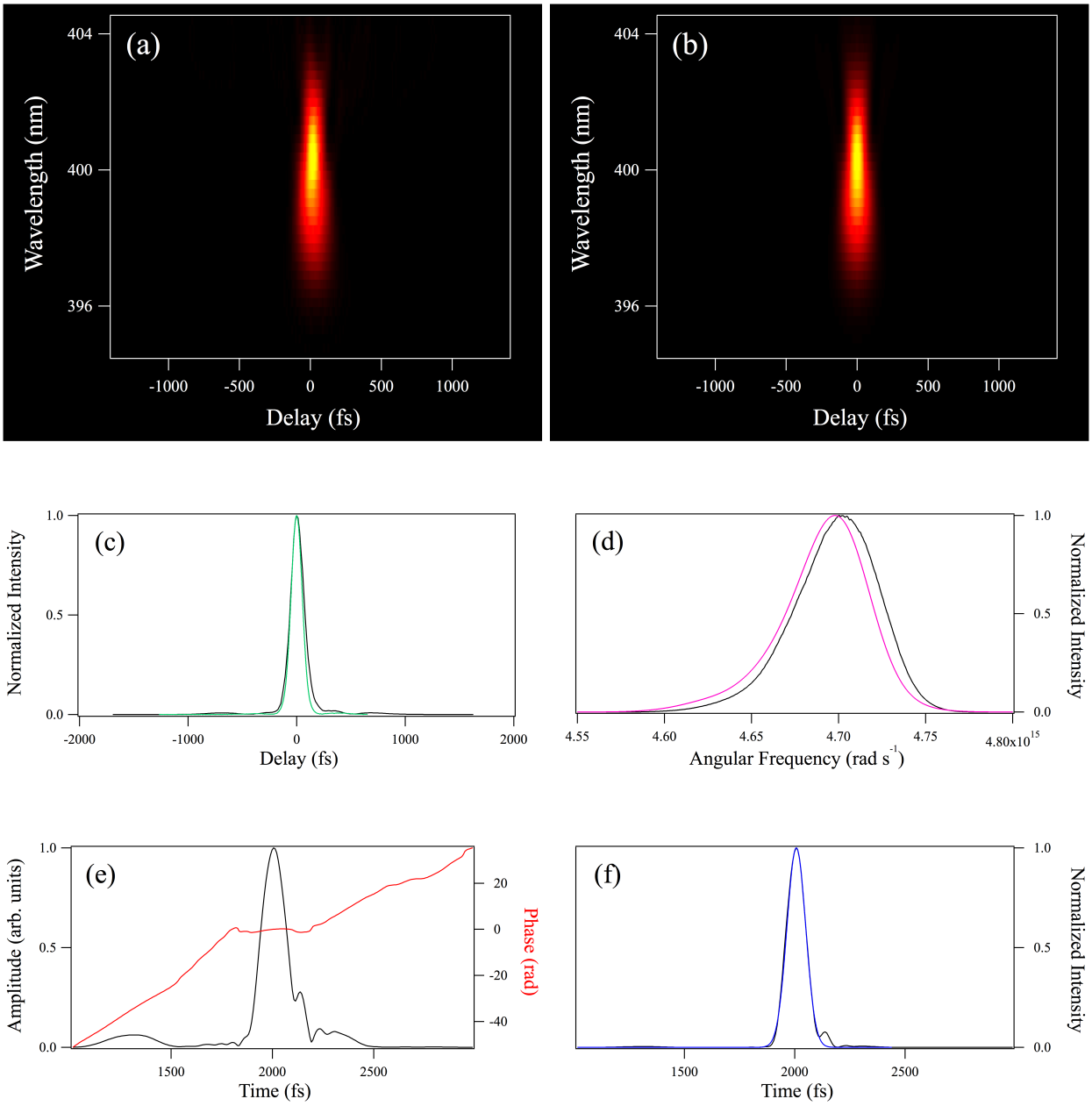

Figure 2.7: Reference pulse measurement. (a) The measured FROG trace (Trace dimensions: 256×512; G = 0.00290974). (b) The retrieved FROG trace. (c) Autocorrelation (green) and delay marginal (black). (d) Autoconvolution of the pulse spectrum (violet) and frequency marginal (black). (e) The retrieved $E(t)$. (f) The retrieved intensity (black) and the incident intensity used in the mirror design (blue) for comparison.

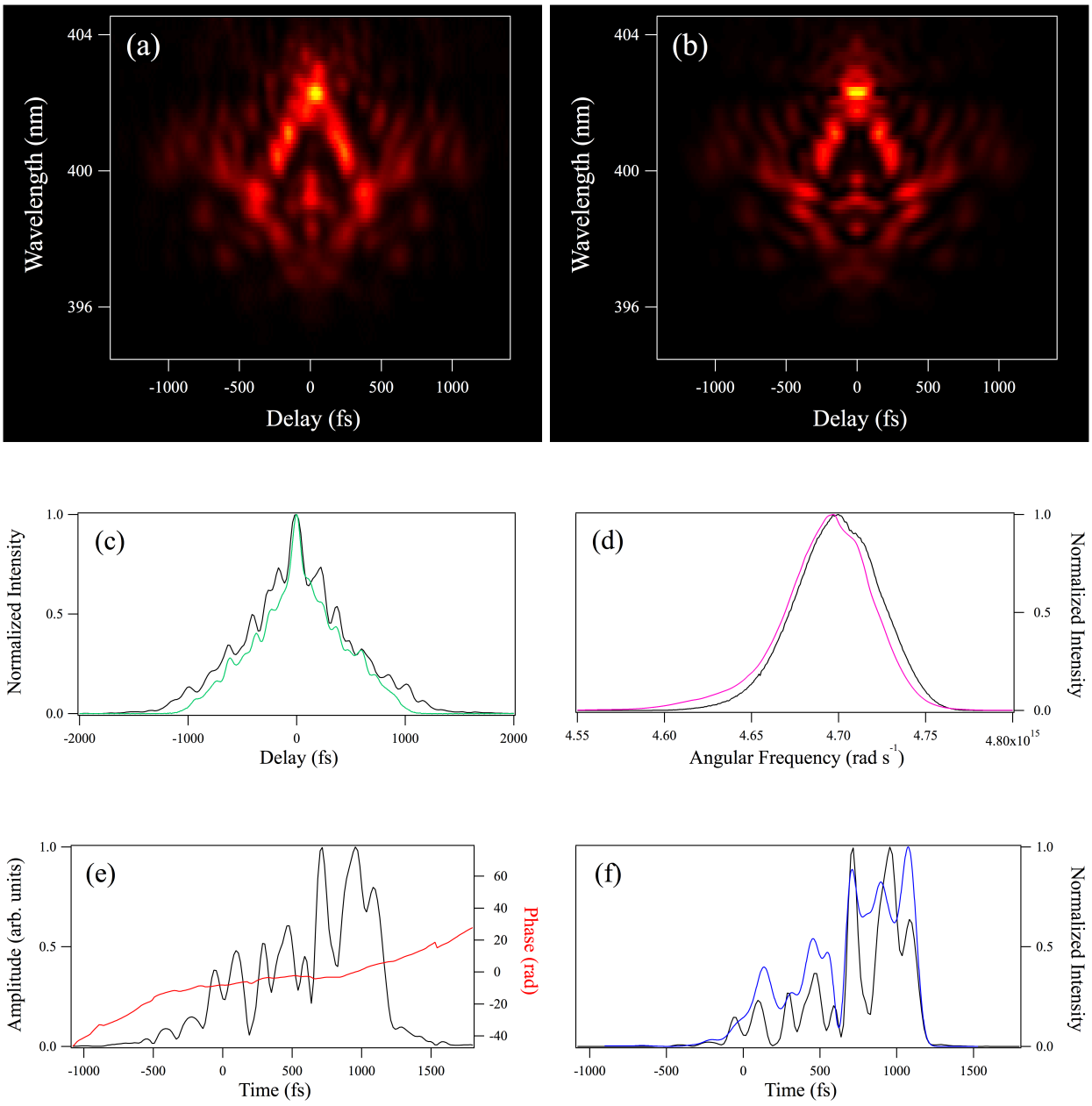

Figure 2.8: Measurement of the laser pulse reflected from F120309-2. (a) The measured FROG trace (Trace dimensions: 256 × 512; G = 0.0121446). (b) The retrieved FROG trace. (c) Autocorrelation (green) and delay marginal (black). (d) Autoconvolution of the pulse spectrum (violet) and frequency marginal (black). (e) The retrieved $E(t)$. (f) The retrieved intensity (black) and the predicted intensity envelope (blue) for comparison.

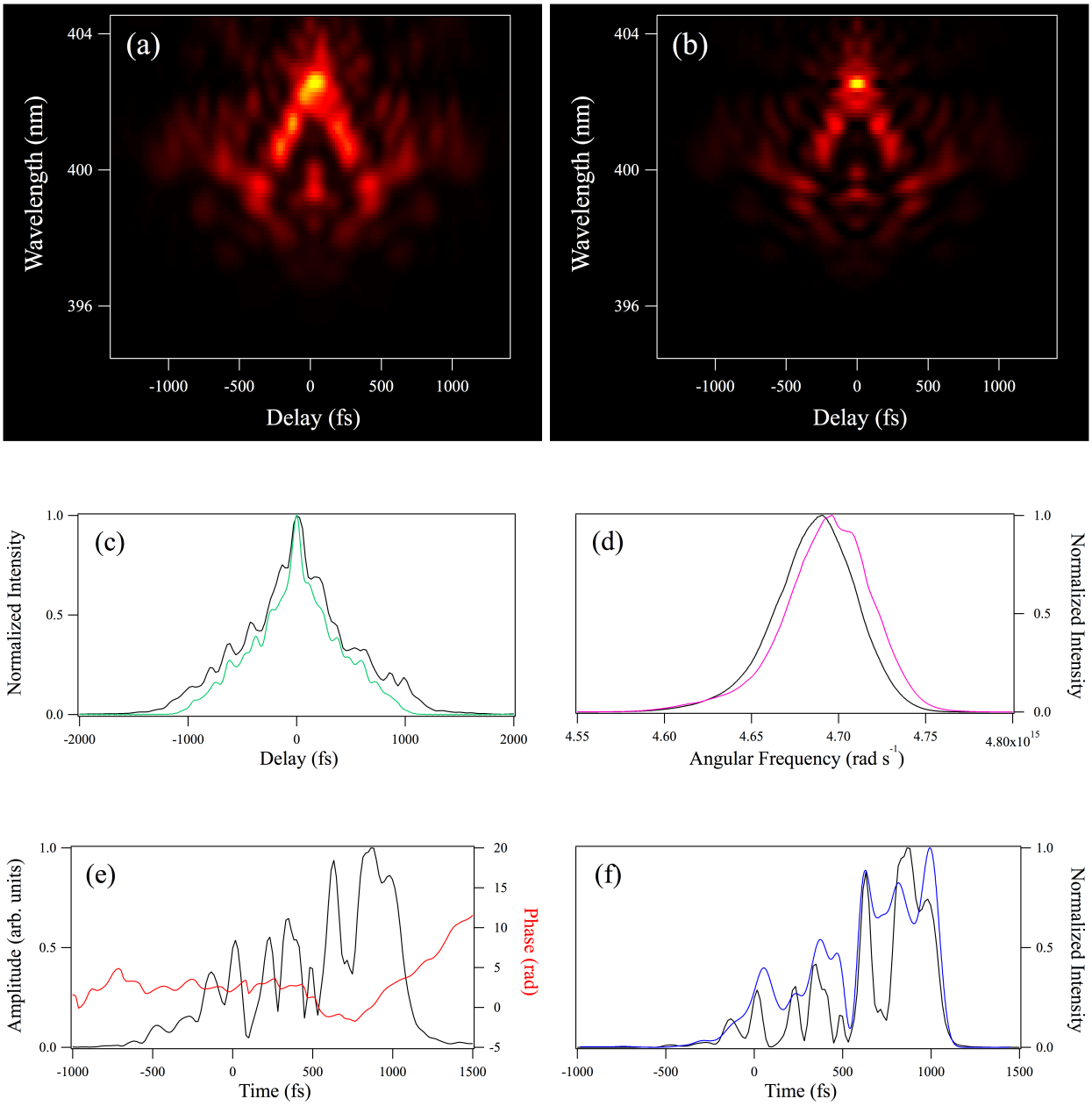

Figure 2.9: Measurement of the laser pulse reflected from F120309-3. (a) The measured FROG trace (Trace dimensions: 256 × 512; G = 0.0132273). (b) The retrieved FROG trace. (c) Autocorrelation (green) and delay marginal (black). (d) Autoconvolution of the pulse spectrum (violet) and frequency marginal (black). (e) The retrieved $E(t)$. (f) The retrieved intensity (black) and the predicted intensity envelope (blue) for comparison.

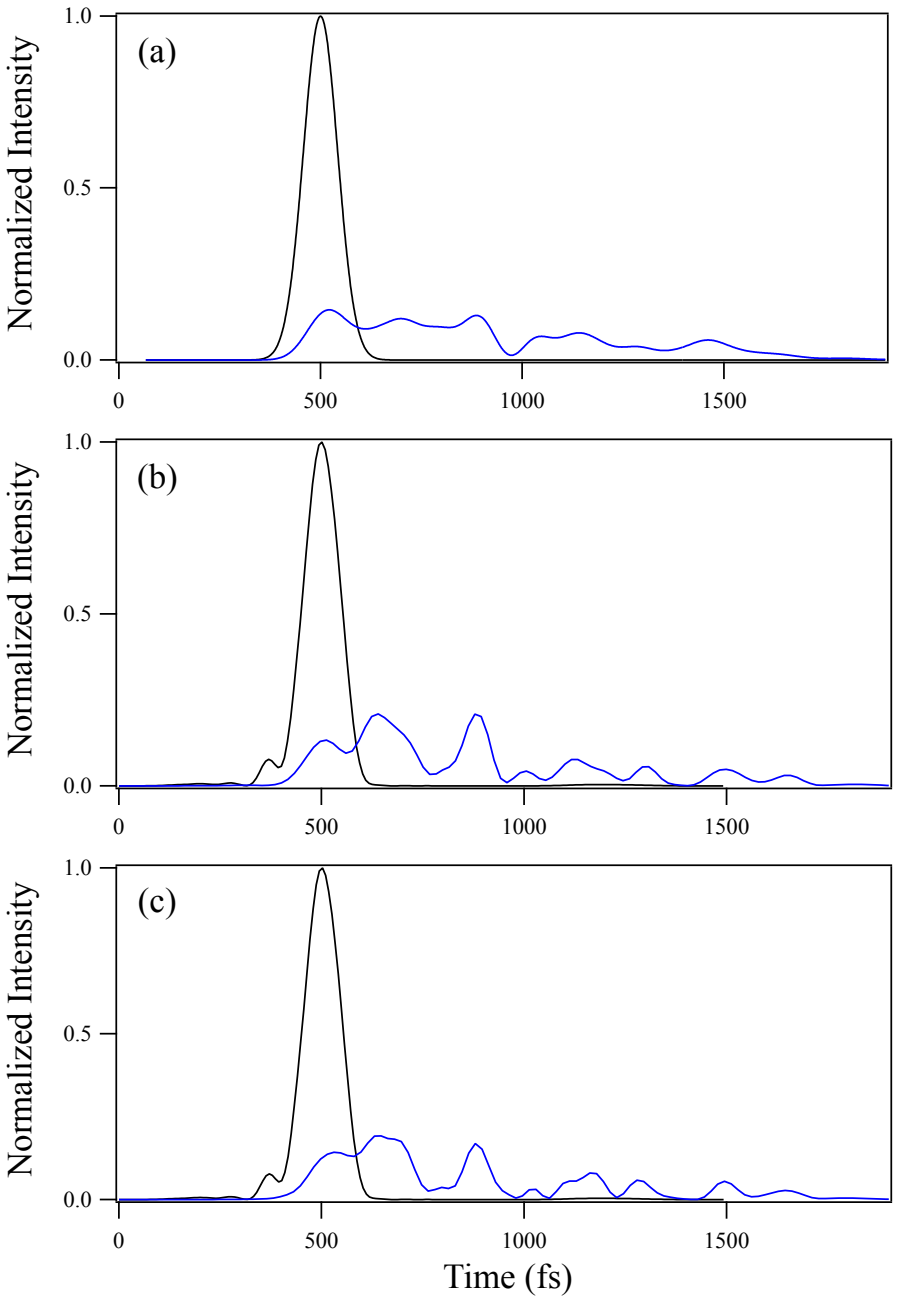

Figure 2.10: Comparison of predicted and measured intensity temporal profiles:
(a) The incident (black) and reflected (blue) intensity calculated by the FDTD method.
(b) The measured incident (black) and reflected (blue) intensity for the case of F120309-2.
(c) The measured incident (black) and reflected (blue) intensity for the case of F120309-3.

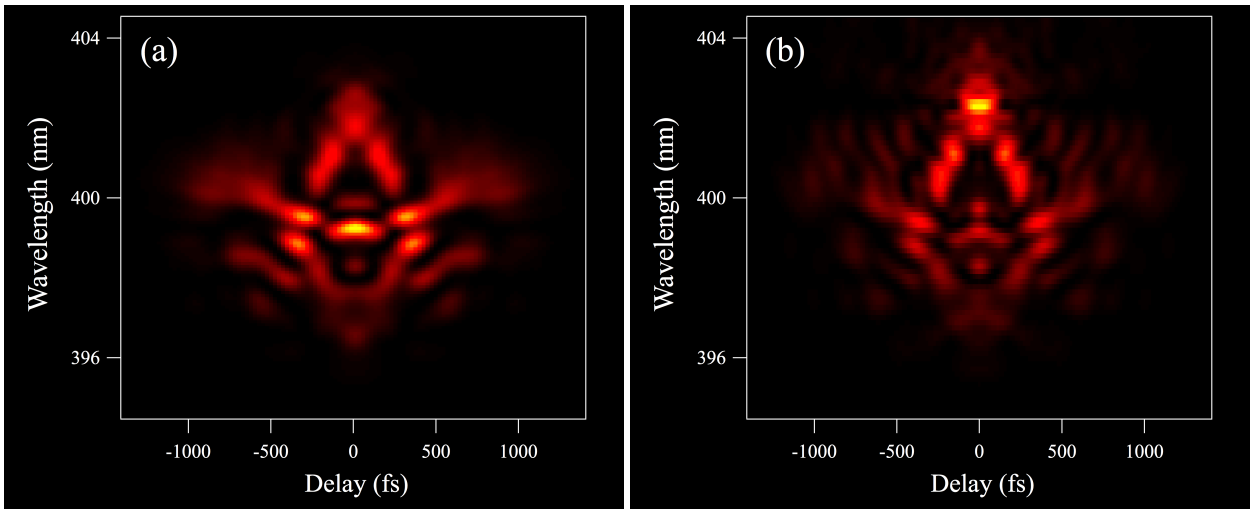

Figure 2.11: Comparison of results in the time-frequency domain. (a) FROG trace generated by the pulse field reflected from the as-designed mirror in an FDTD calculation. (b) FROG trace generated by the pulse field retrieved from the measured FROG trace for the case of F120309-2.

pulse measurement as discussed in Section 2.4.2. Most notably, the nonlinear crystal quality, thickness, and orientation relative to the crossed beam geometry all have bearing on the reliability of the results. Insight into whether the discrepancy is due to deficient device performance or errors in the FROG pulse measurement may be gained from considering additional quantities derivable from the result predicted by FDTD calculations, and further examining the data already presented.

A FROG trace may be generated from the FDTD data corresponding to the pulse reflected from the ideal design using Eqs. 2.5 and 2.6. In Fig. 2.11, this trace is compared with the retrieved trace for the case of mirror F120309-2, which is reproduced from Fig. 2.8 (b). This corresponds to a comparison of the blue curves in Fig. 2.10 (a) and (b). The traces share many of the same features. However, the trace corresponding to the measurement contains a red-shifted peak, and lacks the strong features near 399 nm. There are two likely causes for

this trend. The first is the use of a nonlinear crystal with insufficient phase-matching bandwidth. Indeed, the recommended crystal thickness for such a measurement is 100 μm – one half the thickness of the crystal used in this work (see [10], pg. 129). However, the FROG trace frequency marginal and independently measured pulse spectrum autoconvolution are seen to be in excellent agreement in Fig. 2.8 (d). The ratio of these quantities may be used to correct a FROG trace exhibiting this flaw [10]. The fact that this ratio is approximately constant here suggests that this measurement was not significantly hindered by insufficient phase-matching bandwidth. The other likely cause is a neglect of the spectral response of the spectrometers used. If their instrument functions each happen to exhibit an increasing sensitivity with wavelength in the relevant spectral regions (around 400 nm for the nonlinear signal pulse spectrum, around 800 nm for the fundamental pulse spectrum), then the quantities plotted in Fig. 2.8 (d) may agree while suffering from a mutual flaw. This possibility was eliminated by measuring the instrument function of the spectrograph used to measure all FROG traces, with hopes of correcting them. However, a visual comparison of FROG traces with and without the measured instrument function correction determined it to be negligible.

2.5 Conclusions

The preceding results and considerations led to the conclusion that the noticeable disparity between predicted and measured temporal intensity profiles for the stretched pulses is due primarily to the characteristics of the particular specimens as opposed to flaws in the pulse measurement. Specifically, the curved surfaces may result from the use of relatively thin substrates. Thicker, more expensive substrates are commonly found in more robust optics with better operating parallelism. In addition, the prototypes may have been fabricated with the substrate very close to the deposition source in order to increase the flux density,

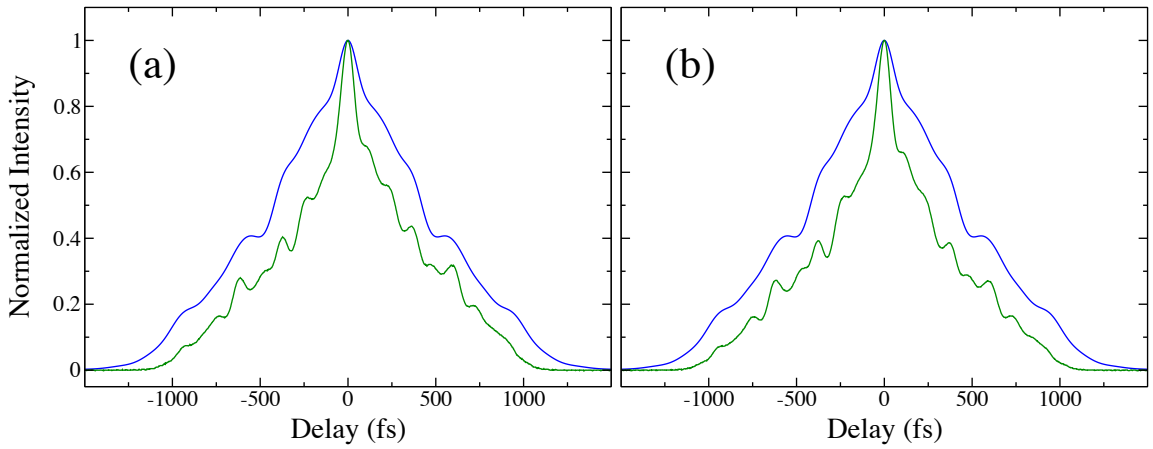

Figure 2.12: Comparison of intensity autocorrelations: Autocorrelation of the temporal intensity envelope calculated by the FDTD method (blue) and measured autocorrelations (green) for the device prototypes F120309-2 (a) and F120309-3 (b).

providing savings in terms of time and material. This would be expected to produce a curved surface if the separation between the deposition source and a point on the substrate surface (and therefore the local flux density) varies appreciably as a function of radial distance from the center of the optic.

FROG trace delay marginals have been compared to independently measured autocorrelations in Figs. 2.8 and 2.9. As a final remark, the autocorrelations measured using the commercial device are reproduced in Fig. 2.12 along with the autocorrelation calculated using the temporal intensity profile calculated by the FDTD method, which is the blue curve shown in Figs. 2.1 and 2.10 (a). Each curve is normalized to its peak. The point here is that additional structure in the experimental intensity profile is manifested in the measured autocorrelations by their additional structure and the associated "coherence spike" [10]. Also, these data are not derived from FROG measurements and are therefore not subject to the same scrutiny. While the intensity autocorrelation does not determine the form of the intensity structure, it does reveal which pulse (simulated or measured) is more structured. This

observation lends additional credence to the measurements presented in this chapter that do in fact provide the complete intensity structure – the FROG traces and pulse fields retrieved from them.

Chapter 3

Computational Studies of Laser Beam Coupling in Hybrid Liquid Crystal-Photorefractive Cells

3.1 Introduction

Photorefractive effects were first reported in 1966 by Ashkin *et al.* [16], who observed optically-induced spatial inhomogeneities in the refractive index of $LiNbO_3$ and $LiTaO_3$. That discovery would lead to a branch of nonlinear optics that has motivated extensive studies in optical engineering and materials research and continues to develop [17].

Nonlinear optical effects are often interesting from an applied science/optical engineering standpoint in that they may be utilized to control or otherwise modify light by virtue of self-action. For example, an intensity-dependent refractive index change $n(I) = n_0 + \Delta n(I)$ may cause self-focusing and affect the propagation of a beam, which has higher intensity at its spatial center. However, these effects, having their origins in higher-order terms of a

polarization $P = \varepsilon_0 \sum_i \chi^{(i)} E^i$, generally have very small coefficients and require high intensities.

Photorefractive behavior in materials cannot be cast in the traditional formalism of nonlinear optics described briefly in Section 1.1 [18]. This is demonstrated most clearly by the fact that the field E directly responsible for Δn is not the optical field. E arises from a fortuitous sequence of physical processes that happens to have as its origin a spatially modulated optical intensity. For this reason, photorefractivity is independent of the overall light intensity (barring extreme conditions), but dependent on the degree to which it is spatially modulated. The basic requirements are that the material be photoconductive and exhibit the linear electro-optic effect. High intensities are not required. This research field maintains the attention of optical scientists and engineers because 1) the effects are self-induced and 2) the coefficients that determine the magnitude of the underlying optical effect are large as compared with those that determine, for example, the optical Kerr effect.

The photorefractive effect, which will be described in more detail in Section 3.3, has found application in many technological settings. Optical data storage is facilitated by holographic memory [19]. Weak optical images may be coupled in a photorefractive to a stronger pump beam and therefore amplified [20]. Photorefractive phase conjugate mirrors are capable of correcting beam distortions occurring in laser cavities due to unwanted nonlinear effects at high intensities [21]. Self-organized laser cavities have been achieved using a photorefractive crystal [22] as an adaptive Fabry-Pérot filter to select and lock-in particular longitudinal or transverse cavity modes [23]. Because the change imparted by the crystal to the cavity is optically-induced, the wavelength of a cavity can be selected by temporary injection from a master laser [24]. Thus, the stable operation of several slave lasers at a given wavelength may be set by a common tunable master laser. The value of the self-induced optical effects occurring in photorefractives is reflected by the breadth of these adaptive technologies.

Two-beam coupling, which is the subject of the rest of this chapter, is derived from the refractive index grating written to a photorefractive, and is optimized when a device can operate in the Bragg diffraction regime such that one beam interferes constructively with the Bragg reflection of another. Hybrid devices may be constructed from layers of organic and inorganic crystals and glasses, photoconductive polymers, and/or liquid crystals. This chapter describes a numerical investigation into the two-beam coupling gain characteristics of such a device. The exponential gain coefficient is defined as

$$g = \frac{1}{L} \ln G \tag{3.1}$$

where L is the sample thickness and G is the gain, which may be defined differently in different contexts. Theoretical calculations might consider G to be a ratio of beam amplitudes before and after passing through a sample, while experiments might consider G to be the ratio of the signal beam's power before and after adding the pump beam, whose energy is coupled into the signal beam.

3.2 Liquid Crystals

Liquid crystals were discovered in the late 19th century by Reinitzer and Lehmann [25–27]. These "mesomorphic phases" constitute a distinct state of molecular aggregation intermediate between crystalline solids and amorphous liquids from which they may be distinguished on a basic level in terms of their spontaneous order: Solids possess, and liquids lack, both translational and orientational order, whereas liquid crystals possess orientational but lack full translational order. They are classified most broadly in terms of the dimensionality of the translational order they do possess, which is generally determined by temperature, concentration, etc. for a given molecular species or mixture of species. *Columnar* phases are

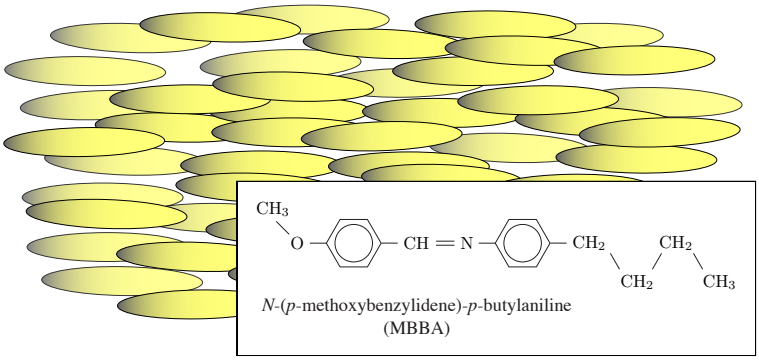

Figure 3.1: Nematic liquid crystal. The nematic phase of the MBBA molecule occurs between 20° C and 47° C.

distinct from solid-state crystals in that one-dimensional mutually parallel channels exist in the bulk material through which the molecules may flow. Liquid crystal (LC) molecules in a *smectic* phase retain long-range orientational order, but have freedom to flow in planes normal to some direction. When the flow of orientationally-ordered LC molecules is not limited in any particular direction, the phase is referred to as *nematic*. Nematics were used in the first observation of photorefractivity in liquid crystals by Rudenko and Sukhov in 1993 [28–30]. An example of a nematic mesogen is MBBA and is shown in Fig. 3.1. These distinctions have bearing on the optical properties of these materials in that a LC material at steady state behaves as an anisotropic solid with a spatially-dependent optical axis. This local optical axis is a unit vector termed the "director", and determines the spatial dependence of the relative permittivity tensor

$$\varepsilon_{ij} = \varepsilon_{\perp}\,\delta_{ij} + \varepsilon_{\mathrm{a}}\,n_i n_j \tag{3.2}$$

where $\mathbf{n}$ is the director, δ_{ij} is the Kronecker delta, and $\varepsilon_{\mathrm{a}} = \varepsilon_{\parallel} - \varepsilon_{\perp}$ is the dielectric anisotropy of the LC with distinct permittivities being experienced by components of a propagating

electric field along ($\varepsilon_{\|}$) and normal to ($\varepsilon_{\perp}$) the director. Typical values for ε_{a} are on the order of 5 to 10 [31]. Choosing the director to lie in the yz-plane in an experimental geometry with no x-dependence, this becomes

$$\hat{\varepsilon} \;=\; \begin{pmatrix} \varepsilon_{\perp} & 0 & 0 \\ 0 & \varepsilon_{\perp} + \varepsilon_a \cos^2\vartheta(y,z) & \frac{\varepsilon_a}{2}\sin 2\vartheta(y,z) \\ 0 & \frac{\varepsilon_a}{2}\sin 2\vartheta(y,z) & \varepsilon_{\perp} + \varepsilon_a \sin^2\vartheta(y,z) \end{pmatrix} \tag{3.3}$$

where $\vartheta(y,z)$ is the angle $\in [\,-\pi,\,\pi\,]$ between $\mathbf{n}$ and $\hat{\mathbf{y}}$. The director $\mathbf{n} = \mathbf{n}(y,z)$ is subject to highly non-local effects. Forces and torques at one side of a container may be communicated across the bulk material via local interactions between clumps of molecules. Van der Waals interactions between the container surface and LC molecules may cause a *pretilt* at the container surface. To calculate the steady-state solution for the director angle field ("director profile") throughout the container, an appropriate free energy functional must be minimized subject to boundary conditions imposed, for example, by the pretilt induced by the container walls. This free energy functional may include terms like the flexoelectric energy

$$F_{\mathrm{f}} = -\int (\mathbf{P}_{\mathrm{f}} \cdot \mathbf{E})\; dV \tag{3.4}$$

where $\mathbf{P}_{\mathrm{f}}$ is written in terms of the $\mathbf{n}(y,z)$ as

$$\mathbf{P}_{\mathrm{f}} = e_{11}\,\mathbf{n}\,(\boldsymbol{\nabla}\cdot\mathbf{n}) - e_{33}\,\mathbf{n}\times(\boldsymbol{\nabla}\times\mathbf{n}) \tag{3.5}$$

with coefficients e_{11} and e_{33} generally being determined empirically: and $\mathbf{E} = \mathbf{E}(y,z)$ is some externally applied field.

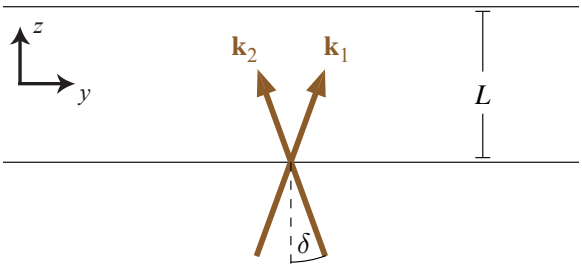

Figure 3.2: Beam geometry and spatial coordinates used throughout this chapter.

3.3 The Photorefractive Space-charge Field and its Influence on the Nematic LC Director

The interference pattern between two crossed laser beams may be described in terms of a modulation parameter $\mathcal{M} \in \mathbb{C}$ as follows: The electric field vectors of the two waves are represented as (see Fig. 3.2):

$$\mathbf{E}_1 = A_1 \, e^{i(\mathbf{k}_1 \cdot \mathbf{r} - \omega_1 t)} \, (\cos(\delta) \, \hat{\mathbf{y}} - \sin(\delta) \, \hat{\mathbf{z}} \,) \tag{3.6}$$

and

$$\mathbf{E}_2 = A_2 \, e^{i(\mathbf{k}_2 \cdot \mathbf{r} - \omega_2 t)} \, (\cos(\delta) \, \hat{\mathbf{y}} + \sin(\delta) \, \hat{\mathbf{z}} \,) \tag{3.7}$$

where A_1 and A_2 are complex beam amplitudes. If the waves have the same frequency $\omega_1 = \omega_2$, then the spatial distribution of the intensity corresponding to the total electric field is stationary [18] and may be written as

$$I \; = \; \frac{1}{2} c n \epsilon_0 \, (\mathbf{E}_1 + \mathbf{E}_2) \cdot (\mathbf{E}_1 + \mathbf{E}_2)^* \; \propto \; (I_1 + I_2) \left[1 + \frac{1}{2} \left(\mathcal{M} \, e^{iqy} + \mathcal{M}^* e^{-iqy} \right) \right] \tag{3.8}$$

where $I_1 = A_1 A_1^*$, $I_2 = A_2 A_2^*$, $q = k_{1y} - k_{2y} = 2k\sin(\delta)$ and $\mathcal{M} = \frac{2\cos(2\delta)}{I_1 + I_2} A_1 A_2^*$. Writing the modulation parameter as $\mathcal{M} = m\, e^{i\phi}$ and ignoring the prefactors in the relationship between intensity and electric field magnitude, Eq. 3.8 becomes

$$I = (I_1 + I_2)\,[\,1 + m\cos(qy + \phi)\,] \tag{3.9}$$

which has maxima and minima

$$I^{(\max)} = (I_1 + I_2)\,[\,1 + m\,] \tag{3.10}$$

and

$$I^{(\min)} = (I_1 + I_2)\,[\,1 - m\,] \tag{3.11}$$

so that the real parameter m is given by

$$m = \frac{I^{(\max)} - I^{(\min)}}{I^{(\max)} + I^{(\min)}} \tag{3.12}$$

and it is clear that the phase ϕ of $\mathcal{M}$ determines the phase of the interference pattern, which varies in a sinusoidal manner as a function of y, relative to the coordinate origin.

A grating vector may be defined as $\mathbf{q} = \frac{2\pi}{\Lambda}\,\hat{\mathbf{y}}$ to describe the direction and spatial period of a y-directed refractive index modulation with spatial period Λ. Maximal coupling between beams is achieved for a Bragg-matched diffraction geometry, which refers to the condition that the grating vector satisfies

$$\mathbf{q} = \mathbf{k}_1 - \mathbf{k}_2. \tag{3.13}$$

Eq. 3.13 holds when the refractive index modulation $\Delta n = \Delta n(y)$ constituting the phase grating has the same spatial periodicity as does the interference pattern created by the crossed beams. This relationship was suggested by the introduction of the symbol q in

Eq. 3.8, and inherently applies when the refractive index modulation is derived from the intensity distribution in the beam crossing. For example, the optical Kerr effect may induce a refractive index $n = n_0 + \Delta n(y)$ with $\Delta n(y) \propto I$. However, this alone is not enough to result in energy transfer between beams. It can be shown [18] that there is no energy transfer between beams with $\omega_1 = \omega_2$ in such a material. In this Kerr medium the spatial phase of the refractive index modulation equals the phase ϕ of the interference pattern. Energy transfer between beams of the same frequency is facilitated by the phase shift between these patterns that arises from the distinct physical processes occurring in photorefractive materials.

Photorefractive behavior may arise in a material that exhibits photoconductivity and the linear electro-optic effect [32]. See Fig. 3.3. In regions of comparatively high intensity, photoionization occurs at donor impurity sites with density N_d. Charge carriers subsequently diffuse to acceptor sites with density N_a in the lower-intensity regions, leaving behind positively charged holes. This charge separation gives rise to an electric field that is static in time, oscillating as a function of position, and referred to as the "space-charge field". The magnitude of this field depends on the specific material properties and geometry. In this work[1], the space-charge field magnitude takes the diffusion-dominated form [33]:

$$E_{0\mathrm{sc}}(q) = \frac{-iE_\mathrm{d}}{1 + \frac{E_\mathrm{d}}{E_\mathrm{q}}}, \qquad E_\mathrm{d} = q\frac{k_\mathrm{B}T}{e}, \qquad E_q = \left(1 - \frac{N_\mathrm{a}}{N_\mathrm{d}}\right)\frac{e\,N_\mathrm{a}}{\varepsilon_0\,\varepsilon_\mathrm{Ph}\,q} \tag{3.14}$$

where the diffusion field E_d is determined for a given grating wave number $q = |\mathbf{q}|$ and temperature T by the elementary charge e and Boltzman's constant k_B, and the saturation field E_q depends on ε_Ph, the material's dielectric constant. The space-charge field, according to the linear electro-optic effect [34], induces a refractive index modulation $\Delta n(y)$ that is sensitive to the sign of $\mathbf{E}_\mathrm{sc}$ and therefore has the same spatial period as does the interference

[1]The minus sign in $E_{0\mathrm{sc}}(q)$ corresponds to negative charge carriers and the particular coordinate system used in this work.

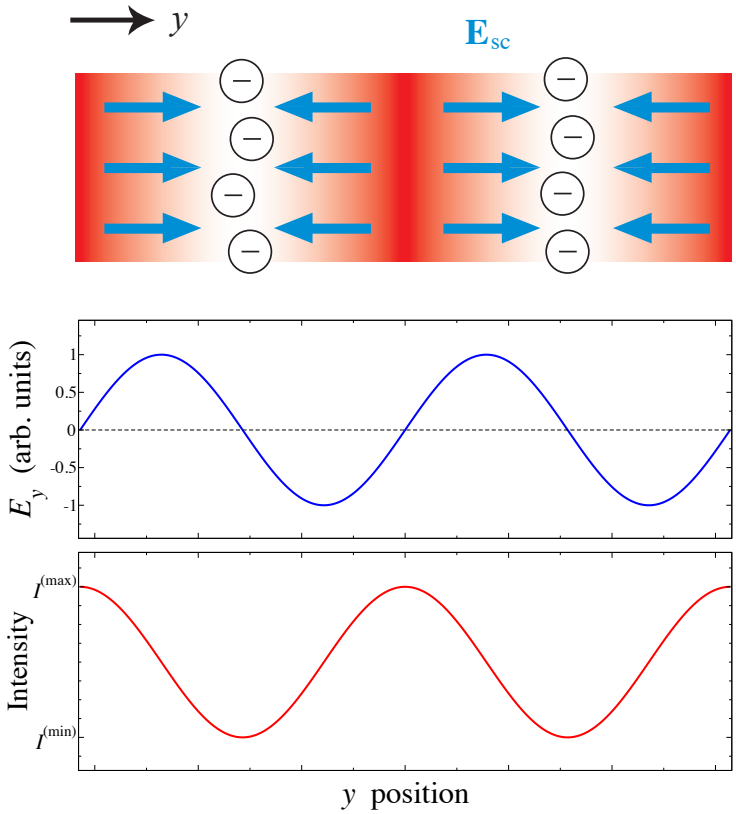

Figure 3.3: Schematic of the construction of a space-charge electric field $\mathbf{E}_{sc}$ (blue arrows) due to photoionization and diffusion of charge carriers (electrons here) from high-intensity regions (red) to low-intensity regions(white).

pattern, but phase-shifted by $\frac{\pi}{2}$. It is this modification of the refractive index as a function of space that is responsible for the many applications that utilize photorefractive materials.

For the case of a finite material slab, the space-charge field also permeates to the region of space surrounding the slab. This field can influence the properties of a material placed adjacent to the photorefractive. Shown in Fig. 3.4 is a schematic of a hybrid organic-inorganic device fashioned from a liquid crystal (LC) layer sandwiched between two photorefractive windows. This device has demonstrated gain coefficients of 600 cm^{-1} as compared with 10 – 100 cm^{-1} typical for purely inorganic photorefractive devices [35]. The beam and sample

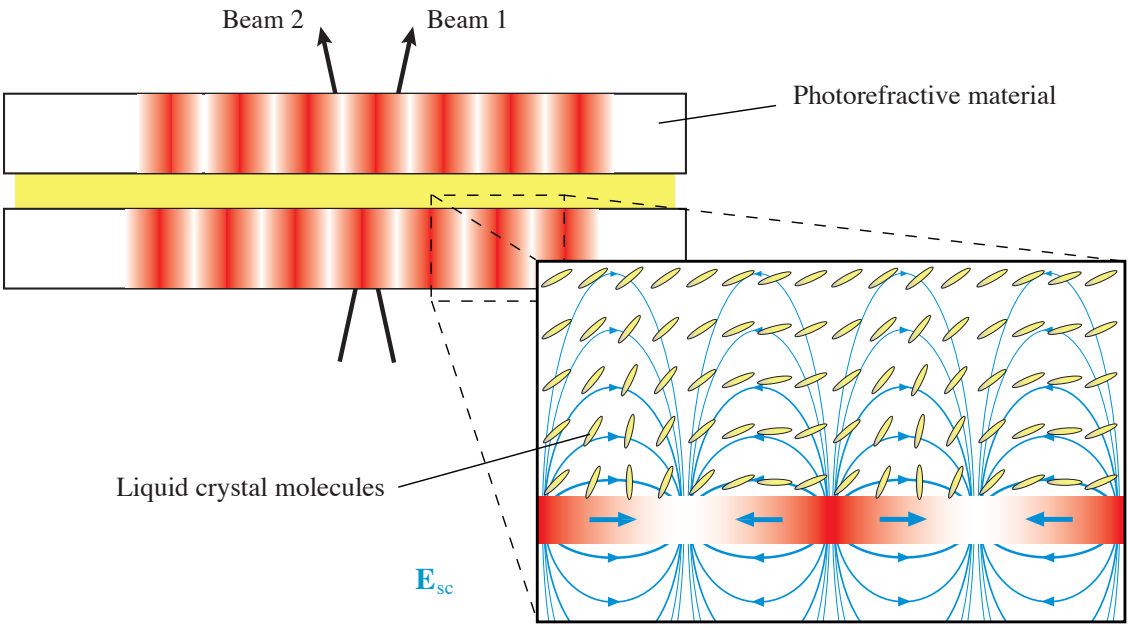

Figure 3.4: Hybrid organic-inorganic beam coupling device. The liquid crystal director is reoriented by the space-charge field $\mathbf{E}_{sc}$ such that the free energy associated with this mesomorphic material is minimized. The magnitude of the reorientation is exaggerated here, and $\mathbf{E}_{sc}(y, z)$ is depicted in the abstract.

geometry are such that the problem may be treated in two spatial dimensions, and effects associated with finite spatial beams are not expected to have any importance. Despite these simplifications, accounting for this gain theoretically has proven difficult. The equations that describe the space-charge field's influence on the LC material, the resulting influence the LC material has on beam propagation, and the resulting modifications to the interference patterns in each window constitute a complex coupled problem that must be solved self-consistently. For example, neglecting the feedback on $\mathbf{E}_{sc}$ due to the reorientation it produces in the LC director and the associated flexopolarization, which itself would, strictly speaking,

require a self-consistent approach, the space-charge field takes the form [35]

$$\begin{aligned}\mathbf{E}_{\mathrm{sc}}(y,z) = & \\ & \frac{E_{0\mathrm{sc}}(q)}{4}\left[(\mathcal{M}_{\mathrm{F}}+\mathcal{M}_{\mathrm{B}})\,\frac{\cosh(\tilde{q}z)}{\cosh(\tilde{q}L/2)}+(\mathcal{M}_{\mathrm{B}}-\mathcal{M}_{\mathrm{F}})\,\frac{\sinh(\tilde{q}z)}{\sinh(\tilde{q}L/2)}\right]\exp(iqy)\;\hat{\mathbf{y}} \\ & +\frac{E_{0\mathrm{sc}}(q)}{4i}\left[(\mathcal{M}_{\mathrm{F}}+\mathcal{M}_{\mathrm{B}})\,\frac{\sinh(\tilde{q}z)}{\cosh(\tilde{q}L/2)}+(\mathcal{M}_{\mathrm{B}}-\mathcal{M}_{\mathrm{F}})\,\frac{\cosh(\tilde{q}z)}{\sinh(\tilde{q}L/2)}\right]\sqrt{\frac{\tilde{\varepsilon}_{\parallel}}{\tilde{\varepsilon}_{\perp}}}\exp(iqy)\;\hat{\mathbf{z}} \\ & +\ \text{c.c.}\end{aligned} \tag{3.15}$$

where subscripts on complex modulation parameters refer to the "Front" (entrance) and "Back" (exit) photorefractive windows, and all other parameters are defined in Section 3.4. This field should in principle be used in the expression for the appropriate free energy to yield the director profile, which in turn determines the LC permittivity tensor that effects beam propagation and therefore the interference pattern in the photorefractive. Rendering such a problem tractable requires making various approximations at various stages of the calculation. In order to shed light on the effect of approximations associated with the evolution of the electromagnetic fields corresponding to the propagation of and coupling between beams, the experiment was simulated via finite-difference time-domain (FDTD) calculations of two beam coupling in the LC layer. Methods used and results obtained are the subject of the remainder of this chapter.

3.4 Liquid Crystal Director Profile

The director $\mathbf{n} = \mathbf{n}(y, z)$ is obtained from minimization of the total free energy functional $F = \sum_i F_i$, thus balancing the torques associated with the Frank-Oseen elastic energy

$$F_{\rm el} = \frac{1}{2} \int \left[K_{11} \left(\boldsymbol{\nabla} \cdot \mathbf{n} \right)^2 + K_{22} \left(\mathbf{n} \cdot \boldsymbol{\nabla} \times \mathbf{n} \right)^2 + K_{33} \left(\mathbf{n} \times \boldsymbol{\nabla} \times \mathbf{n} \right)^2 \right] dV \tag{3.16}$$

and the applied field $\mathbf{E}_{\rm sc}(y, z)$. Here, K_{11}, K_{22}, and K_{33} are the splay, twist, and bend elastic constants, respectively. The two-dimensional system geometry, which confines $\mathbf{n}$ to the yz-plane, makes the second term in this expression identically zero. The influence of $\mathbf{E}_{\rm sc}$ is dominated by the flexoelectric energy term

$$\begin{aligned} F_{\rm f} &= - \int \left(\mathbf{P}_{\rm f} \cdot \mathbf{E}_{\rm sc} \right) dV \\ &= - \int \left[e_{11} \ \left(\mathbf{E}_{\rm sc} \cdot \mathbf{n} \right) \left(\boldsymbol{\nabla} \cdot \mathbf{n} \right) + e_{33} \, \mathbf{E}_{\rm sc} \cdot \left(\mathbf{n} \cdot \boldsymbol{\nabla} \right) \mathbf{n} \right] dV \end{aligned} \tag{3.17}$$

where e_{11} and e_{33} are the flexoelectric coefficients. See [35] for details. Expanding the direction cosines and keeping terms in small ϑ up to first order, the y-dependence of the solution to the Euler-Lagrange equation

$$\frac{\partial F}{\partial \vartheta} - \frac{d}{dy} \frac{\partial F}{\partial \vartheta_y} - \frac{d}{dz} \frac{\partial F}{\partial \vartheta_z} = 0 \qquad \text{with} \qquad \vartheta_y \equiv \frac{d\vartheta}{dy}, \quad \vartheta_z \equiv \frac{d\vartheta}{dz} \tag{3.18}$$

is Fourier expanded as

$$\vartheta(y, z) = \theta_0(z) + \left[\, \theta(z) \exp(iqy) + \text{c.c.} \, \right] \tag{3.19}$$

where higher-order Fourier components for the modulation in y are neglected according to the so-called "first spatial harmonic approximation" [36]. The resulting solution, which

assumes infinitely strong anchoring of the pretilts θ_{F} and θ_{B} at the front and back window surfaces bounding the LC layer of thickness L, is given by

$$\theta_0(z) = s + pz \qquad \text{with} \qquad s = \frac{\theta_{\mathrm{F}} + \theta_{\mathrm{B}}}{2}, \quad p = \frac{\theta_{\mathrm{B}} - \theta_{\mathrm{F}}}{L} \tag{3.20}$$

and

$$\theta(z) = \frac{E_{0\mathrm{sc}}(q)}{2} \left[\mathcal{M}_{\mathrm{F}}\, G_{\mathrm{F}}(z) + \mathcal{M}_{\mathrm{B}}\, G_{\mathrm{B}}(z) \right] \tag{3.21}$$

where

$$\begin{aligned} G_{\mathrm{F}}(z) = \frac{r\tilde{q}}{\tilde{q}^2 - q_1^2} \Bigg\{ & \left(1 + \frac{i2p\,(\tilde{q}^2 + q^2)}{q\,(\tilde{q}^2 - q_1^2)} \right) \left[e^{-q_1(z+L/2)} - e^{-\tilde{q}(z+L/2)} \right] \\ & - \frac{i\,(\tilde{q}^2 + q^2)}{q\tilde{q}} \left[\theta_0(z) e^{-\tilde{q}(z+L/2)} - \theta_{\mathrm{F}} e^{-q_1(z+L/2)} \right] \Bigg\}, \end{aligned} \tag{3.22}$$

$$\begin{aligned} G_{\mathrm{B}}(z) = \frac{r\tilde{q}}{\tilde{q}^2 - q_1^2} \Bigg\{ & \left(1 + \frac{i2p\,(\tilde{q}^2 + q^2)}{q\,(\tilde{q}^2 - q_1^2)} \right) \left[e^{\,\tilde{q}(z-L/2)} - e^{\,q_1(z-L/2)} \right] \\ & - \frac{i\,(\tilde{q}^2 + q^2)}{q\tilde{q}} \left[\theta_0(z)\, e^{\,\tilde{q}(z-L/2)} - \theta_{\mathrm{B}}\, e^{\,q_1(z-L/2)} \right] \Bigg\}, \end{aligned} \tag{3.23}$$

and where the quantities r, $\tilde{q}$, and q_1 are defined as

$$r = \frac{e_{11} + e_{33}}{K_{11}}, \qquad \tilde{q} = q\sqrt{\frac{\tilde{\varepsilon}_{\parallel}}{\tilde{\varepsilon}_{\perp}}}, \qquad q_1 = q\sqrt{\frac{K_{33}}{K_{11}}}. \tag{3.24}$$

$\tilde{\varepsilon}_{\parallel}$ and $\tilde{\varepsilon}_{\perp}$ are the low-frequency permittivities of the LC material along and normal to the director, respectively. After expanding Eq. 3.19 using Eqs. 3.20 – 3.24 in order to work with real quantities[2] in the context of an FDTD numerical calculation, the director profile $\vartheta(y, z)$

[2]This expansion is given for reference in Appendix D.

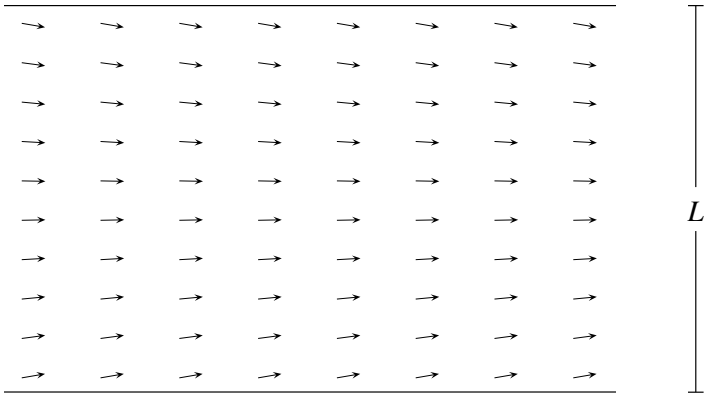

Figure 3.5: Vector field depiction of the LC director profile $\vartheta(y, z)$. Note that the y-dependence is too weak to be visible.

is used in Eq. 3.3 to close the Maxwell curl equations according to

$$\mathbf{D} = \hat{\varepsilon}\,\mathbf{E} \qquad \text{and} \qquad \mathbf{H} = \frac{1}{\mu_0}\mathbf{B} \tag{3.25}$$

and thus propagate beams through the LC material with spatially-dependent anisotropy. The director profile is plotted as a vector field in Fig. 3.5. The effect of the pretilt boundary conditions on the z-dependence is evident, but the modulation in y is too small to be visible.

3.5 Finite-Difference Time-Domain Calculations

3.5.1 General Considerations and Reduction to 2D

The purpose of this investigation was to explore beam coupling effects occuring in the LC layer. The cell windows are treated as an isotropic medium with refractive index n_{Ph}. The photorefractive effects occurring therein are already well-understood and were not modeled.

The space-charge field of Eq. 3.15 determines the director profile in terms of material parameters, beam incidence angle δ, and the complex modulation parameters $\mathcal{M}_{\mathrm{F}}$ and $\mathcal{M}_{\mathrm{B}}$. The strength (magnitude m) and position (phase ϕ) of the front and back window interference patterns created by the beams as they interact with the LC layer are unknowns to be interrogated from FDTD data and used to update the material in a self-consistent manner. The resulting steady-state relative permittivity tensor $\hat{\varepsilon}(y,z)$ diffracts the continuous-wave beams which may be "measured" and used to determine the beam coupling gain G.

The three-dimensional FDTD code described in Section 1.2 was reduced to two dimensions for propagation in the yz-plane. Essentially, this is done by reducing the rank of all arrays whose dimensions correspond to real space by one, and imposing on the discretized Maxwell curl equations that all electromagnetic field components F_i have no x-dependence: $\frac{\partial F_i}{\partial x} \to 0$. This is not to say that the fields $\mathbf{F}$ have no x-components. Circularly polarized light, for example, may still be simulated using this code, but only for propagation directions in the yz-plane, and for spatial beam profiles with infinite extent in the x-direction. The choice of incident beam polarizations (in the yz-plane) and the form of $\hat{\varepsilon}(y,z)$ in Eq. 3.3, however, prevent fields from developing any x-components in these numerical beam coupling experiments.

3.5.2 Total-Field Scattered-Field Incident Wave Formulation

The incident beams were "fed into" the computational domain (CD) via a Fortran implementation of the Total-Field Scattered-Field (TFSF) incident wave formulation [4]. This technique facilitates the simulation of optical interactions at arbitrary angle of incidence and relies on the fact that the Maxwell equations are linear on the interface between two distinct subdomains of the CD. In the inner domain the total electric and magnetic fields are stored in memory as usual. This is where the material interactions of interest to the user take place. In a domain surrounding the total-field region, the fields stored in memory and updated at

each time step are the "scattered fields":

$$\mathbf{E}_{\text{scat}}(\mathbf{r}) = \mathbf{E}_{\text{total}}(\mathbf{r}) - \mathbf{E}_{\text{inc}}(\mathbf{r}, t) \quad \text{and} \quad \mathbf{H}_{\text{scat}}(\mathbf{r}) = \mathbf{H}_{\text{total}}(\mathbf{r}) - \mathbf{H}_{\text{inc}}(\mathbf{r}, t) \tag{3.26}$$

which are computationally available because incident fields are designed by the user and hence known for all $\mathbf{r}$ and t. The operators in the Maxwell equations distribute across these relations, leaving the algorithm unchanged except on the interface between the partitions. The Yee grid cells traditionally must be "sewn together" on this interface such that the incident excitation propagates across the inner region and is subtracted from the interface opposite where it was inserted. However, since the total (as opposed to scattered) fields transmitted/diffracted from the LC layer were of interest here, this operation was imposed only on the TFSF "slit" positioned in the front photorefractive window, as shown in Fig. 3.6. The fact that there is a disconnect in the field updating scheme, and an associated ambiguity as to which fields (total or scattered) are stored near the disconnect, creates no numerical artifacts as long as the incident fields near that disconnect are sufficiently small. The ambiguity is irrelevant as seen from Eqs. 3.26 with $\mathbf{E}_{\text{inc}}(\mathbf{r}, t) = \mathbf{H}_{\text{inc}}(\mathbf{r}, t) = 0$ for all t.

A fourth-order super Gaussian beam shape,

$$E_{\text{inc}}(\rho) \propto \sqrt{I_0}\, \exp\left(-\ln(2)\, 2^{n-1} \left(\frac{\rho}{w}\right)^n\right) \tag{3.27}$$

with $n = 4$ was used for a number of reasons. Here, $I_0 = 1$ (arb. units) is the intensity at the center of the beam shape, $w = 28$ μm is the FWHM of the beam intensity, and ρ is the spatial coordinate transverse to the propagation direction for the beam. Most importantly, the extraction of the phases ϕ_{F} and ϕ_{B} of the complex modulation parameters[3] requires an interference pattern that varies in a sinusoidal manner as in Eq. 3.9. The interference pattern formed by ordinary Gaussian beams is gated spatially, which would complicate the

[3]This will be described in Section 3.5.3

implementation of the LC material model. Additionally, higher-order super Gaussians decay faster at the edges of the beam profile, which conveniently prevents overlap of the incident beams and the TFSF slit edge that would cause the artifacts just mentioned. On the other hand, higher-order shapes aperture the beam more severely, causing it to diffract. This is minimized by choosing $n = 4$ in Eq. 3.27, while retaining a sufficiently non-gated interference pattern for the sake of implementing the LC material model.

Simulations begin with zero E and H fields throughout the CD. The beams are introduced on the TFSF slit and ramped up according to a Gaussian time profile with $1/e$ field width of 5 fs. As the continuous-wave (cw) beams were continuously excited at the TFSF slit, and because no material updating occurs until after all aspects of the beams associated with this time profile have propagated through to the PML and been absorbed, the choice was fairly arbitrary.

It should be noted that the incidence angles (δ) that were used as input parameters are significantly smaller than the beam angles as constructed on an optical table in the experiments. This is because the numerical simulations are confined to the photorefractive windows. Beams crossed at larger angles in air refract by Snell's law upon entry into the higher-index front photorefractive window. This was accounted for by the experimenters in their determination of values for grating spacings (Λ) within the photorefractive in terms of beam angles on the optical table. Incidence angles (δ) *within* the photorefractive window will be quoted in what follows.

3.5.3 Implementation of the LC Permittivity

The space-charge field develops in a cw-illuminated photorefractive according to a characteristic time that depends not only on material parameters like charge carrier mobility and recombination time, the structure of donor and acceptor levels, and its effective dielectric constant, but also on experimental parameters like grating spacing $\Lambda = 2\pi/q$, temperature

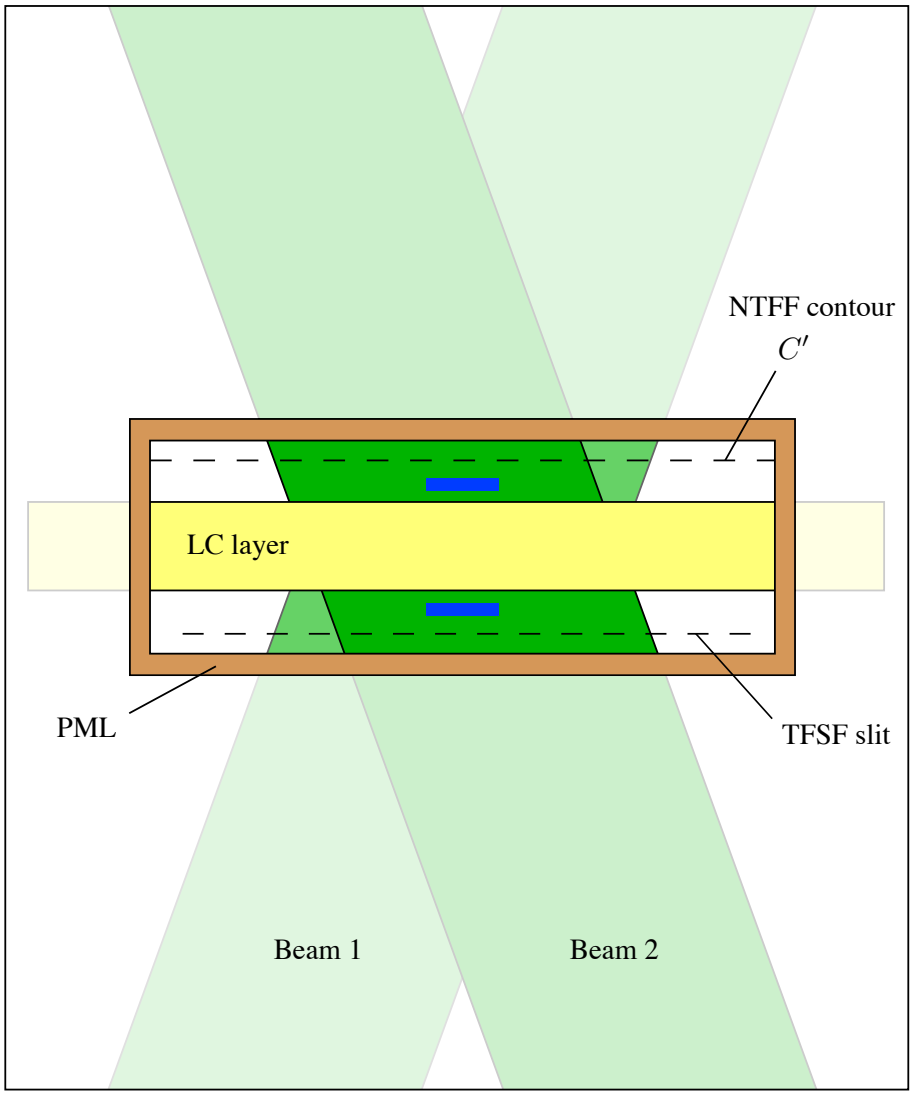

Figure 3.6: Geometry of FDTD simulations of two-beam coupling described in this chapter. The blue boxes represent the "zones" where modulation parameters are determined from electric field data.

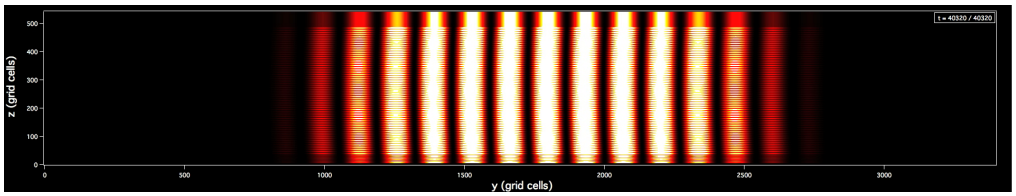

Figure 3.7: Example intensity data corresponding to beams crossed in the geometry shown in Fig. 3.6 for the case $\Lambda = 3$ μm.

T, and the intensities of the overlapped beams [37]. A fundamental lower limit to the photorefractive response time based on the time required to transport a charge carrier by $\Lambda/2$ was proposed by Glass *et al.* [38], though it is not viewed as being extremely useful because of the large discrepancy between the values it produces (from 10^{-12} s to 10^{-9} s depending on charge carrier mobility) and the much larger values observed experimentally. Regardless, the hybrid cell response is bottlenecked by the response time of the nematic LC director reorientations, which is on the order of 10^{-3} s or longer [39]. This is much longer than the $\sim 10^{-13}$ time scale on which the interference patterns are modified by the optical fields propagating through a LC layer with $L = 10$ μm.

The LC material model described in Section 3.4 is kinematic in nature. Transient and/or dispersive effects requiring a causal approach to the relationship between $\mathbf{D}$ and $\mathbf{E}$ are ignored from the outset. The LC material model was imposed in the context of the FDTD updating scheme by inserting into the middle of the leap-frog time-updating scheme the computation of $\mathbf{E}$ from $\mathbf{D}$ according to

$$\mathbf{E} = \hat{\varepsilon}^{-1}\,\mathbf{D} \tag{3.28}$$

so that the response is treated mathematically as being instantaneous. The continuous-wave beams propagate initially through the LC layer with zero space-charge field ($\mathcal{M}_{\mathrm{F}} = \mathcal{M}_{\mathrm{B}} = 0$), and the LC material is later "turned on" by computing $\mathcal{M}_{\mathrm{F}}$ and $\mathcal{M}_{\mathrm{B}}$ continuously at each time step and inserting them into the model, thus driving the optical fields to their steady state.

The magnitudes m_{F} and m_{B} of the complex modulation parameters are computed using Eq. 3.12 in each photorefractive window. The regions where these are calculated will be referred to as the "front zone" and "back zone", and are indicated by the blue boxes in Fig. 3.6. The modulated intensity distributions $I_{\mathrm{F}}(y)$ and $I_{\mathrm{B}}(y)$ at time t are computed in each window as follows:

For each zone,

- In a rank 3 array with dimensions corresponding to y, z, and time t, store the value of $|\mathbf{E}|^2 = E_x^2 + E_y^2 + E_z^2$, for the past $\mathtt{n}_{T/2}$ time steps, where $\mathtt{n}_{T/2}$ is the number of time steps corresponding precisely[4] to half the period T of one optical cycle[5].

- Sum the array over it's t dimension and divide by $\mathtt{n}_{T/2}$. This gives the time average of $|\mathbf{E}|^2$, which is $\propto I$.

- Sum the array over it's z dimension and divide by the number of grid cells that defines the zone size in the z-direction. This results in the intensity spatially averaged over z.

The resulting one-dimensional data set describes the interference pattern as depicted by the red curve in Fig. 3.3, from which the magnitude and phase of the modulation parameters

$$\mathcal{M}_{\mathrm{F}} = m_{\mathrm{F}}\, e^{i\phi_{\mathrm{F}}} \qquad \text{and} \qquad \mathcal{M}_{\mathrm{B}} = m_{\mathrm{B}}\, e^{i\phi_{\mathrm{B}}} \tag{3.29}$$

are determined. The magnitudes m_{F} and m_{B} are computed from $I_{\mathrm{F}}(y)$ and $I_{\mathrm{B}}(y)$ using Eq. 3.12. The phase ϕ_{F} is extracted from $I_{\mathrm{F}}(y)$ as follows:

- Construct $I'_{\mathrm{F}}(y) = \left[2\, I_{\mathrm{F}}(y) - \left(I_{\mathrm{F}}^{(\max)} + I_{\mathrm{F}}^{(\min)}\right)\right] / \left(I_{\mathrm{F}}^{(\max)} - I_{\mathrm{F}}^{(\min)}\right)$, which vertically shifts and scales $I_{\mathrm{F}}(y)$ to a sinusoid oscillating between 1 and -1.

- Perform a fit of $I'_{\mathrm{F}}(y)$ to `cos(q*y(j)+phi)` using the Levenberg-Marquardt method [40], where `phi` is the variable to be optimized and `y(j)` is a Δy-spaced abscissa constructed to have a common origin[6] with `yLC(j)`, the $\frac{\Delta y}{2}$-spaced y-coordinates of the director profile $\vartheta(y, z)$. The optimized `phi` is returned as ϕ_{F}.

[4]The size of the time step Δt is chosen such that $\frac{T/2}{\Delta t}$ is an integer.

[5]The quantity $|\mathbf{E}|^2$ ocsillates at twice the frequency as $\mathbf{E}$. Therefore, the extent of the array dimension corresponding to time may be halved.

[6]A less restrictive requirement on the coordinate sets is that their origins are separated by an integer multiple of $2\pi/q$.

This procedure is repeated in the back zone to extract ϕ_{B}, and $\hat{\varepsilon}(y,z)$ is subsequently updated according to $\vartheta(y,z)$ given in Appendix D.

Example optical properties of the LC layer are depicted in Fig. 3.8 for the case of $\Lambda = 3$ μm, $L = 10$ μm, and incident beams with equal intensity. The refractive indices plotted here are the extraordinary refractive index variation in the y-direction for particular z-positions indicated by red, blue, and green coloring. This quantity is given by [34]

$$n_{\mathrm{e}}(\beta) = \frac{1}{\sqrt{\frac{\cos^2\beta}{\varepsilon_\perp} + \frac{\sin^2\beta}{\varepsilon_\parallel}}} \tag{3.30}$$

where β is the angle between the director $\mathbf{n}$ and the nominal propagation vector $\mathbf{k}$. The angle β takes on a separate set of values for the two beams, which are assumed to be approximately constant during propagation through the first ~ 2 μm of the LC layer in order to create the refractive index plots. Because all propagation vectors, incident wave polarizations, and LC directors lie in the same plane, all waves are extraordinary and therefore experience the directionally-dependent extraordinary index $n_{\mathrm{e}}(\beta)$, as opposed to the ordinary index n_{o}.

The grating spacings investigated ranged from 0.5 μm to 5.5 μm, which corresponds to incidence angles between 1.155° and 12.81°. The beam crossing angle depicted in Fig. 3.6 is exaggerated. In addition, the beams used in simulations had a spot size defined by a intensity FWHM of 28 μm, which caused them to diverge[7] more so than would realistic but computationally expensive beam spot sizes of a few millimeters. Direct determination of the gain G from interrogated electric field values was frustrated by these features to the point that the problem was rendered impractical in terms of required CPU time, and unmanageable in terms of memory requirements. Noting that after the beams have exited the LC layer their propagation through the upper medium is trivial, a Near-To-Far-Field

[7]While use of the term "diffract" to describe how a beam with finite extent develops spatially according to the Maxwell curl equations would be technically more accurate, it is misplaced in the context of this discussion of beam coupling by diffraction.

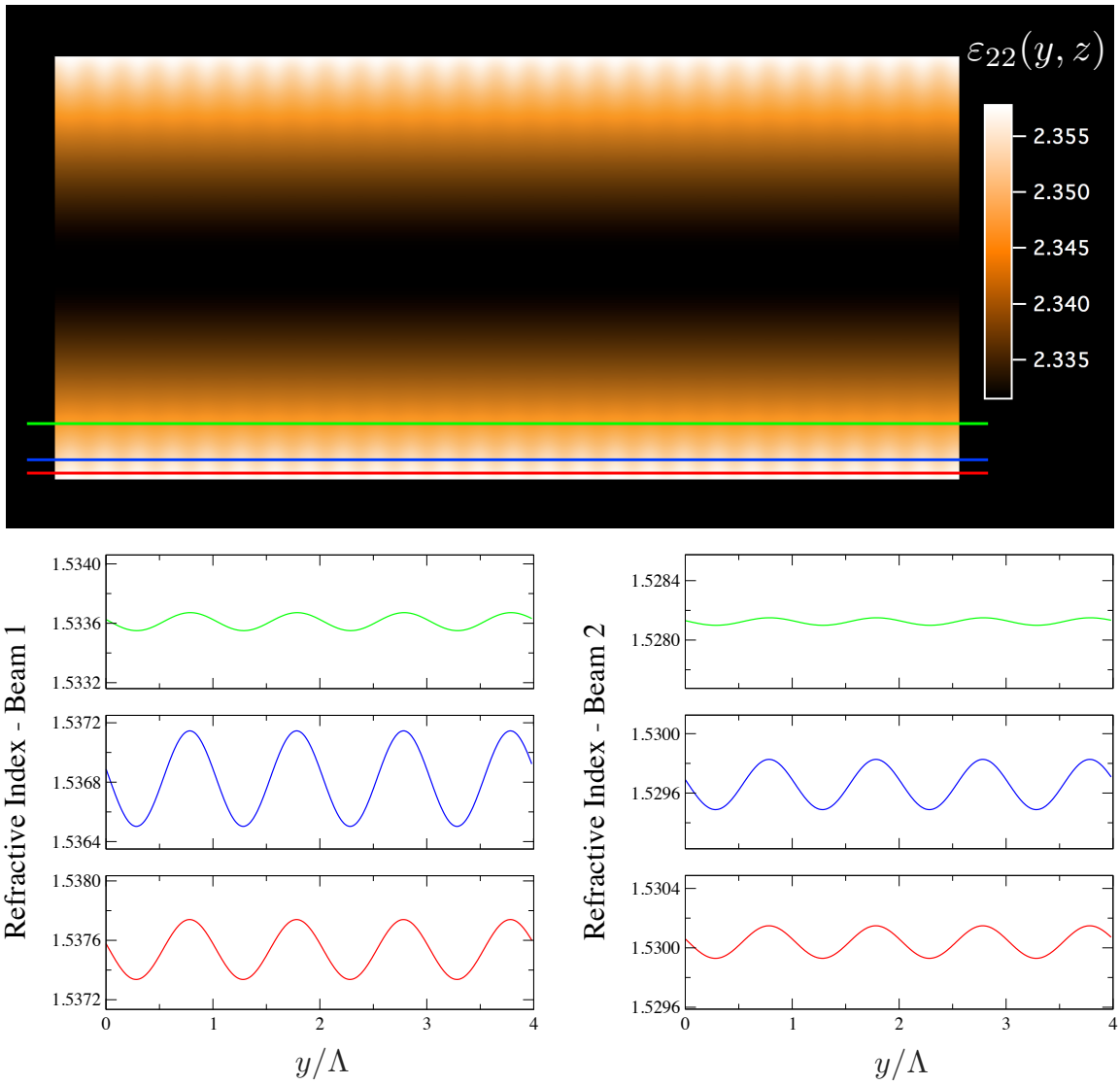

Figure 3.8: Optical properties of the LC layer for the case $\Lambda = 3$ μm, $L = 10$ μm, and incident beams with equal intensity: The 22-component of $\hat{\varepsilon}$ as a function of space, and refractive index variation in y for the z-positions indicated by red, blue, and green labels. Note that the aspect ratio in the upper plot is not 1:1.

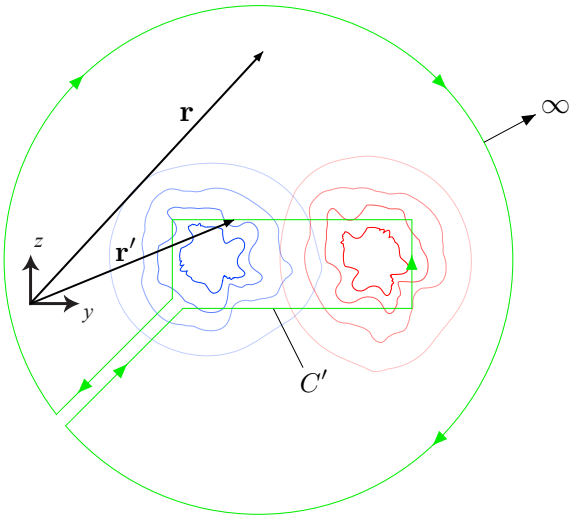

Figure 3.9: Geometry of Green's Theorem as applied to the NTFF Transformation. Arbitrary fields radiating from two sources are represented in red and blue.

(NTFF) transformation was implemented to construct the far-field intensity distribution produced by the beams diffracted by the LC layer.

3.6 Near-to-Far-Field Transformation

It is well known that Green's Theorem may be applied to a wave function and the Green function corresponding to radiation from a point source at $\mathbf{r}'$ to an observation point $\mathbf{r}$, and thus construct the wave function at $\mathbf{r}$ in terms of sources at various $\mathbf{r}'$ in the limit $\mathbf{k}\,|\mathbf{r}-\mathbf{r}'| \to \infty$ [2, 41]. See Fig. 3.9. In the context of computational electromagnetics, the boundary conditions imposed on the fields may be used to construct hypothetical electric and magnetic current distributions on the contour C', with $\mathbf{E}$ and $\mathbf{H}$ set equal to zero inside C'. This is called the *surface equivalence theorem* and states that any radiating field distribution within C' may be replaced by equivalent electric and magnetic current distributions on C',

and that these current distributions may be used as sources to compute the fields in the radiation zone. For the problem at hand, this procedure is performed in order to spatially separate beams crossed at a small angle.

Time-domain expressions for the far fields in terms of the sources can be derived from Lorentz gauge scalar and vector potentials, each satisfying the inhomogeneous wave equation [42]. Cast in terms of the hypothetical sources $\mathbf{J}$ and $\mathbf{M}$ of the surface equivalence theorem, the electric field is [43]

$$\begin{aligned}\mathbf{E}_{\mathrm{rad}}(\mathbf{r},t) \;=\; & \frac{\mu_0}{4\pi}\int_{S'} \frac{\left(\left[\dot{\mathbf{J}}(\mathbf{r}',t)\right]_\tau \times \mathbf{R}\right)\times\mathbf{R}}{R^3}\, dS' \\ & -\frac{1}{4\pi c}\int_{S'} \frac{\left[\dot{\mathbf{M}}(\mathbf{r}',t)\right]_\tau \times \mathbf{R}}{R^2}\, dS'\end{aligned} \tag{3.31}$$

with the equivalent sources

$$\mathbf{J}(\mathbf{r}',t) = \hat{\mathbf{n}}(\mathbf{r}')\times\mathbf{H}(\mathbf{r}',t) \qquad \text{and} \qquad \mathbf{M}(\mathbf{r}',t) = -\hat{\mathbf{n}}(\mathbf{r}')\times\mathbf{E}(\mathbf{r}',t). \tag{3.32}$$

Here, $[\ ]_\tau$ represents evaluation at the retarded time $\tau = t - R/c$, the dot $(\dot{\cdot})$ represents differentiation with respect to time, $\hat{\mathbf{n}}(\mathbf{r}')$ is the unit vector normal to S', and $\mathbf{R} = \mathbf{r} - \mathbf{r}'$.

In reference [43], a two-dimensional problem is formulated in terms of a three-dimensional one with infinite extent in the spatial dimension on which fields have no dependence. The surface S' extends from $x' = -\infty$ to $+\infty$. This was done to express the integral over x' in terms of a time integral because the time-retarded contributions at various x' correspond to various times in the history of a transient waveform. For the case of the two-beam coupling system investigated here, the integration may be performed on the open contour C' as illustrated in Fig. 3.6. The use of such an open contour is discussed in [4] and has proved beneficial in the context of computing the radiation fields scattered in a particular

direction [44]. In addition, the Fresnel-Kirchhoff diffraction formula is derived by carrying out a mathematical procedure that is nearly identical to the NTFF transformation. There, the contour is chosen as the semi-infinite hemisphere into which light is transmitted by an aperture, and the outer (curved) integration surface is placed at a distance greater than the diffracting light has had time to travel, and thus contributes nothing to the integral [6]. The use of the open NTFF contour as shown in Fig. 3.6 is equally justified.

Eqs. 3.31 and 3.32 were reduced to the following expressions for the components of the electric field at $\mathbf{r}$, which is chosen to lie in the yz-plane ($x = 0$):

$$E_x(\mathbf{r},t) = \frac{1}{2\pi}\int_0^\infty dx' \int_{C'} dC' \left(\frac{n_{\mathrm{Ph}}}{c}\frac{(z-z')}{R^2}\,\dot{E}_x^\tau + \mu_0 \frac{(y-y')^2 + (z-z')^2}{R^3}\,\dot{H}_y^\tau \right) \tag{3.33}$$

$$E_y(\mathbf{r},t) = \frac{1}{2\pi}\int_0^\infty dx' \int_{C'} dC' \left(\frac{n_{\mathrm{Ph}}}{c}\frac{(z-z')}{R^2}\,\dot{E}_y^\tau - \mu_0 \frac{(x')^2 + (z-z')^2}{R^3}\,\dot{H}_x^\tau \right) \tag{3.34}$$

$$E_z(\mathbf{r},t) = \frac{1}{2\pi}\int_0^\infty dx' \int_{C'} dC' \left(\frac{-n_{\mathrm{Ph}}}{c}\frac{(y-y')}{R^2}\,\dot{E}_y^\tau + \mu_0 \frac{(y-y')(z-z')}{R^3}\,\dot{H}_x^\tau \right) \tag{3.35}$$

where n_{Ph} is the refractive index assumed in the back photorefractive window and the notation $\dot{F}_i^\tau$ represents the i^{th}-component of the time derivative of the field $\mathbf{F}$ at position $\mathbf{r}'$, evaluated at the retarded time τ. The spatial uniformity of the $\mathbf{E}$ and $\mathbf{H}$ fields in the x-direction and using $\hat{\mathbf{n}}(\mathbf{r}') = \hat{\mathbf{z}}$ for all points on C' provides this level of simplification. These integrals are computed numerically using a trapezoid rule, and choosing $\mathbf{r}$ to correspond to a far-field screen such that $\frac{2\pi n_{\mathrm{Ph}}}{\lambda} \times z = 10^6$.

The quantities $\dot{F}_i^\tau$ are time-dependent complex functions with phase corresponding to $\mathbf{k}\cdot\mathbf{r}'$. Insertion of FDTD data into Eqs. 3.33 – 3.35 requires the determination of the relative phases between the F_i on the NTFF contour. Additionally, evaluation at various retarded times τ requires some sort of interpolation of the FDTD data, which are stored

at discrete time steps. Both of these features were addressed using a modified version of the Levenberg-Marquardt fitting routine used to extract the phases of the modulation parameters and invoking linear superposition: The Huygens-Fresnel principle states that, for a (linear) material structure with arbitrarily complicated spatial dependence illuminated by light at frequency ω, the electromagnetic disturbance at some position $\mathbf{r}'$ is the coherent sum of spherical wavelets with amplitudes A_i and the same frequency:

$$F(\mathbf{r}', t) = \sum_{i=1}^{\infty} A_i \, e^{i(\mathbf{k}_i \cdot \mathbf{r}' - \omega t)} + \text{c.c.} \tag{3.36}$$

The $e^{-i\omega t}$ time-dependence factors out of the sum, yielding a wave oscillating at frequency ω for all $\mathbf{r}'$. It follows that the components of $\mathbf{E}$ and $\mathbf{H}$ at all $\mathbf{r}'$ have frequency ω, so that fits to the function $A(\mathbf{r}') \cos(\omega t + \phi(\mathbf{r}'))$ provide the *continuous* function $\dot{F}_i = i\omega A(\mathbf{r}') \exp(i(\omega t + \phi(\mathbf{r}')))$ to be inserted into Eqs. 3.33 – 3.35 and evaluated at $\tau = t - R/c$ during the integration. The full history (and future) of the steady state is determined by data stored for a single cycle at each point $\mathbf{r}'$ on C'.

The NTFF transformation described above was tested by calculating the far-field diffraction pattern of $\lambda = 532$ nm light transmitted by a single slit [45] of width $d = 4.84$ μm using near-field data on C'. The resulting normalized far-field intensity distribution is plotted in Fig. 3.10 along with the analytical result $I = \sin\alpha/\alpha$ with $\alpha = \frac{1}{2}kd\sin\theta$, where $k = \frac{2\pi}{\lambda}$ and θ is the angle between $\hat{\mathbf{z}}$ and a vector from the center of the slit to the observation point (y, z).

As all information about the system with no x-dependence is contained in a single $x =$ constant plane, the consideration of the x-dependence of the integrands in Eqs. 3.33 – 3.35 evaluated at retarded times, which *do* actually depend on x', seems to be an unnecessary adherence to a NTFF transformation derived in 3D for a 2D system. However, a proof that the contributions from individual terms integrated over C' for $x' = x_1$ are pro-

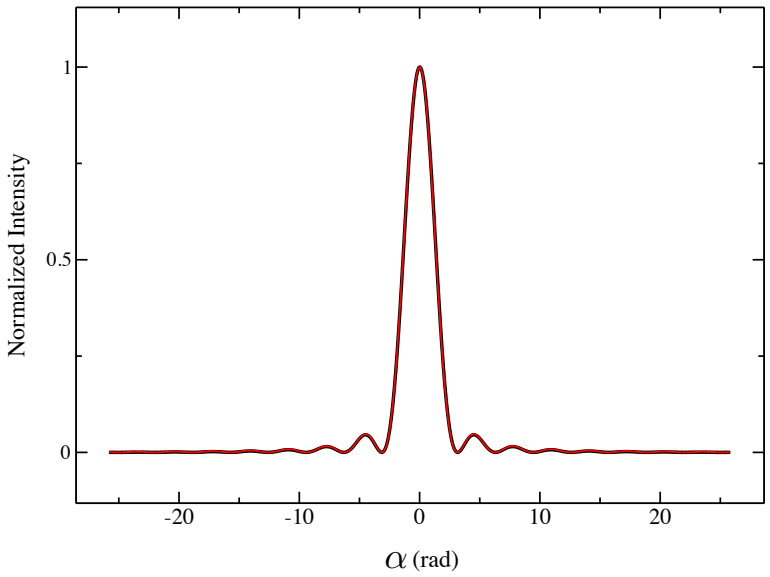

Figure 3.10: Single-slit diffraction pattern calculated analytically (red curve) and by the FDTD code (black curve) incorporating the near-to-far-field transformation described in the text.

portional to the corresponding contribution from $x' = x_2$ was not found. The integrands in Eqs. 3.33 – 3.35 decrease to 0 as $x' \to \infty$. The NTFF transformation was coded with the idea of evaluating the x' integrals from 0 to some $x_{\max}$ such that contributions from $x' > x_{\max}$ are negligible. However, not only the intensities, but also the components of $\mathbf{E}$ in the far field were found to be completely independent of the choice of $x_{\max}$ apart from a scale factor. This, and the fact that E_x is necessarily zero in this problem, means that the far-field intensity distribution may be computed from $\mathbf{E}(\mathbf{r}) \cdot \mathbf{E}^*(\mathbf{r})$ using the components of Eqs. 3.34 and 3.35 and any particular numerical value[8] for t, where the integrals over x' are dropped.

[8] $t = 0$ was used in all far-field calculations.

3.7 Results and Discussion

The results described in this section were computed using beams with wavelength $\lambda = 532$ nm and a Yee grid cell size $\Delta y = \Delta z = \lambda/(N_\lambda\, n_{\max})$, choosing $N_\lambda = 10$ as the grid sampling resolution and $n_{\max} = n_{\mathrm{Ph}} = 2.4$, since the ordinary and extraordinary indices associated with the LC were both < 2. This assignment results in waves and material features spatially resolved by grid points separated by $\lambda/10$ at most. The size of the time step was chosen as $\Delta t = \Delta z/(2\,c)$, corresponding to a Courant number $S = c\Delta t/\Delta z = 0.5 < \frac{1}{\sqrt{2}}$. A 60-cell (1.33 μm thickness) PML absorbing boundary was used. Additional simulation parameters associated with LC and photorefractive materials are listed in Appendix C.

The gain G vs. Λ attributed to the LC layer for incident beams with wavelength $\lambda_0 = 532$ nm was determined as follows:
For each grating spacing $\Lambda = \lambda_0/(2\, n_{\mathrm{Ph}} \sin\delta)$,

- Propagate the incident beams into the LC director configuration corresponding to $\mathbf{E}_{\mathrm{sc}} = 0$ and wait for the steady state to be reached in which the beams are reflected, deflected, etc. by the pretilted director and then absorbed by the PML.

- Compute the far field diffraction pattern using the NTFF transformation. The $\mathbf{E}_{\mathrm{sc}} = 0$ director has no y-dependence and thus cannot result in coupling between beams and corresponds to a power measurement of Beam 1 with Beam 2 blocked as in experiments [46]. Define the spatially-integrated far-field intensity pattern of Beam 1 for this case as I_0.

- Turn on the LC material updating as described in Section 3.5.3 and allow the system to converge to the steady state. The parameters m_{F}, ϕ_{F}, m_{B}, and ϕ_{B} at each time step were written to files and plotted to verify convergence.

- Compute the $\mathbf{E}_{\mathrm{sc}} \neq 0$ far-field diffraction pattern using the NTFF. Define the spatially-

integrated far-field intensity pattern of Beam 1 for this case as I.

- Compute the gain $G = I/I_0$.

The liquid crystal TL205 was used in the experiments simulated during this numerical investigation. The photorefractive windows were constructed from cerium-doped strontium barium niobate (SBN:Ce). Results from experiments conducted by Evans and Cook and the result calculated by analytical methods by Reshetnyak are taken from [35] and shown in Fig. 3.11 (a). The poor agreement between these results, as reflected by the plotting of the natural logarithm of g as opposed to g itself, motivated the investigation by the FDTD method. Neither the overall magnitude, nor the decrease in gain coefficient for $\Lambda > 2$ μm, are captured in the analytical solution.

Results from a large number of simulations are shown in Fig. 3.11 (b). The gain coefficient obtained from FDTD simulations using the most reliable estimates available for the LC and photorefractive material parameters (solid curve) fails to explain the overall magnitude of the gain coefficient measured in experiments. The magnitude of the effect is the same whether calculated by FDTD or analytically. The small difference, which is revealed by a careful comparison of the solid curves in Fig. 3.11, is attributable to the 1° difference in pretilt angles used.

There are clear oscillations in the FDTD result that are absent from the analytical result. These oscillations bear a noticeable resemblance to the oscillations in the experimental data and may be explained as follows: The beams were seen to bend continuously as they propagate through the LC layer in a manner dominated by the $\theta_0(z)$ part of $\vartheta(y, z)$, which arises from the pretilts. This may be qualitatively seen in the intensity data shown in Fig. 3.7. The actual coupling would depend on constructive and destructive interference between diffraction orders at the back face of the LC layer. However, steady-state modulation parameters resulting from a completed run may be manually assigned to a subsequent auxiliary run

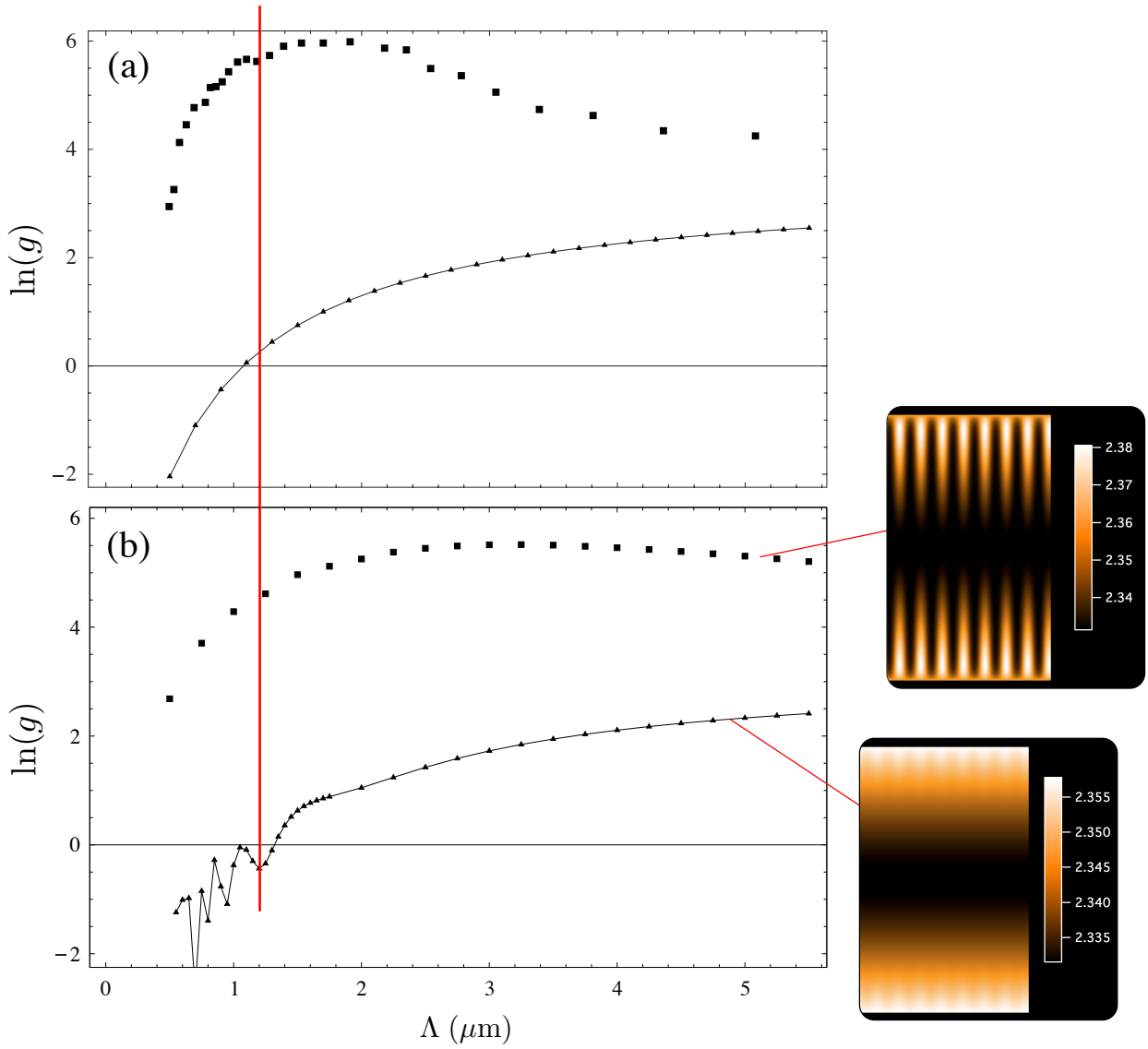

Figure 3.11: FDTD numerical results computed as part of this dissertation and the corresponding experimental measurements and theoretical calculations. (a) Experimental results (black boxes) and the theoretical calculation (solid curve) using $\theta_{\mathrm{F}} = 12°$, $\theta_{\mathrm{B}} = -12°$ as reported in [35]. (b) FDTD result obtained using accepted LC and photorefractive material parameters and $\theta_{\mathrm{F}} = 11°$, $\theta_{\mathrm{B}} = -11°$ (solid curve) and the FDTD result obtained using LC material parameters adjusted as described on pg. 68 (black boxes), each labeled by the corresponding plot of $\varepsilon_{22}(y, z)$.

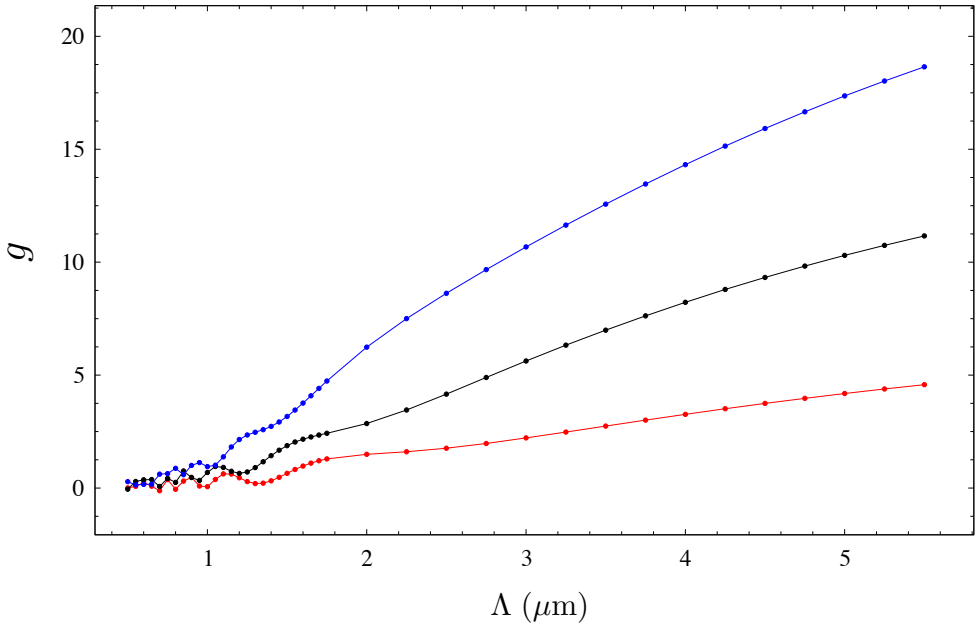

Figure 3.12: Exponential gain coefficient derived from FDTD simulations performed using $\theta_{\mathrm{F}} = -\theta_{\mathrm{B}} = 5°$ (red), 11° (black), and 20° (blue).

using a single beam, simply to get an idea of what effect the steady-state LC layer has on it. The beam paths are arced to various extents depending on incidence angle, and therefore, grating spacing. Though subject to the intricate details of the anisotropic permittivity that varies continuously in space, it may be argued on geometrical grounds that there is a variation in the phase relationship between the transmitted portion of one beam and the Bragg reflection of the other beam that is monotonic in δ according to the optical path difference associated with the variation of these arc lengths.

Shown in Fig. 3.12 are plots of g vs. Λ calculated by the FDTD method for various pretilts. In addition to the overall magnitude of the beam coupling effect, the size of the pretilt determines the initial refraction angle of the beams upon their entry into the LC layer, and thus shifts the influence of the effect on beams simulated using the same incidence

angle δ. The oscillations are less rapid as grating spacing increases. This is largely a matter of the relationship between grating spacing and incidence angle: $\Lambda = \lambda_0 / (2\, n_{\mathrm{Ph}} \sin\delta) \approx \lambda_0 / (2\, n_{\mathrm{Ph}} \delta)$, which results in an abscissa that distorts the oscillation that is fairly constant as a function of δ.

Also plotted in Fig. 3.11 (b) is a gain curve (black boxes) derived from simulations that used LC material parameters that were adjusted to produce the relative permittivity distribution labeling that curve. Each of the flexoelectric coefficients e_{11} and e_{33} were increased by a factor of 12.5, and the LC bend elastic constant K_{33} was decreased by two orders of magnitude. The flexoelectric effect has been strengthened relative to the LC bend restoring force. These values are justified neither by experimental measurements nor by theoretical considerations. The fact that this curve indicates an overall gain magnitude similar to that of the experimental data as well as a negative slope at large grating spacings indicates that additional physical effects need to be incorporated into the model [35] in order to produce a larger LC permittivity modulation in the y-direction.

3.8 Conclusions

The FDTD calculations presented in this chapter have validated the analytical calculation of beam coupling in the LC layer, with director given by Eqs. 3.19 – 3.23, in terms of overall gain magnitude. The analytical calculation assumes constant propagation directions for the beams as they pass through the LC layer. There are additional approximations [35] associated with solving a vector wave equation that are made between deriving the director expression $\vartheta(y, z)$ and obtaining an expression for the exponential gain coefficient $g(\Lambda)$. It is clear from a comparison between numerical and analytical calculations that the failure of the analytical approach to capture the measured magnitude of the gain in the LC hybrid device was not due to these approximations. Those approximations do, however, fail to capture the

oscillatory behavior revealed by the FDTD numerical investigation conducted as part of this dissertation.

Chapter 4

Finite-Difference Time-Domain Studies of Ag Nanostructures

4.1 Introduction

The turn of the century has seen tremendous increases in the ability to manipulate matter on the scale of nanometers. Nanotechnology is expected to result in advances in a broad range of technologies, including optics. Electromagnetic wave engineering entails either the manipulation of the electric and magnetic properties of a device arising from its morphology or the selection of materials with appropriate properties. The first strategy refers to the manipulation of the arrangement of materials, an example being the antenna used to transmit and receive radio transmissions. A radio-frequency antenna may be tuned and optimized by adjusting its morphology on the length scale of meters because the wavelength of the radiation is on the length scale of meters. The second strategy is a matter of the device's constituent materials. An example is the Pockels cell, which is used to rotate the polarization of a wave during its transmission according to an applied voltage. Considering wavelengths in the visible and infrared regimes, the absorption, dispersive, birefringent, and

nonlinear characteristics of a material are determined by polarizabilities at the molecular level as well as characteristics of crystal and quantum mechanical energy level structure. "Metamaterials" may be designed with the first idea in mind, but to operate at infrared and visible wavelengths [47]. Control over the optical properties of these metamaterials at these wavelengths is a function of our level of control over material morphology at nanoscopic length scales. Such control is increasingly afforded by nanotechnology.

This chapter presents numerical investigations of the optical properties of Ag nanostructures fabricated by Oblique Angle Deposition (OAD). This method entails the deposition of atoms onto a substrate whose orientation relative to the atomic source is precisely controlled. The Ag vapor is created by boiling off atoms from a solid Ag sample using an electron beam in an evacuated chamber maintained at $\sim 5 \times 10^{-7}$ torr [48]. Within this chamber, the substrate may be held at a particular orientation relative to the source so that rods with morphological features on the scale of nanometers result from competition between surface diffusion and a shadowing effect [49]. The growth of these "nanorods" is controlled by the substrate orientation and depends on its type of material, surface quality, and temperature.

Calculations were performed using the commercial FDTD software package XFdtd (Remcom). Commercial software was used primarily because of the need to reliably and efficiently construct the intricate geometrical objects corresponding to nanostructure morphology. This is accomplished conveniently within XFdtd by its 3D drawing capabilities. Once drawn, various "parts" may be assigned a material by the user, which imposes in the region of space occupied by the part a particular set of constitutive relations assumed by the FDTD field-updating scheme. A screen shot of the XFdtd user interface is shown in Fig. 4.1.

The Drude model for the conductivity of metals was employed by way of the frequency-domain permittivity

$$\varepsilon(\omega) = 1 - \frac{\omega_{\mathrm{p}}^2}{\omega\,(i\,\gamma + \omega)} \tag{4.1}$$

where ω_p is the plasma frequency and γ is the scattering frequency. This permittivity may be derived by taking the $\omega_0 \to 0$ limit in a damped, driven oscillator model for the response of $\mathbf{D}$ to $\mathbf{E}$, where ω_0 is the resonance frequency [2]. Qualitatively, charges in this model are being driven in a fluid with viscosity associated with γ. At frequencies below the plasma frequency, a propagating field incident upon the metal's surface does not appreciably penetrate it and is almost entirely reflected. However, the size and shape of a material structure may be comparable to the wavelength in such way as to excite surface plasmons that conform spatially to the material morphology[1]. The transient response, as described by Eq. 4.1, may result in plasmon resonances, not fundamental to the underlying material model, but rather, associated with the geometry of the material surface.

Fabrication techniques have been advanced recently, resulting in nanostructures with a range of morphologies. Among the methods used is "dynamic shadowing" growth, which entails rotating the substrate either continuously or intermittently during Ag deposition [51]. One of the resulting structures is a "bent nanorod array"; the substrate is rotated intermittently to result in helical structures constructed from straight rod segments. Such a structure may be drawn within XFdtd, and periodic boundary conditions surrounding the structure may be imposed such that a perfectly-ordered, infinite 2D array of idealistic helices may be modeled using a computational domain corresponding to a single "nanohelix". This simulation scheme is depicted in the screen shot in Fig. 4.1. The helix shown is constructed from four segments each with length 200 nm, diameter 50 nm, and rotated out of a z=constant plane by 20°. The translational symmetry in the x- and y-directions is given by the respective sizes of the computational domain, each of which are 400 nm here.

[1]The work function of Ag [50] is sufficiently large to exclude photoelectric ejection for all wavelengths considered in this work.

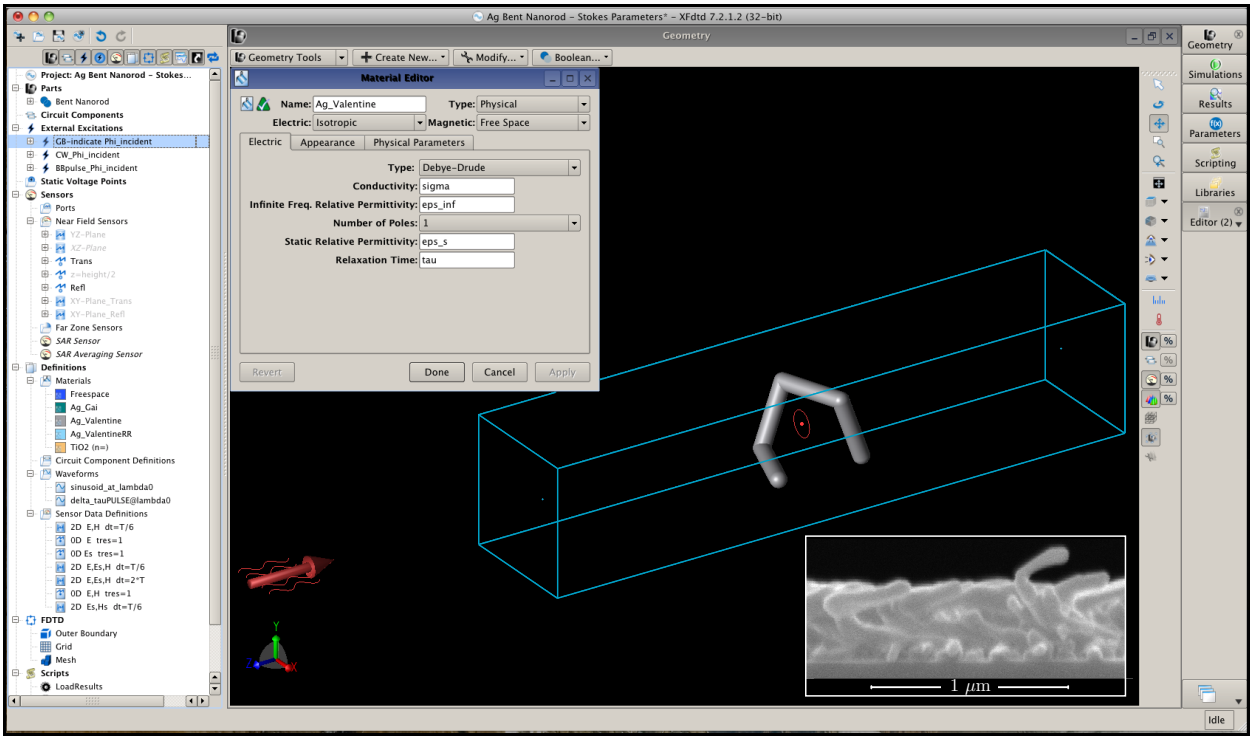

Figure 4.1: XFdtd graphical user interface. The computational domain is indicated by the blue box. The incident wave (indicated by the red guide) is polarized in the x-direction and propagates in the negative z-direction. The inset is a side-view SEM image of an actual nanohelix array.

Structures with helical pitch on this length scale are expected to exhibit optically-relevant chirality. This was explored using the FDTD method by calculating the Stokes parameters

$$S_0 = A_x^2 + A_y^2 \tag{4.2}$$

$$S_1 = A_x^2 - A_y^2 \tag{4.3}$$

$$S_2 = 2\,A_x\,A_y \cos\left(\phi_y - \phi_x\right) \tag{4.4}$$

$$S_3 = 2\,A_x\,A_y \sin\left(\phi_y - \phi_x\right) \tag{4.5}$$

for reflected and transmitted waves using incident wavelengths ranging from 500 nm to 900 nm. Here, A_x and ϕ_x are the amplitude and phase of the x-component of the electric field propagating in the negative z-direction, and likewise for the y-component. The meanings of these quantities are [52]:

- $S_0 \leftrightarrow$ Total irradiance
- $S_1 \leftrightarrow$ Irradiance transmitted by a linear polarizer oriented to pass waves polarized in the x-direction, less the irradiance transmitted by a linear polarizer oriented to pass waves polarized in the y-direction
- $S_2 \leftrightarrow$ Irradiance transmitted by a linear polarizer oriented to pass waves polarized in the direction of $\hat{\mathbf{x}} + \hat{\mathbf{y}}$, less the irradiance transmitted by a linear polarizer oriented to pass waves polarized in the direction of $-\hat{\mathbf{x}} + \hat{\mathbf{y}}$
- $S_3 \leftrightarrow$ Irradiance transmitted by a device that is transparent only to right-hand circularly polarized waves, less the irradiance transmitted by a device that is transparent only to left-hand circularly polarized waves

The laboratory measurement of Stokes parameters is treated in [53].

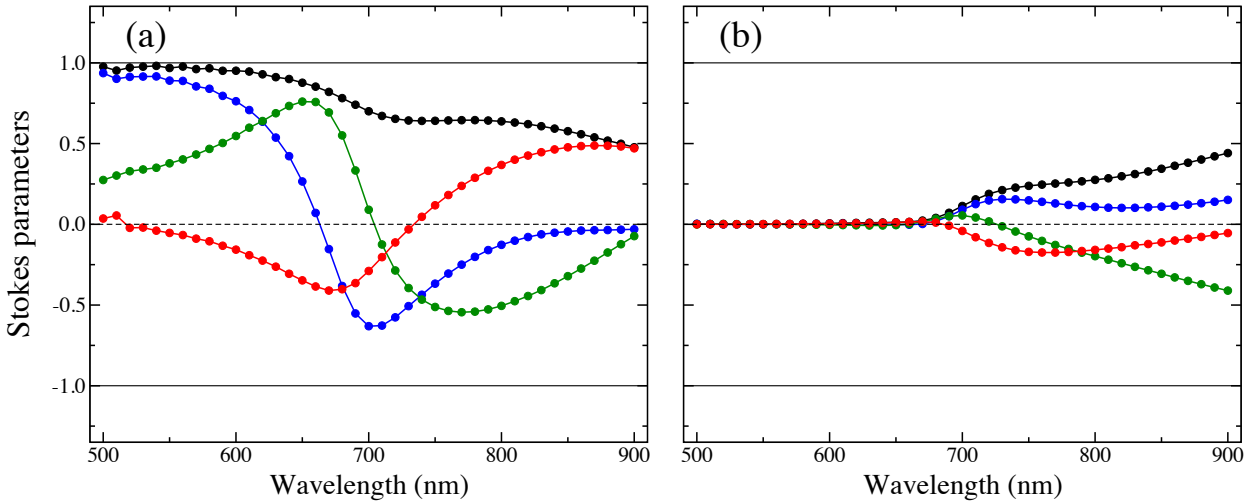

Figure 4.2: (a) Stokes parameters S_0 (black), S_1 (blue), S_2 (green), S_3 (red) of the light *transmitted* by the nanohelix array. (b) Stokes parameters (same color scheme) of the light *reflected* by the nanohelix array.

The Stokes parameters were calculated by propagating linear-polarized continuous waves (in separate calculations) toward the array until the transverse components of the transmitted and reflected fields, recorded at a single point in space far from the array, converged to steady-state sinusoids. The late-time components were then post-processed by fitting them to extract the amplitudes and phases for each case. The Stokes parameters are normalized by virtue of the fact that normalized incident fields were used.

The results are shown in Fig. 4.2. A variety of polarization states can be identified in the transmitted fields. Near $\lambda = 500$ nm the array is highly transmissive and rotates the polarization slightly off the x-axis. As $\lambda = 700$ nm is approached, the behavior shifts wildly as reflectance increases. At $\lambda = 900$ nm, the array transmittance is ~ 0.5, and the transmitted wave is essentially right-hand circularly polarized.

The remainder of this chapter describes FDTD studies of systems for which there were experimental data. The actual nanohelix arrays fabricated by Zhao *et al.* are much more

dense, and reflect much more light than they transmit. The measurement of Stokes parameters corresponding to Fig. 4.2 is planned for the future, and follow-up FDTD simulations using densely packed helices[2] may be performed for comparison.

4.2 FDTD Investigation of the Increased Electromagnetic Contribution to Surface-enhanced Raman Scattering in Ag Nanorod Arrays Deposited at Low Temperature

4.2.1 Introduction

Raman scattering refers to the inelastic scattering between photons and optical phonons that results in photons with shifted frequency. If sufficiently strong, this effect may be detected by irradiating molecules with a laser and resolving the scattered light with a spectrometer. Surface-enhanced Raman scattering (SERS) refers to the vast increase in the magnitude of this effect when the scattering species are positioned on a metallic surface. It is expected that single molecule detection by SERS, which has been reported [54] for the special case of a particular dye molecule, can be made feasible by modest improvements to these metallic SERS substrates. The high surface-to-volume ratios and distinguishing electromagnetic properties of metallic nanostructures make them a promising candidate.

The SERS enhancement factor of a substrate is known to depend on surface morphology. The SERS characteristics of Ag nanorod arrays have been studied in detail [48, 55]. These nanostructures are deposited at room temperature. At lower temperatures, the Ag atoms are less likely to be thermally dislodged from their initial landing site, leading to rougher

[2]The use of periodic boundary conditions does not limit in any way the density of helices that may be simulated.

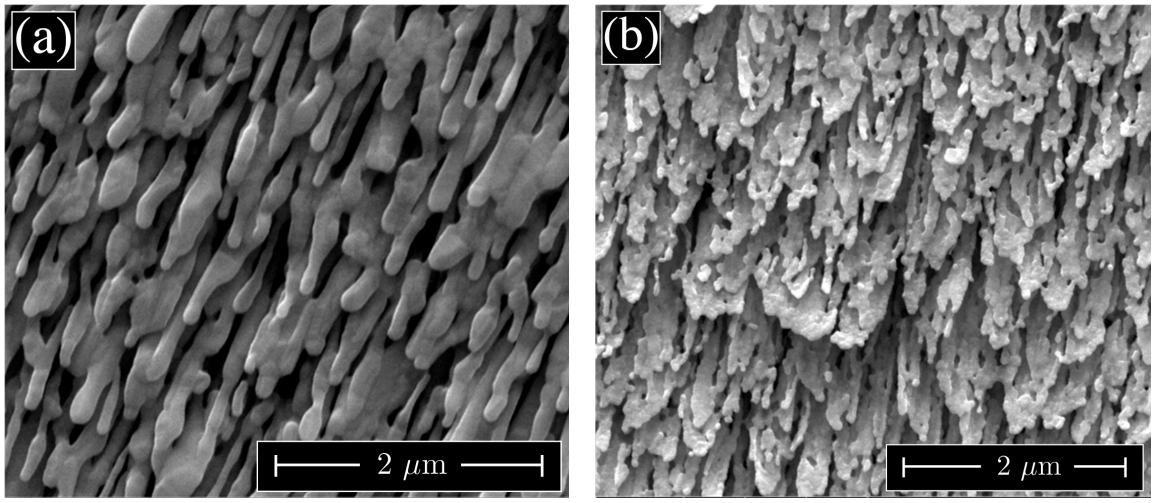

Figure 4.3: SEM top-view images of Ag nanorod SERS substrates grown at (a) room temperature, and (b) 140 K substrate temperature.

morphology. As a result, nanostructures deposited onto substrates held at low temperature have a rough, porous morphology. It was concluded by previous studies that the porous features of Ag films (no nanorods) deposited at low temperatures are active Raman scattering sites [56]. Scanning electron microscope (SEM) images of Ag nanorod arrays deposited onto substrates by Oblique Angle Deposition held at room temperature and a temperature of 140 K are shown in Figs. 4.3 (a) and (b), respectively. The FDTD calculations presented in this section are specific to these structures, and meant to capture the increased SERS sensitivity measured by Singh *et al.* using a laser operating at a wavelength of 785 nm [57].

A widely accepted contribution to the measured enhancement of Raman scattering from molecules deposited on metallic nanostructures is the concentration of the electric field in particular localized regions of the surface morphology [58]. These regions are referred to as "hot spots", and their significance is attributed to a scaling of the electromagnetic contribution to the detected Raman-shifted radiation as the fourth power of the ratio of the local

electric field near the metallic surfaces to the incident electric field [59]:

$$I^{\mathrm{SERS}} \sim \left| \frac{\mathbf{E}_{\mathrm{local}}(\omega)}{\mathbf{E}_0(\omega)} \right|^4 \tag{4.6}$$

Here, it is assumed that the nanostructure has approximately the same optical properties at frequencies ω and $\omega \pm \omega_{\mathrm{vib}}$, and supposed that the nanostructure 1) scatters the incident electric field onto hot spots and 2) scatters the Raman-shifted radiation towards the detection system by the same proportion [60–62]. Note that this local field enhancement makes no reference to any particular scattering molecule. In order to investigate the effect the manifestly distinct surface morphology of nanorod arrays deposited at low temperature has on local field enhancement, SERS enhancement factors of the form in Eq. 4.6 were computed from data generated by XFdtd.

4.2.2 FDTD Calculations

The FDTD method integrates Maxwell's curl equations directly in the time domain. As such, the electric field vector may be interrogated at arbitrary points in space and time and then post-processed to quantify the local field enhancement for various Ag nanorod morphologies. The incident laser beam used in the experiments modeled was unpolarized. FDTD source excitations are vectors which have definite polarization states. In reality, an unpolarized electromagnetic wave is characterized by orthogonal electric field vector components with random, rapidly-varying phase difference and equal magnitude [63] regardless of the choice of coordinate basis. Rather than simulate this statistical behavior directly, separate calculations were performed using mutually orthogonal ("s" and "p"), linearly polarized incident waves and the results were summed incoherently. The square of the electric field magnitude for the

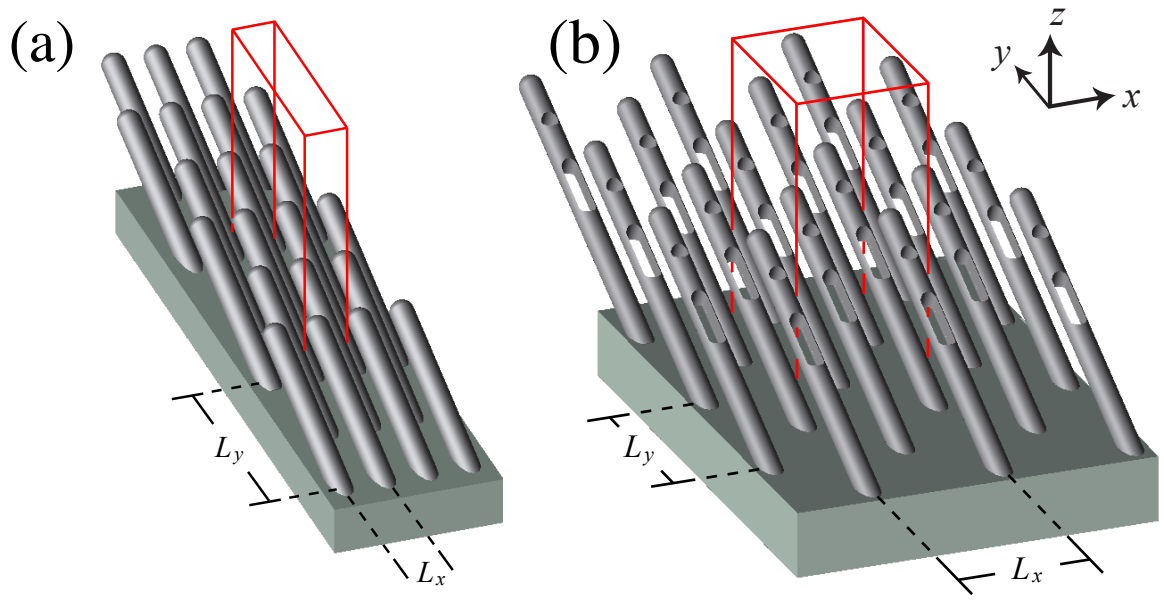

Figure 4.4: Two of the morphologies used in FDTD simulations. The red box indicates the unit cell of each staggered array and defines the computational domain. See text for geometrical parameters. (a) Ag nanorods deposited at room temperature. (b) Porous Ag nanorods deposited at 140 K.

case of an unpolarized beam was taken as the arithmetic mean of the individual results:

$$|\mathbf{E}_{\text{unpol}}(\mathbf{r},t)|^2 = \frac{1}{2}\left(|\mathbf{E}_s(\mathbf{r},t)|^2 + |\mathbf{E}_p(\mathbf{r},t)|^2\right) \tag{4.7}$$

The Ag nanorods deposited at room temperature shown in Fig. 4.3 (a) have, on average, length 900 nm, diameter 100 nm, and make an angle of 71° with the substrate normal. These parameters were used to construct an idealization of the morphology grown at room temperature, which is staggered to correspond to a less-ordered array and is shown in Fig. 4.4 (a). The separations between positions of the nanorods for the room temperature case are $L_x = 177$ nm and $L_y = 862$ nm. More precisely, there are two 2D arrays with lattice vectors $L_x\,\hat{\mathbf{x}}$ and $L_y\,\hat{\mathbf{y}}$, one of which is displaced by $(L_x\,\hat{\mathbf{x}} + L_y\,\hat{\mathbf{y}})/2$ to form a

two-dimensional rhombic Bravais lattice in the xy-plane. The porous nanorods deposited at low temperature and shown in Fig. 4.4 (b) have length 1 μm, diameter 70 nm, and make an angle of 63° with the substrate normal. For this case, $L_x = 400$ nm and $L_y = 500$ nm. The porosity of the nanorods deposited at low temperature was modeled by inserting pores with diameter 50 nm as well as 50 nm $\times$ 200 nm slits into the nanorods as shown in Fig. 4.4 (b). The idealized morphologies used in FDTD calculations meant to correspond to nanorods deposited on substrates held at 140 K will be indicated by "LT", and those deposited at room temperature will be indicated by "RT" in this chapter. In each case, the nanorods are positioned on a 200 nm Ag base layer. The RT and LT morphologies were discretized on a spatial grid with cell edge lengths $\sim$ 4 nm for preliminary calculations and then $\sim$ 2 nm. The $\sim$ 5 and 2.5 attosecond time steps that result from these choices according to the Courant stability condition [4] ensure numerical stability for the plane wave excitation with 785 nm wavelength. The nanorod arrays are infinite in the plane of the substrate by virtue of periodic boundary conditions imposed on the sides of the of the $L_x \times L_y$ unit cell of each staggered geometry. The incident wave travels in the negative z-direction, and the perfectly matched layer absorbing boundary condition is employed on the faces bounding the z-directed dimension of the computational domain, which is indicated by the red boxes in Fig. 4.4.

Drude behavior in the Ag base layer is implemented according Eq. 4.1 with plasma frequency $\omega_{\mathrm{p}} = 1.37\times10^{16}$ rad/s and scattering frequency $\gamma = 2.73\times10^{13}$ rad/s corresponding to bulk Ag [64]. The scattering frequency in the Ag nanorods is increased by a factor of 3 to account for increased surface scattering [65]. Note that Eq. 4.7 is not the average of two intensities. The time-averaged Poynting vector depends on $\mathbf{E}$ and $\mathbf{H}$, which are not in proportion near surfaces by virtue of the complicated spatial dependence of electromagnetic wave fields interacting with a metallic structure with morphological features on this length

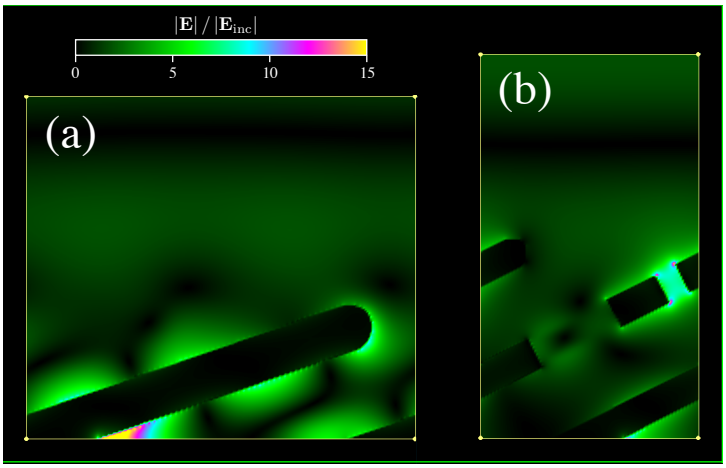

Figure 4.5: Example local field enhancement from simulations using the morphologies shown in Fig. 4.4. The incident wave is polarized in the y-direction and propagates in the negative z-direction. The ratio of local to incident electric field magnitude is shown in a yz-plane that bisects one of the rods in each case. Note that values greater than 15 saturate the color scale.

scale. However, the Raman molecules are regarded as dipole scatterers that respond to $\mathbf{E}$. The squared magnitude of $\mathbf{E}$ is therefore the correct quantity to consider.

Previous numerical investigations of the local field enhancement have indicated the magnitudes of the local electric field in various regions of similar Ag nanostructures [55], to which the results for the RT nanorods, depicted in Fig 4.5 (a), are comparable. For example, a steady-state hot spot may be identified near the small-angle point of contact between tilted nanorods and base layer for the case of a y-polarized incident wave. The electric field magnitude reaches a strong maximum ($\sim 60\times$ the incident amplitude) precisely at the intersection between nanorod and base layer. The field reaches this magnitude only within a very small volume of the idealized surface morphology. The morphology shown in Fig. 4.4 (b) exhibits hot spots in and around the pores and slits, with a decreased enhancement at the base owing in part to the smaller tilt angle in the LT case. Again, maxima ($\sim 20\times$ the incident

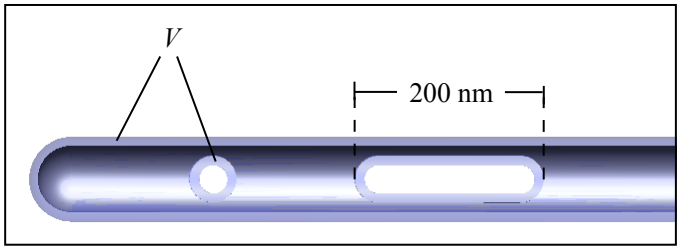

Figure 4.6: The integration volume V considered to contain Raman probe molecules is the 10 nm shell coating the porous nanorods and the base layer (not shown).

amplitude) are found in small volumes located near the sharp material features. Note that the data in Fig 4.5 correspond to calculations that used a grid cell edge length $\sim$ 4 nm, and to a steady-state time value for which the local electric fields are maximally enhanced. It is clear that the two case morphologies have local field enhancements with very different and complicated spatial dependence. Spatial averaging is therefore necessary to compare in a more meaningful way the electromagnetic contribution to the detected Raman signal computed for the two morphologies [58, 66].

It is reasonable to assume that the Raman molecules may be located between the surfaces of the nanorods + base layer and an imaginary surface that coats the metallic morphology, creating a shell with thickness 10 nm. This construction is depicted in Fig. 4.6 for the case of the morphology shown in Fig. 4.4 (b). The electric field magnitude as a function of position is stored for all grid points located within this shell, and for each of 50 time values separated by $T/50$ that occur at the end of the simulation after convergence has been reached. Here, T is the duration of one cycle of the 785 nm wavelength incident wave. These data were gathered from calculations using orthogonally polarized incident waves and used to compute $|\mathbf{E}_{\text{unpol}}(\mathbf{r}, t)|^2$ according to Eq. 4.7 for the cases of RT and LT idealized morphologies. The

Raman scattering enhancement is calculated as

$$I^{\mathrm{SERS}}(\mathbf{r}) = \left[\frac{\langle |\mathbf{E}_{\mathrm{unpol}}(\mathbf{r},t)|^2 \rangle}{\langle |\mathbf{E}_0(\mathbf{r},t)|^2 \rangle} \right]^2 \tag{4.8}$$

where $\mathbf{E}_0$ refers to the incident wave and the angle brackets $\langle\ \rangle$ denote a time average over one period of the steady-state oscillation. The quantity $\langle |\mathbf{E}_0(\mathbf{r},t)|^2 \rangle = \frac{1}{2}$ for the case of a sinusoidal incident electric field with amplitude 1.0 (arbitrary units). The Raman scattering enhancement is then averaged over the volume V of the 10 nm shells coating the nanorods for each case:

$$I^{\mathrm{SERS}}_{\mathrm{avg}} = \frac{1}{V} \int_V I^{\mathrm{SERS}}(\mathbf{r})\, dx\, dy\, dz \ \rightarrow\ \frac{1}{N} \sum_{i=1}^{N} I^{\mathrm{SERS}}(i) \tag{4.9}$$

where i indexes the N discrete field points in the shell volume within which all FDTD grid cells have the same volume. The ratio of these quantities calculated for two distinct surface morphologies provides a quantitative measure of their relative electromagnetic SERS enhancement.

The SERS signal measured for nanorod arrays deposited at low temperature is increased relative to that of the room temperature case by a factor ~ 2 [57]. The structure shown in Fig. 4.4 (b) was constructed to investigate the effect of pores added to the morphology, and uses the somewhat different geometrical parameters estimated using SEM images. Note that these calculations used a grid cell edge length ~ 2 nm. It is known that rough and/or porous features on metallic nanostructures lead to enhanced local fields [67]. While the field was seen to be enhanced in and around the pores of the structure shown in Fig. 4.4 (b), this enhancement does not result in $I^{\mathrm{SERS}}_{\mathrm{avg}}(\mathrm{LT})$ that is superior to $I^{\mathrm{SERS}}_{\mathrm{avg}}(\mathrm{RT})$. In fact, the ratio formed by these quantities is 0.091. Clearly, the attributes of the surface morphology shown in Fig. 4.4 (b) do not result in a local field enhancement superior to that of the RT nanorods.

To investigate the origin of the difference between the two results, two variations on the parameters defining the structure in Fig. 4.4 (b) were explored: Firstly, it was supposed that an inter-rod field coupling may be stronger and that the regions where the field is enhanced lie more within the integration volume V for the thicker, more densely packed RT morphology of Fig. 4.4 (a). The parameters L_x and L_y were therefore reduced to 320 nm and 400 nm respectively for the LT case, resulting in $I_{\text{avg}}^{\text{SERS}}(\text{LT})/I_{\text{avg}}^{\text{SERS}}(\text{RT}) = 0.041$. In other words, the performance of the LT morphology was further degraded. Secondly, the dependence of $I_{\text{avg}}^{\text{SERS}}(\text{LT})$ on the angle the nanorods make with the base layer was briefly explored. The components of the incident wave electric field vector are in the plane of the base layer and therefore more prone to excite currents along the RT nanorods which are closer to in-plane alignment. Setting the LT rod angle equal to the RT rod angle resulted in $I_{\text{avg}}^{\text{SERS}}(\text{LT})/I_{\text{avg}}^{\text{SERS}}(\text{RT}) = 0.634$, which is a large increase. These observations led to the hypothesis that the connective Ag matter evident in the SEM image in Fig. 4.3 (b) and situated predominantly at the rod tips, plays an important role. To test this, the morphology of Fig. 4.4 (b) was modified by adding connective rod segments which lie in a plane normal to the incident propagation vector and connect nanorods that are staggered with respect to each other. This morphology is shown in Fig. 4.7. This construction resulted in $I_{\text{avg}}^{\text{SERS}}(\text{LT})/I_{\text{avg}}^{\text{SERS}}(\text{RT}) = 2.030$, which is in agreement with the experimental result. These results are summarized in Table 4.1. Pairs of spatial slices with $x =$ constant of the steady-state electric field magnitude in the integration volume and at a time value corresponding to maximally enhanced local fields[3] are shown in Figs. 4.8 and 4.9 for the case of a y-polarized incident wave. Note that the incident electric field amplitude is normalized to unity. It is clear that this addition has produced a morphology whose electromagnetic SERS enhancement is superior to that of the idealized RT morphology.

[3]Note that the local peaks of $|\mathbf{E}|$ do not all occur at precisely the same time.

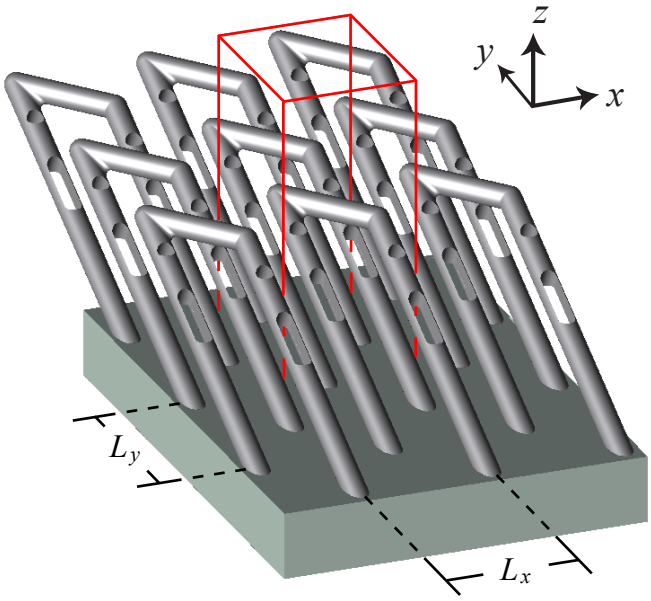

Figure 4.7: The LT morphology with connective rod segments added.

It is important to note that the contribution to Eq. 4.9 from the shell added to account for the added connective rod segment, which is not indicated in Figs. 4.8 and 4.9, was noticeably smaller than the contribution from the other portions of the integration volume V. This is meaningful in that it reveals the fact that the local field is *not* enhanced *on* the added segment, but rather, that the added segment is on average more strongly driven by each orthogonal component of the unpolarized incident field. It is also relevant that the fields in this case took significantly longer to converge to steady-state, as revealed by time-dependent data visualization within XFdtd. The added rod tips provide conductive pathways between nanorods such that surface plasmon modes associated with the geometry of the connected morphology may develop over time and lead to superior local field enhancement near the pores and other sharp features.

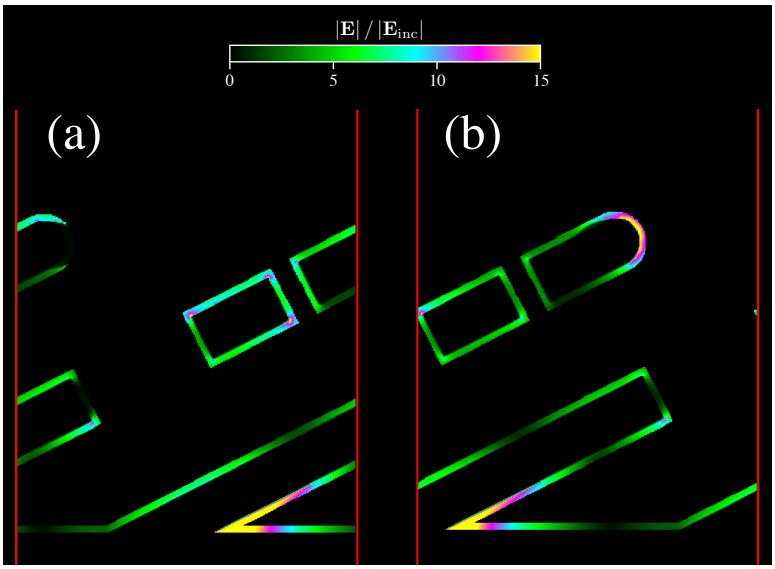

Figure 4.8: Local field enhancement in a slice of the integration volume *that bisects the rods* for the case of the connected morphology shown in Fig. 4.7. The incident wave is y-polarized in this case. Because this system lacks the symmetry possessed by the morphology of Fig. 4.4 (b), the local field enhancement is not the same in all rods. (a) corresponds to the rods used to indicate L_x in Fig. 4.7. (b) corresponds to the rods used to indicate L_y in Fig. 4.7. Note that values greater than 15 saturate the color scale.

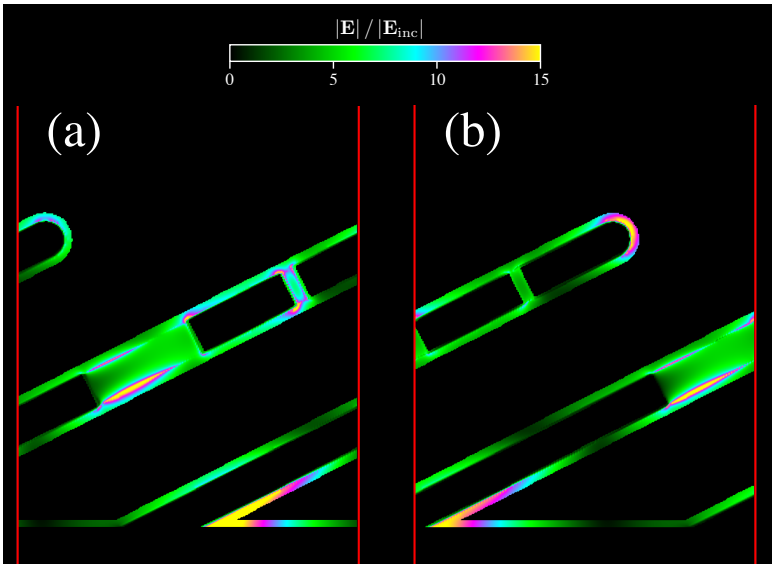

Figure 4.9: Local field enhancement data from the same simulation as Fig. 4.8, but in a slice of the integration volume *near the edge of the pores*.

Table 4.1: Summary of ratios of spatially-averaged electromagnetic contribution to the detected Raman signal for various modifications of the LT morphology.

Morphology	Rod Angle (°)	L_x (nm)	L_y (nm)	$I_{\text{avg}}^{\text{SERS}}(\text{LT})/I_{\text{avg}}^{\text{SERS}}(\text{RT})$
RT - Fig. 4.4 (a)	71	177	862	–
LT - Fig. 4.4 (b)	63	400	500	0.091
LT - Fig. 4.4 (b)	63	320	400	0.041
LT - Fig. 4.4 (b)	71	400	500	0.634
LT - Fig. 4.7	63	400	500	2.030

4.2.3 Conclusion

This FDTD investigation took as its basis the validity of Eq. 4.6, which is rarely considered to capture the entire effect of SERS in metallic nanostructures [60, 67]. The remarkable agreement between the reported experimental result (~ 2) and the numerical result (2.030) was unexpected. On the other hand, the experimental result is a relative increase in SERS sensitivity measured using nanorods deposited in the same lab, using the same probe molecule, and differing only in the deposition temperature (which results in modified morphology). Contributions depending on, for example, the changes to the quantum chemistry of the probe molecule arising from the presence of the Ag surface therefore play far less a role, if any role at all.

The pores have been identified as electric field hot spots in FDTD calculations, which in addition have demonstrated the significance of the blade-like rod tips to the electromagnetic contribution to SERS enhancement. This interpretation is not considered to be expressed by "$2 \approx 2.030$", but rather, by the sequence of simulations leading up to that result, which is discussed in the preceding text and summarized in Table 4.1.

4.3 FDTD Modeling of the Transmission of Terahertz Radiation by Ag Nanorod Arrays

4.3.1 Introduction

Terahertz (THz) optics is an active field of research. The weak response of dielectric materials to radiation in this 10^{11}–10^{13} Hz regime is distinct from that in other frequency bands and facilitates non-destructive inspection, imaging through otherwise opaque materials, and chemometrics of pharmaceuticals [68]. However, it is these very aspects of the material responses to THz that make its control difficult. The range of possible applications is being expanded by the increasing ability to manipulate the radiation in ways analogous to techniques established in the visible and IR regimes. Examples include bandpass filters [69], wave plates [70], and linear polarizers. The latter would require a material with polarization-dependent transmittance in the THz regime.

This section describes FDTD modeling of transmission of THz pulses by Ag nanorod arrays fabricated by OAD on silicon wafers. Experimental data for the range 0.2–4 THz show a transmission coefficient with magnitudes $\sim 0.5\%$ for polarization parallel to and $\sim 5\%$ for polarization normal to the deposition direction[4].

4.3.2 FDTD Simulations

Transmission spectra at normal incidence were calculated using XFdtd. Recall that the time-domain nature of FDTD allows the broadband optical response of a material structure composed of linear media to be obtained from a single calculation that uses a pulsed excitation source. The sample transmission coefficient as a function of frequency may be calculated over the bandwidth of the incident pulse by Fourier transforming the incident

[4]Data are plotted in Figs. 4.13 and 4.14

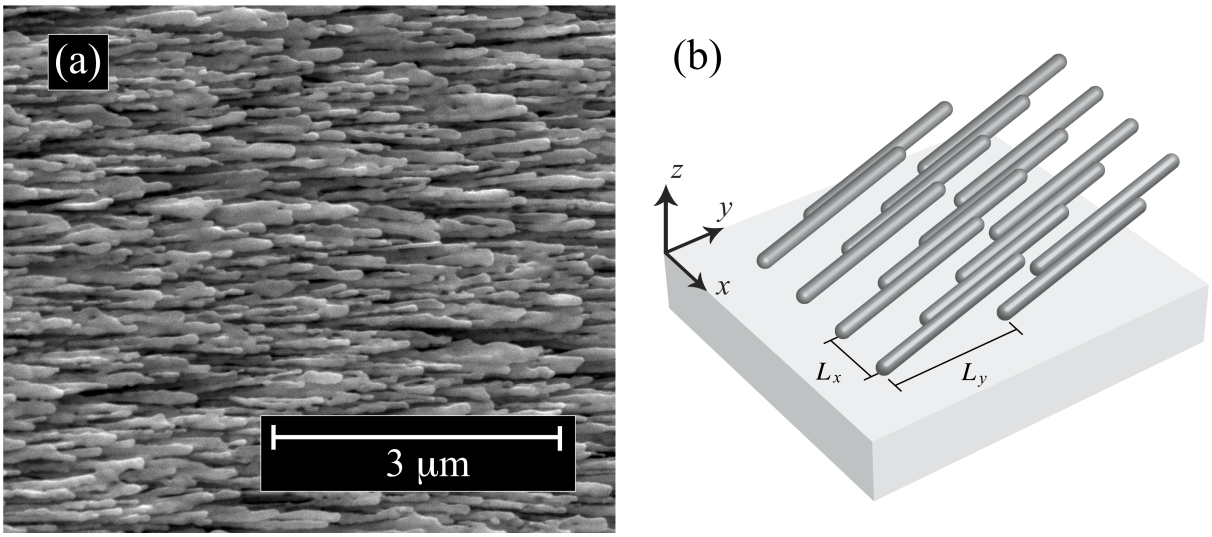

Figure 4.10: (a) SEM image of the Ag nanorods deposited on a silicon wafer. (b) The staggered base morphology derived from the SEM image, and coordinate frame used in FDTD simulations. The nanorods have diameter 100 nm, length 1 μm, and make a 72° angle with the substrate normal. $L_x = 250$ nm, $L_y = 893$ nm.

and transmitted pulses, and taking the ratio. The simulations described here use $\sim$ 1 ps pulses centered at $\sim$ 1 THz.

Shown in Fig. 4.10 (a) is an SEM image of the nanostructure. On average, the nanorods have length 1 μm, diameter 100 nm, and make an angle of 72° with the substrate normal. These parameters were used to construct what will be referred to as the "base morphology", which is staggered in the same way as the idealized nanorods of the previous section (4.2) with $L_x = 250$ nm and $L_y = 893$ nm. See Fig. 4.10 (b).

The computational expense in terms of the run time and memory footprint of an FDTD calculation is largely determined by the choice of the size of the grid on which space is discretized. A grid cell size of 8 nm was chosen with a mind to resolving the base morphology while maintaining reasonable computation size, and noting that the resulting "staircased" meshing of the rod geometry results in features that are at most $10^{-4} \times \lambda_{\min}$, where $\lambda_{\min}$ refers

to the shortest wavelength contributing to the excitation spectrum. Note that not all mesh points are separated by precisely 8 nm, as the software's meshing engine may modify this slightly in order to better represent the various curved surfaces. The ~ 10 attosecond time step that results from this choice according to the Courant stability condition [4] ensures numerical stability for all frequencies and materials considered. The size of the computational domain required was reduced by imposing periodic boundary conditions at the edges of the 893 nm $\times$ 250 nm unit cell of the staggered geometry, which corresponds to a physical system that is infinite in the plane of the substrate. The incident pulse travels in the negative z-direction, and the perfectly matched layer absorbing boundary condition is employed in the z-direction as before.

Special care was taken to ensure that the absorbing boundary was located sufficiently far from the structure such that the transmitted electric field interrogated near it corresponded to the propagating transmitted field. The center wavelength of the incident pulse (~ 300 μm) is much longer than the thickness of the rod array < 1 μm. The *propagating* electromagnetic field must be interrogated in order to compute the relevant transmittance. Simulations using a computational domain extended in the z-direction by 640 μm were performed initially. A spatial grid gradually tapered to 8 μm was employed to speed up the simulations with such a large computational domain. However, this led to non-physical dispersive effects caused by the varying spatial grid, which caused the pulse to be erroneously stretched in time during propagation through vacuum. The issue was settled by using a constant grid size of 8 nm and computational domain length of ~ 152 μm in a computationally expensive run, and observing that the electric field interrogated relatively close to the nanorods propagated unchanged after reaching a distance ~ 1 μm from the nanorods. A convention was gradually adopted of observing the near-field z-component of $\mathbf{E}$ as a function of position in the xz- and yz-planes in order to verify that the field interrogated as the transmitted field propagating in the negative z-direction had no z-component.

Drude behavior in the material Ag is implemented according to the permittivity in Eq. 4.1 with $\omega_p = 1.37 \times 10^{16}$ rad/s is the plasma frequency and $\gamma = 8.20 \times 10^{13}$ rad/s is the scattering frequency in the nanorods [64,65]. This plasma frequency is three orders of magnitude larger than the frequencies investigated in this work, which are < 4 THz. The peak of the incident spectrum is at ~ 1 THz, corresponding to a wavelength of 300 μm. Absorption features due to plasmon resonances in metallic nanostructures typically occur at wavelengths which differ from the spatial extent of the nanostructure by a factor of ~ 10 or less [71–73]. The 100 nm $\times$ 1 μm Ag nanorods do not constitute a combination of morphology and material parameters that may exhibit plasmon resonance effects in the few-terahertz regime. Indeed, this was born out by preliminary simulations in which the nanorod array depicted in Fig. 4.10 (b) transmitted essentially all of the incident radiation regardless of it's polarization, as will be described in the Section 4.3.3.

The actual nanorods are deposited on a silicon substrate with a thickness of 640 μm. Its inclusion in simulations would require an increase of the necessary computational space volume by a factor > 275. It is known that the presence of a dielectric material encompassing metallic nanostructures influences plasmon resonance and leads to a shift and change of shape of absorption features in the visible frequency range as its refractive index is varied [74, 75]. In this work however, the Ag nanorods and the silicon substrate constitute distinct layers excited by comparatively low-frequency fields. Absorption features associated with plasmon resonance are not augmented by the presence of the dielectric substrate because there are no absorption features to speak of. It is unlikely for the silicon, having band gap frequency > 200 THz and being transmissive in the incident frequency band, to have bearing on a dependence of the transmittance on incident polarization. Such a dependence was the motivation for this investigation, and simulation results are compared with experimental data that are normalized to measurements made using blank silicon substrates. The silicon substrate was ignored in this study on these grounds.

It is clear that the morphology constructed for simulations shown in Fig. 4.10 (b) is an idealization of general features of the array shown in the SEM image Fig. 4.10 (a). The actual samples show nanorods that are connected by various areas of contact and separated to various extents. It may be hypothesized that the nanorods are coupled by material connections that may be resistive or capacitive in nature. If the point of contact between nanorods is significantly smaller than the rod diameter, then the connection is resistive. If protuberances on nanorods are in very close proximity but not actually in contact, then the coupling is capacitive. These small features would demand a finer spatial grid in the context of FDTD calculations. The 8 nm grid cell size corresponds to a grid sampling density $N_\lambda = 10^4$ at frequency 3.75 THz, which is at the upper edge of the frequency range of interest. This grid sampling density is already three orders of magnitude larger than that which is considered necessary for numerical stability [4]. Seeing as the computational memory requirement scales as N^3 for a total number of grid cells N, and the computational run time for a given propagation distance scales as N^4, attempts to accurately resolve the fine material structure would be rather crude. Furthermore, the far-field, statistically significant terahertz transmission properties realized experimentally must be determined by the properties of some simplified morphology that captures those effects which survive a suitable spatial average. Supposing that the relevant transmission behavior can be captured by adding resistive and capacitive connections to the 2D unit cell of the base morphology shown in Fig. 4.10 (b), numerical transmission "experiments" were performed using the resulting nanostructure with periodic boundary conditions imposed along its transverse dimensions. In this way, a search of the parameter space of connective geometries was avoided by instead varying resistivities and dielectric constants of the added connective elements. The former is parameterized by the scattering frequency used in implementing the Drude model in a given element, while the latter is adjusted by the dielectric constant of the material placed between metallic surfaces. The dependence of the transmission on incident polarization measured by Zhang

et al. [76] motivated an exploration of the various arrangements and material parameters of the additional connective elements in FDTD simulations. Results of this investigation are presented in the next section.

4.3.3 Results and Discussion

Freestanding nanorods of the base morphology and impedance-matched connections

The transmittance of the base morphology is essentially unity regardless of the polarization of the incident pulse. This can be understood by viewing the array as a collection of scatterers in the long-wavelength regime. A collection of small scatterers infinite and periodic in the transverse directions has a scattering structure factor which vanishes in all but the forward direction [2]. The 1 μm rod length is not expected to exhibit absorption associated with plasmon resonance at the frequencies of interest. This was verified by calculations of the base morphology transmittance and reflectance at higher frequencies, which revealed a lowest-frequency absorptance peak of 0.15 at 163 THz for the case of y-polarized incidence. Recalling that the frequencies of interest are < 4 THz, it is clear that the base morphology does not exhibit the transmission behavior found in the experiments (see Figs. 4.13 and 4.14). If the nanorods in the unit cell are connected along the y-direction by an additional rod segment with equal diameter and material parameters, then an incident pulse polarized in that direction is essentially completely attenuated because the impedance is matched along the length of rods that are of infinite extent by virtue of the periodic boundary condition. On the other hand, an incident wave polarized orthogonal to the infinite rods (in a separate calculation) is essentially completely transmitted because the very low frequency current along the infinite rods is not excited. This structure behaves like a high-efficiency wire grid polarizer. These results are summarized in Table 4.2, where the magnitudes of the

Table 4.2: Summary of transmitted electric field magnitudes at 1 THz.

Incident Polarization	Base Morphology	Connected along y-direction
x-direction	0.99995	0.9993
y-direction	0.99898	0.00424

transmitted electric field amplitudes at 1 THz are listed for each case. At this point it is clear that the measured polarization dependence of the nanorod array's terahertz transmission must be attributed to less trivial inter-rod connections.

Freestanding nanorods coupled by resistive connections

The results summarized in Table 4.2 suggested a hypothesis of orthogonal resistive connections between nanorods in order to account for experimental results. Shown in Fig. 4.11, the blue connections use a Drude model with scattering frequency increased relative to that used by the nanorods of the base morphology by a factor of 16. The green rods supply connectivity in the x-direction and have their scattering frequency increased by a factor of 3.5. The transmitted amplitudes for various incident polarization angle ϕ are plotted in Fig. 4.13, along with the experimental results obtained by Zhang *et al.* [76].

Freestanding nanorods coupled by resistive and capacitive connections

Although it is not obvious from the data plotted in Fig. 4.13, the transmission spectra calculated by the FDTD method exhibit weak high/low-pass behavior depending on polarization angle ϕ. When normalized to the incident spectrum, the y-polarized transmittance is seen to decrease with frequency, while the x-polarized transmittance increases with frequency. This behavior can be augmented by the addition of a capacitive element that leads to high- or

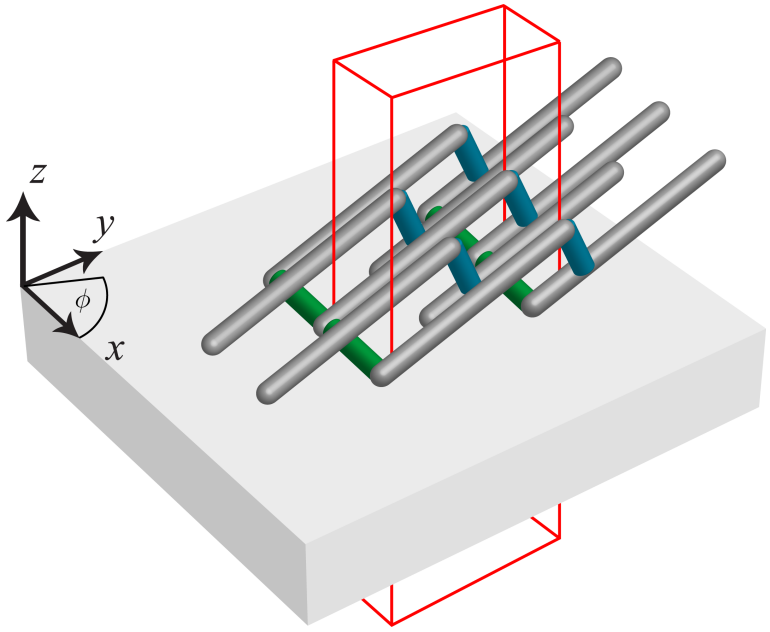

Figure 4.11: The base morphology of Fig. 4.10 with resistive connections added. The unit cell is a 250 nm × 893 nm cross-section of the computational domain, which is indicated by the red box. The blue Drude metal has its scattering frequency increased by a factor of 16. The green Drude metal has its scattering frequency increased by a factor of 3.5.

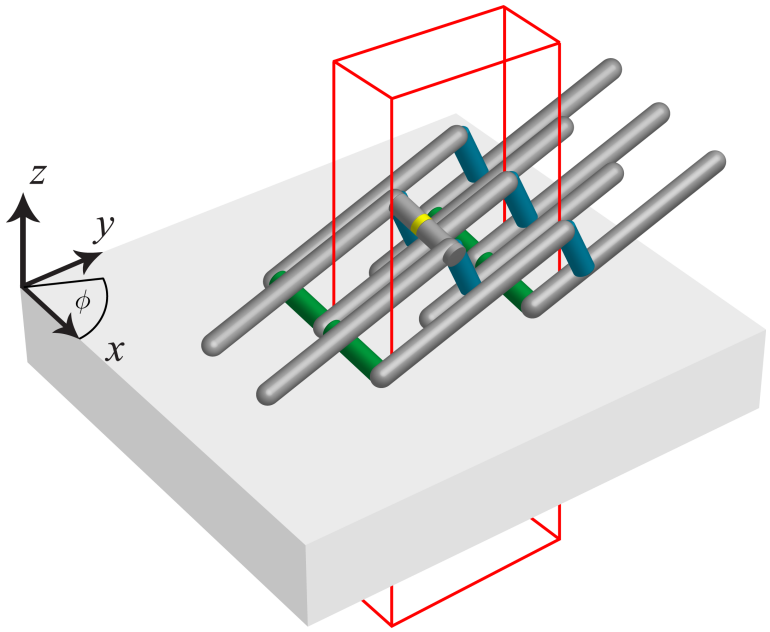

Figure 4.12: The connected morphology of Fig. 4.11 with a capacitive connection added to the unit cell. The relative permittivity of the dielectric layer (yellow) is 800.

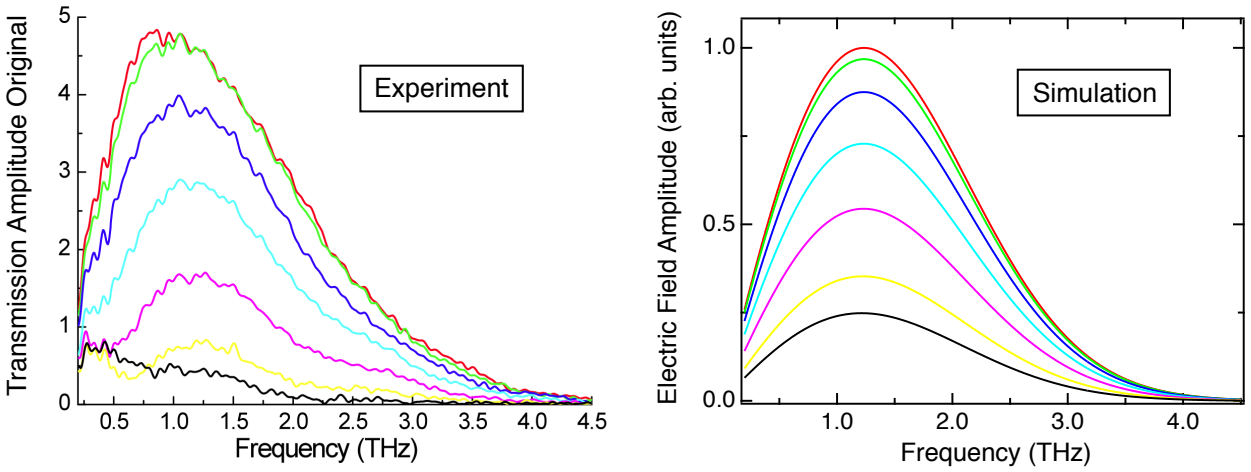

Figure 4.13: Measured and simulated transmitted electric field amplitude for various incident polarizations ϕ. These simulations used the morphology in Fig. 4.11. Note that vertical axis scales are arbitrary. Color – ϕ correspondence (top to bottom): Red – 0°, Green – 15°, Blue – 30°, Cyan – 45°, Magenta – 60°, Yellow – 75°, Black – 90°.

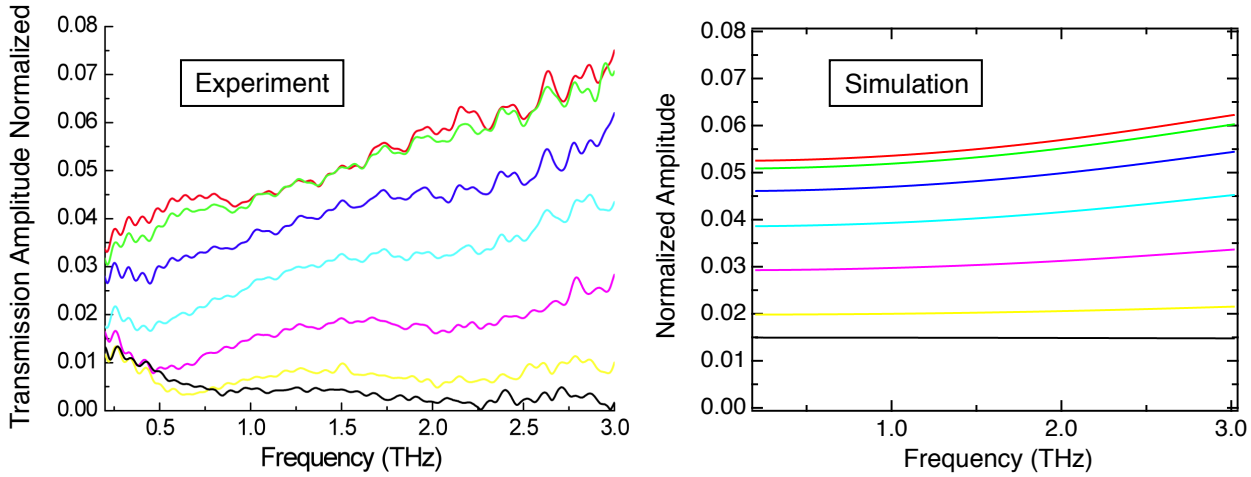

Figure 4.14: Measured and simulated normalized transmitted electric field amplitude for various incident polarizations ϕ. The experimental data are normalized to transmission data for a blank substrate. The FDTD data are normalized to the incident spectrum. These simulations used the morphology in Fig. 4.12. Color – ϕ correspondence (top to bottom): Red – 0°, Green – 15°, Blue – 30°, Cyan – 45°, Magenta – 60°, Yellow – 75°, Black – 90°.

low-pass behavior that depends on the polarization of the incident pulse and the arrangement and material parameters of the connective elements. This is analogous to a simple RC circuit that forms a voltage filter that preferentially transmits high or low frequencies depending on whether the output voltage is taken across the resistor or the capacitor. Shown in Fig. 4.14 alongside corresponding experimental results are normalized transmission spectra calculated for the case of the morphology shown in Fig. 4.12, where a capacitive element has been incorporated into the unit cell such that the array accentuates the high-pass behavior of the x-component of the terahertz field. The resistive elements use the same scattering frequencies as before. The capacitive element is constructed from the same metal as the rods of the base morphology, with equal diameter (100 nm), but incorporating a dielectric layer with relative permittivity 800 and thickness 20 nm. If the simplistic form of capacitance in terms of parallel plates of area A separated by a dielectric with thickness d is assumed, then the dielectric constant of the capacitive element can be reduced to correspond to that of air while keeping the capacitance constant if A/d is increased by a factor of 800. Taking A to be the surface area of one of the nanorods and $d = 1$ nm constitutes one set of geometrical parameters that results in the same capacitance with unit dielectric constant. Note that the experimental data are normalized to measured transmission data corresponding to a blank silicon substrate, whereas the FDTD calculation includes no substrate and is normalized to the incident spectrum.

The agreement between the simulation and experimental results shown in Fig. 4.14 is limited by the constraint to morphologies with translational symmetry of such short lattice vectors. In other words, the investigation of connections within the smallest unit cell of the staggered base morphology is computationally convenient, but limits the accessible spatial extent of impedance-matched electrical pathways. With this limitation, the spatial confinement of uniformly damped oscillations on the metallic surfaces is limited by the unit cell size. Longer-range impedance-matched electrical pathways are thought to be respon-

sible for the non-monoticity occurring in the normalized transmission spectra measured in the experiments at intermediate incident polarization angles as shown in Fig. 4.14. More computationally expensive calculations which used a unit cell area expanded by a factor of 8 were performed to explore this briefly, resulting in the identification of non-monoticity on this ~ 1 THz frequency scale. Given the sample-to-sample variation in current experimental results, and the significantly expanded parameter space search that would be necessary to capture the intermediate-ϕ non-monoticity, a detailed investigation of this effect was not conducted.

4.3.4 Conclusion

The results of this numerical study suggest that the spatially-averaged inter-rod coupling exhibited by ~ 1 μm nanorods in the ~ 300 μm wavelength regime may be described in terms of anisotropic R-C coupling between the nanorods. This anisotropy is attributable to the anisotropy of the Ag nanorods fabricated by Oblique Angle Deposition as manifested by SEM images. It is important to note that the arrangement of the added connections is not arbitrary. The choice depicted in Fig. 4.12 was the result of exhaustive efforts to replicate the experimental result with minimal deviation from the base morphology. The high-pass behavior shown in Fig. 4.14, in particular, relies completely on the chosen placement of the x-directed capacitive and resistive connective segments. It is possible that these results shed light on the nature of inter-rod coupling that generalizes to nanorod arrays fabricated with somewhat different deposition parameters (leading to, for example, a different nanorod tilt angle). This could offer guidance as to what sort of nanoscale materials should be selected for micro-patterning and subsequent use in THz optics.

Chapter 5

Summary, Conclusions, and Future Work

The investigations conducted as part of this dissertation have fostered a knowledge spanning several disciplines of optics. The ultrashort pulse measurements described in Chapter 2 have demonstrated that standard fabrication techniques can produce monolithic optical devices capable of stretching femtosecond pulses in a fairly predictable and controlled manner. The analysis led to the conclusion that the disparity between predicted and measured temporal intensity profiles for the stretched pulses is most likely due to the combination of small fabrication errors of the first-time production of only a few specimens and the deviation of the laboratory incident pulse from the ideal, flat-phase Gaussian pulse used in the device design. Furthermore, FDTD simulation results described in [7] strongly suggest that a very wide range of reflected pulse shapes are possible using the design scheme. Future work could include the design and optimization of paired devices to stretch and subsequently compress a measured pulse, whose deviation from an ideal Gaussian could be accounted for at the design stage.

Chapter 3 described the FDTD numerical investigation of two-beam coupling in liquid crystals under the influence of a photorefractive space-charge field. The main finding was that the standard treatment of flexoelectricity in the anisotropic liquid crystal layer does not account for the overall magnitude of the measured gain, but that it does predict oscillations present in the experimental data that are absent from the analytical beam propagation result. Future work includes implementation of the director profile corresponding to cholesterics for the purpose of conducting a follow-up investigation of beam coupling in these mesogens.

Finally, heuristic yet satisfying models for the coupling between Ag nanorods have been constructed in Chapter 4. The pores in Ag nanorods deposited at low temperatures were identified as electric field hot spots in FDTD calculations, which further demonstrated the significance of the blade-like rod tips to the electromagnetic contribution to SERS enhancement. An investigation of the transmission properties of similar nanorod arrays in the few-THz regime resulted in the conclusion that the spatially-averaged inter-rod coupling exhibited by the $\sim$ 1 μm nanorods may be described in terms of anisotropic R-C coupling between the nanorods. Future work includes retrieving effective medium parameters for the anisotropic nanorods at THz frequencies. The extraction of effective permittivities and permeabilities corresponding to orthogonal polarizations would enable the simulation of lithographically-patterned structures with arbitrarily-shaped apertures. This would facilitate the optimization of optical properties that depend on aperture shape, resulting in a useful computational design scheme.

Appendix A

SHG-FROG Retrieval Algorithm

Extraction of the pulse field $E(t)$ from the FROG trace is equivalent to a two-dimensional phase retrieval problem. The method of generalized projections entails projecting between two subsets of the set of all complex functions of two variables. These two subsets correspond to constraints applied during an iteration of the algorithm (see Fig. A.1):

- Eq. 2.5 provides the (data) constraint that the squared magnitude of the Fourier transform of $E_{\text{sig}}(t, \tau)$ must be in agreement with the FROG trace data. This is an empirical statement.

- Eq. 2.6 provides the (nonlinear optical) constraint that $E_{\text{sig}}(t, \tau)$ must be generated by the functional form $E(t)\,E(t-\tau)$ for the case of SHG-FROG. This is a theoretical statement.

The intersection of these two sets represents the solution which uniquely yields $E(t)$. In this work, a set of pseudorandom complex numbers was used as the initial guess for $E(t)$ needed to start the algorithm.

Figure A.1: Flowchart of the SHG-FROG retrieval algorithm with generalized projections (adapted from [10]).

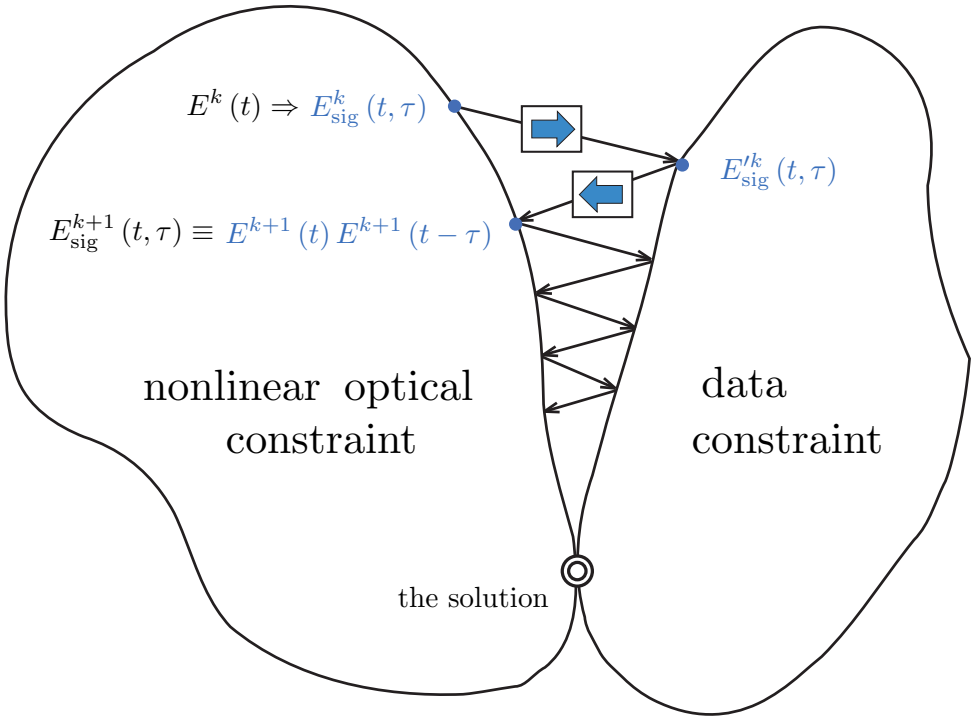

$$E^k_{\text{sig}}(t,\tau) \xrightarrow{\text{FT}} \tilde{E}^k_{\text{sig}}(\omega,\tau) \rightarrow \tilde{E}'^k_{\text{sig}}(\omega,\tau) = \frac{\tilde{E}^k_{\text{sig}}(\omega,\tau)}{\left|\tilde{E}^k_{\text{sig}}(\omega,\tau)\right|}\sqrt{I_{\text{FROG}}(\omega,\tau)} \xrightarrow{\text{FT}^{-1}} E'^k_{\text{sig}}(t,\tau)$$

Compute the field $E^{k+1}(t)$ that minimizes the functional distance between $E'^k_{\text{sig}}(t,\tau)$ and $E^{k+1}(t)\,E^{k+1}(t-\tau)$

Appendix B

High Dynamic Range FROG trace

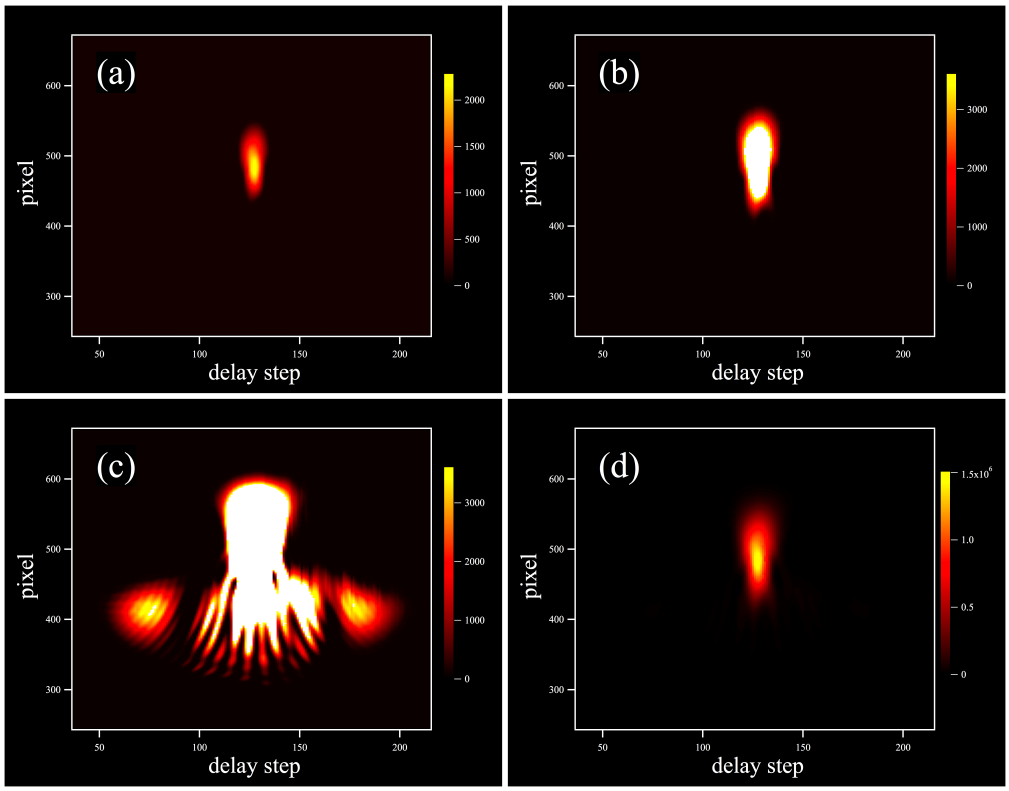

Figure B.1: Construction of a high dynamic range FROG trace measured for the incident pulse described in section 2.2. FROG traces acquired using (a) 3 ms, (b) 12 ms, and (c) 384 ms integration times, and (d) the resulting high dynamic range FROG trace. White pixels indicate values that saturate the color scales.

Appendix C

Liquid Crystal TL205 and Photorefractive SBN:Ce Material Parameters

Table C.1: Parameters used in the FDTD simulations described in Chapter 3 unless stated otherwise in the text. "Ph" refers to the SBN:Ce photorefractive windows.

Symbol	Value	Units	Description
L	10	μm	Thickness of the LC layer
N_{a}	3.8×10^{21}	m^{-3}	Density of acceptor impurities in Ph windows
N_{d}	1.328×10^{25}	m^{-3}	Density of donor impurities in Ph windows
$\varepsilon_{\mathrm{Ph}}$	200	(unitless)	Dielectric constant of Ph windows
n_{Ph}	2.4	(unitless)	Refractive index used in the Ph windows
T	293.15	K	Ambient temperature
e_{11}	10^{-11}	C/m	LC flexoelectric coefficient
e_{33}	10^{-11}	C/m	LC flexoelectric coefficient
K_{11}	1.73×10^{-11}	N	LC splay elastic constant at room T
K_{33}	2.04×10^{-11}	N	LC bend elastic constant at room T
$\varepsilon_{\parallel}$	2.3317	(unitless)	Rel. perm. $\parallel$ director at optical frequencies
$\varepsilon_{\perp}$	3.0433	(unitless)	Rel. perm. $\perp$ director at optical frequencies
$\tilde{\varepsilon}_{\parallel}$	9.1	(unitless)	Static rel. perm. $\parallel$ director
$\tilde{\varepsilon}_{\perp}$	4.1	(unitless)	Static rel. perm. $\perp$ director

Appendix D

Expansion of $\vartheta(y, z)$ from Eq. 3.19 in Terms of Real Quantities

In this expansion, the complex modulation parameters in the front and back photorefractive windows are written as

$$\mathcal{M}_{\mathrm{F}} = m_{\mathrm{F}}\, e^{i\phi_{\mathrm{F}}} \qquad \text{and} \qquad \mathcal{M}_{\mathrm{B}} = m_{\mathrm{B}}\, e^{i\phi_{\mathrm{B}}} \tag{D.1}$$

See Section 3.3 for a discussion of their meaning.

(continued next page)

The director profile is

$$\begin{aligned}
\vartheta(y,z) = \theta_0(z) + \frac{(-1)\; r\, E_{\rm d}}{q\left(\tilde{q}^2 - q_1^2\right)^2 \left(1 + \frac{E_{\rm d}}{E_q}\right)} \times \\
\Big\{\; m_{\rm F} \Big[Q_q \sin(qy + \phi_{\rm F}) \left(e^{-\tilde{q}(z+L/2)} - e^{-q_1(z+L/2)} \right) + \\
+ \cos(qy + \phi_{\rm F}) \left(H_0^+(z)\, e^{-\tilde{q}(z+L/2)} - H_{\rm F}\, e^{-q_1(z+L/2)} \right) \Big] + \\
+ m_{\rm B} \Big[Q_q \sin(qy + \phi_{\rm B}) \left(e^{\,q_1(z-L/2)} - e^{\,\tilde{q}(z-L/2)} \right) + \\
+ \cos(qy + \phi_{\rm B}) \left(H_0^-(z)\, e^{\,\tilde{q}(z-L/2)} - H_{\rm B}\, e^{\,q_1(z-L/2)} \right) \Big] \;\Big\}
\end{aligned} \tag{D.2}$$

where

$$H_0^+(z) = \left(\tilde{q}^2 + q^2\right)\left(\tilde{q}^2 - q_1^2\right)\theta_0(z) + 2p\tilde{q}\left(\tilde{q}^2 + q^2\right), \tag{D.3}$$

$$H_0^-(z) = \left(\tilde{q}^2 + q^2\right)\left(\tilde{q}^2 - q_1^2\right)\theta_0(z) - 2p\tilde{q}\left(\tilde{q}^2 + q^2\right), \tag{D.4}$$

$$H_F = \left(\tilde{q}^2 + q^2\right)\left(\tilde{q}^2 - q_1^2\right)\theta_{\rm F} + 2p\tilde{q}\left(\tilde{q}^2 + q^2\right), \tag{D.5}$$

$$H_B = \left(\tilde{q}^2 + q^2\right)\left(\tilde{q}^2 - q_1^2\right)\theta_{\rm B} - 2p\tilde{q}\left(\tilde{q}^2 + q^2\right), \tag{D.6}$$

$$Q_q = q\,\tilde{q}\left(\tilde{q}^2 - q_1^2\right), \tag{D.7}$$

and the quantities q, $E_{\rm d}$, E_q, $\theta_{\rm F}$, $\theta_{\rm B}$, p, $\theta_0(z)$, r, $\tilde{q}$, q_1, are defined in Sections 3.3 and 3.4.

Bibliography

[1] T. H. Maiman, "Stimulated optical radiation in ruby," *Nature* **187**, 493 (1960).

[2] J. D. Jackson, *Classical Electrodynamics*, John Wiley & Sons, New York, 3rd ed. (1998).

[3] M. V. Agranovich and Y. N. Gartstein, "Spatial dispersion and negative refraction of light," *Physics-Uspekhi* **49**(10), 1029 (2006).

[4] A. Taflove and S. C. Hagness, *Computational Electrodynamics: The Finite-Difference Time-Domain Method*, Artech House, Norwood, MA, 3rd ed. (2005).

[5] J.-P. Béringer, *Perfectly Matched Layer (PML) for Computational Electromagnetics*, Synthesis Lectures on Computational Electromagnetics, Morgan & Claypool, Seattle (2007).

[6] M. Born and E. Wolf, *Principles of Optics: Electromagnetic Theory of Propagation, Interference, and Diffraction of Light*, Cambridge University Press, Cambridge, 6th ed. (1997).

[7] S. Dunning, *Optimizing Thin Film Filters for Ultrashort Pulse Shaping*. Phd, University of Georgia (2009).

[8] K. F. Wall and A. Sanchez, "Titanium sapphire lasers," *The Lincoln Laboratory Journal* **3**(3) (1990).

[9] R. Trebino and D. J. Kane, "Using phase retrieval to measure the intensity and phase of ultrashort pulses: frequency-resolved optical gating," *J. Opt. Soc. Am. A* **10**(5), 1101 (1993).

[10] R. Trebino, *Frequency-Resolved Optical Gating: The Measurement of Ultrashort Optical Pulses*, Kluwer Academic Publishers, Boston (2000).

[11] M. D. Levenson and S. S. Kano, *Introduction to Nonlinear Laser Spectroscopy - Revised Edition*, Quantum Electronics - Principles and Applications, Academic Press, San Diego (1988).

[12] http://www.newlightphotonics.com/bbo-properties.html

[13] C. J. Sansonetti, M. L. Salit, and J. Reader, "Wavelengths of spectral lines in mercury pencil lamps," *Appl. Opt.* **35**(1), 74 (1996).

[14] S. W. Winkler, *Nondestructive Interaction of Ultrafast Laser Pulses with Transparent Dielectrics*. Phd, University of Georgia (2009).

[15] K. W. DeLong, R. Trebino, J. Hunter, and W. E. White, "Frequency-resolved optical gating with the use of second-harmonic generation," *J. Opt. Soc. Am. B* **11**(11), 2206 (1994).

[16] A. Ashkin, G. D. Boyd, J. M. Dziedzic, R. G. Smith, A. A. Ballman, J. J. Levinstein, and K. Nassau, "Optically-induced refractive index inhomogeneities in $LiNbO_3$ and $LiTaO_3$," *Applied Physics Letters* **9**(1), 72 (1966).

[17] *Photorefractive Materials and Their Applications*, (3 volume series), P. Günter and J.-P. Huignard, Eds., Springer, New York (2006).

[18] R. W. Boyd, *Nonlinear Optics*, Academic Press, San Diego, 2nd ed. (2003).

[19] L. Hesselink, S. S. Orlov, A. Liu, A. Akella, D. Lande, and R. R. Neurgaonkar, "Photorefractive materials for nonvolatile holographic data storage," *Science* **282**, 1089 (1998).

[20] H. Ono, A. Emoto, and N. Kawatsuki, "Photorefractive mesogenic composites for applications to image processing," in *Photorefractive Materials and Their Applications 3*, P. Günter and J.-P. Huignard, Eds., **3**, Springer, New York (2006).

[21] T. Omatsu and M. J. Damzen, "Multi-watt cw output from a double-pass diode side-pumped Nd:YVO_4 amplifier with a Rh:$BaTiO_3$ phase conjugator," *Optics Communications* **198**, 135 (2001).

[22] G. Pauliat, N. Dubreuil, and G. Roosen, "Self-organizing laser cavities," in *Photorefractive Materials and Their Applications 3*, P. Günter and J.-P. Huignard, Eds., **3**, Springer, New York (2006).

[23] A. Godard, G. Pauliat, G. Roosen, and É. Ducloux, "Relaxation of the single-mode emission conditions in extended-cavity semiconductor lasers with a self-organizing photorefractive filter," *Appl. Opt.* **43**(17), 3543 (2004).

[24] N. Dubreuil, G. Pauliat, and G. Roosen, Paper We4.P.065, in *Proceedings of the 30th European Conference on Optical Communications*, **3**, 600–601 (2004).

[25] S. Chandrasekhar, *Liquid Crystals*, Cambridge University Press, Cambridge, 2nd ed. (1992).

[26] F. Reinitzer, "Beiträge zur kenntniss des cholesterins," *Monatshefte für Chemie* **9**(1), 421 (1888).

[27] O. Lehmann *Z. Physikal. Chem.* **4**, 462 (1889).

[28] E. V. Rudenko and A. V. Sukhov, "Photoinduced electrical conductivity and photorefraction in a nematic liquid crystal," *JETP Letters* **59**(2) (1994).

[29] E. V. Rudenko and A. V. Sukhov, "Optically induced spatial charge separation in a nematic and the resultant orientational nonlinearity," *Sov. Phys. JETP* **78**(6) (1994).

[30] E. V. Rudenko and A. V. Sukhov, "Photorefractive effect in nematic liquid crystals: Ion-diffusion approach," *Molecular Crystals and Liquid Crystals Science and Technology* **282**(1) (1996).

[31] I.-C. Khoo, "Liquid crystal photorefractive optics: Dynamic and storage holographic grating formation, wave mixing, and beam/image processing," in *Photorefractive Optics: Materials, Properties, and Applications*, F. T. S. Yu and S. Yin, Eds., Academic Press, San Diego (2000).

[32] G. S. He and S. H. Liu, *Physics of Nonlinear Optics*, World Scientific, New Jersey (1999).

[33] P. Yeh, *Introduction to Photorefractive Optics*, Wiley Series in Pure and Applied Optics, Wiley, New York (1993).

[34] A. Yariv, *Introduction to Optical Electronics*, Holt, Rinehart, and Winston, New York, 2nd ed. (1976).

[35] V. Y. Reshetnyak, I. P. Pinkevych, G. Cook, D. R. Evans, and T. J. Sluckin, "Two-beam energy exchange in a hybrid photorefractive-flexoelectric liquid-crystal cell," *Physical Review E* **81**(3), 031705 (2010).

[36] J. Frejlich, *Photorefractive Materials : Fundamental Concepts, Holographic Recording and Materials Characterization*, John Wiley & Sons, Hoboken, New Jersey (2007).

[37] I. Biaggio, "Recording speed and determination of basic material properties," in *Photorefractive Materials and Their Applications 2*, P. Günter and J.-P. Huignard, Eds., **2**, Springer, New York (2006).

[38] A. M. Glass, M. B. Klein, and G. C. Valley, "Fundamental limit of the speed of photorefractive effect and its impact on device applications and material research: comment," *Appl. Opt.* **26**(16), 3189 (1987).

[39] I.-C. Khoo, *Liquid Crystals: Physical Properties and Nonlinear Optical Phenomena*, John Wiley & Sons, New York (1995).

[40] W. H. Press, S. A. Teukolsky, W. T. Vetterling, and B. P. Flannery, *Numerical Recipes in Fortran 77*, vol. 1, Cambridge University Press, 2nd ed. (1986).

[41] N. F. Mott and H. S. W. Massey, *The Theory of Atomic Collisions*, Clarendon Press, Oxford, 3rd ed. (1965).

[42] W. K. H. Panofsky and M. Phillips, *Classical Electricity and Magnetism*, Addison-Wesley, Reading, Massachusetts, 2nd ed. (1962).

[43] S. González García, B. García Olmedo, and R. Gómez Martín, "A time-domain near-to far-field transformation for FDTD in two dimensions," *Microwave and Optical Technology Letters* **27**(6), 427 (2000).

[44] X. Li, Z. Chen, A. Taflove, and V. Backman, "Modified FDTD near-to-far-field transformation for improved backscattering calculation of strongly forward-scattering objects," *IEEE Antennas and Wireless Propagation Letters* **4**, 35 (2005).

[45] G. R. Fowles, *Introduction to Modern Optics*, Dover, Mineola, New York, 2nd ed. (1989).

[46] D. R. Evans and G. Cook, "Bragg-matched photorefractive two-beam coupling in organic-inorganic hybrids," *Journal of Nonlinear Optical Physics & Materials* **16**(3), 271 (2007).

[47] *Structured Surfaces as Optical Metamaterials*, A. A. Maradudin, Ed., Cambridge University, Cambridge (2011).

[48] Y. J. Liu, H. Y. Chu, and Y.-P. Zhao, "Silver nanorod array substrates fabricated by oblique angle deposition: Morphological, optical, and SERS characterizations," *The Journal of Physical Chemistry C* **114**(18), 8176 (2010).

[49] S. B. Chaney, S. Shanmukh, R. A. Dluhy, and Y.-P. Zhao, "Aligned silver nanorod arrays produce high sensitivity surface-enhanced raman spectroscopy substrates," *Applied Physics Letters* **87**(3), 031908 (2005).

[50] M. Chelvayohan and C. H. B. Mee, "Work function measurements on (110), (100), and (111) surfaces of silver," *J. Phys. C: Solid State Phys.* **15**, 2305 (1982).

[51] Y.-P. He and Y.-P. Zhao, "Advanced multi-component nanostructures designed by dynamic shadowing growth," *Nanoscale* **3**(6), 2361 (2011).

[52] R. D. Guenther, *Modern Optics*, John Wiley & Sons, New York (1990).

[53] J. M. Stone, *Radiation and Optics*, McGraw-Hill, New York (1963).

[54] K. Kneipp, Y. Wang, H. Kneipp, L. T. Perelman, I. Itzkan, R. R. Dasari, and M. S. Feld, "Single molecule detection using surface-enhanced raman scattering (SERS)," *Physical Review Letters* **78**(9), 1667 (1997).

[55] Y.-J. Liu, Z.-Y. Zhang, Q. Zhao, R. A. Dluhy, and Y.-P. Zhao, "Surface enhanced Raman scattering from an Ag nanorod array substrate: The site dependent enhancement and layer absorbance effect," *The Journal of Physical Chemistry C* **113**(22), 9664 (2009).

[56] E. V. Albano, S. Daiser, G. Ertl, R. Miranda, K. Wandelt, and N. Garcia, "Nature of surface-enhanced-raman-scattering active sites on coldly condensed Ag films," *Physical Review Letters* **51**(25), 2314 (1983).

[57] J. Singh, T. E. Lanier, H. Zhu, W. M. Dennis, R. A. Tripp, and Y.-P. Zhao, "Highly sensitive and transparent surface enhanced Raman scattering substrates made by active coldly condensed Ag nanorod arrays." Manuscript submitted for publication (2012).

[58] E. C. Le Ru, M. Meyer, E. Blackie, and P. G. Etchegoin, "Advanced aspects of electromagnetic SERS enhancement factors at a hot spot," *Journal of Raman Spectroscopy* **39**(9), 1127 (2008).

[59] F. J. García-Vidal and J. B. Pendry, "Collective theory for surface enhanced raman scattering," *Physical Review Letters* **77**(6), 1163 (1996).

[60] T. Vo-Dinh, "Surface-enhanced Raman spectroscopy using metallic nanostructures," *Trends in Analytical Chemistry* **17**(89), 557 (1998).

[61] L. Novotny and B. Hecht, *Principles of Nano-Optics*, Cambridge University Press, New York (2006).

[62] M. Kerker, D.-S. Wang, and H. Chew, "Surface enhanced Raman scattering (SERS) by molecules adsorbed at spherical particles: errata," *Appl. Opt.* **19**(24), 4159 (1980).

[63] M. Young, *Optics and Lasers*, vol. 5 of *Springer Series in Optical Sciences*, Springer-Verlag, New York, 3rd ed. (1986).

[64] M. A. Ordal, L. L. Long, R. J. Bell, S. E. Bell, R. R. Bell, R. W. Alexander, Jr, and C. A. Ward, "Optical properties of the metals Al, Co, Cu, Au, Fe, Pb, Ni, Pd, Pt, Ag, Ti, and W in the infrared and far infrared," *Appl. Opt.* **22**(7), 1099 (1983).

[65] J. Valentine, S. Zhang, T. Zentgraf, E. Ulin-Avila, D. A. Genov, G. Bartal, and X. Zhang, "Three-dimensional optical metamaterial with a negative refractive index," *Nature* **455**(7211), 376 (2008).

[66] Y.-J. Liu, Z.-Y. Zhang, Q. Zhao, and Y.-P. Zhao, "Revisiting the separation dependent surface enhanced Raman scattering," *Applied Physics Letters* **93**(17), 173106 (2008).

[67] M. Moskovits, "Surface-enhanced spectroscopy," *Reviews of Modern Physics* **57**(3), 783 (1985).

[68] M. Tonouchi, "Cutting-edge terahertz technology," *Nature Photonics* **1**(2), 97 (2007).

[69] O. Paul, R. Beigang, and M. Rahm, "Highly selective terahertz bandpass filters based on trapped mode excitation," *Opt. Express* **17**(21), 18590 (2009).

[70] P. Weis, O. Paul, C. Imhof, R. Beigang, and M. Rahm, "Strongly birefringent metamaterials as negative index terahertz wave plates," *Applied Physics Letters* **95**(17), 171104 (2009).

[71] C. Oubre and P. Nordlander, "Optical properties of metallodielectric nanostructures calculated using the finite difference time domain method," *The Journal of Physical Chemistry B* **108**(46), 17740 (2004).

[72] A. L. Atkinson, J. M. McMahon, and G. C. Schatz, "FDTD studies of metallic nanoparticle systems," in *Self-Organization of Molecular Systems – From Molecules and Clusters to Nanotubes and Proteins*, N. Russo, V. Y. Antonchenko, and E. Kryachko, Eds., Springer, The Netherlands (2009).

[73] E. Tatartschuk, E. Shamonina, and L. Solymar, "Plasmonic excitations in metallic nanoparticles: Resonances, dispersion characteristics and near-field patterns," *Opt. Express* **17**(10), 8447 (2009).

[74] T. R. Jensen, M. L. Duval, K. L. Kelly, A. A. Lazarides, G. C. Schatz, and R. P. V. Duyne, "Nanosphere lithography: effect of the external dielectric medium on the surface

plasmon resonance spectrum of a periodic array of silver nanoparticles," *The Journal of Physical Chemistry B* **103**(45), 9846 (1999).

[75] S. Malynych and G. Chumanov, "Coupled planar silver nanoparticle arrays as refractive index sensors," *Journal of Optics A: Pure and Applied Optics* **8** (2006).

[76] W. Cao and W. Zhang. Oklahoma State University, Stillwater, Oklahoma 74078 – Private Communication.